

**BASIC MODULE FOR AN INTEGRATED OPTICAL
PHASE DIFFERENCE MEASUREMENT AND
CORRECTION SYSTEM**

by

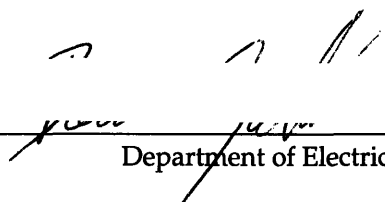
Boris Golubovic

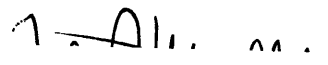
S.B. E.E., Massachusetts Institute of Technology (1991)

S.B. Physics, Massachusetts Institute of Technology (1990)

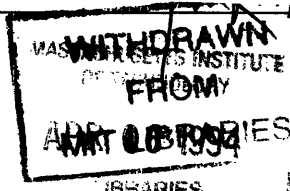
Submitted to the Department of
Electrical Engineering and Computer Science
in Partial Fulfillment of the Requirement for the
Degree of
Master of Science
in
Electrical Engineering and Computer Science
at the
Massachusetts Institute of Technology
September 1993

© Massachusetts Institute of Technology 1993
All Rights Reserved

Signature of Author  _____
Department of Electrical Engineering and Computer Science
September 30, 1993

Certified by  _____
Robert H. Rediker
Thesis Advisor

Accepted by _____
Frederic R. Morgenthaler
Chairman, Department Committee on Graduate Studies



BASIC MODULE FOR AN INTEGRATED OPTICAL PHASE DIFFERENCE MEASUREMENT AND CORRECTION SYSTEM

by

Boris Golubovic

Submitted to the Department of Electrical Engineering and Computer Science on
September 30, 1993 in partial fulfillment of the requirements for the degree of
Master of Science in Electrical Engineering and Computer Science

Abstract

A basic module for an integrated optical phase difference measurement and correction system was developed and fabricated in the GaAs-AlGaAs material system. The implemented device made it possible to measure the relative phase difference between two waveguides using a small fraction of the power (<10%) for diagnostic purposes. This proof-of-concept device incorporated waveguides, waveguide couplers and Y-junctions, phase modulators, and photodetectors on the same substrate. This thesis describes the design, fabrication and operation of the implemented device. Waveguide phase modulators with $V_{\pi}=5.0V$ for $\lambda=0.865\mu m$ were fabricated. Selective Be ion implantation and rapid thermal annealing was used to form the $p^+-n^- - n^+$ modulator structure. The phase was modulated via the linear electrooptic effect in the reverse-biased $p^+-n^- - n^+$ structure. A Y-junction interferometer was used to obtain the relative phase difference between the two waveguides. Integrated MSM photodetectors, $17\times 69\mu m$ in size, with TIR mirror coupling were used for signal detection. Both, the interferometer and detector were fabricated and operated between two, $30\mu m$ separated waveguides. A phase dither detection system made it possible to determine the relative phase between two waveguides largely independent of the power ratio between the individual guides.

Thesis Advisor: Dr. Robert H. Rediker
Title: Senior Research Scientist

Acknowledgments

I would like to thank my thesis advisor, Dr. Robert Rediker, for giving me the opportunity to do this research, and all the advice which went well beyond the scope of this thesis. I am grateful to Joe Donnelly for all his time, guidance, and encouragement during this thesis work. I have learned a great deal from him.

The AlGaAs material grown by Chris Wang, and Bill Goodhue's etching system were instrumental in the successful completion of this thesis. I would like to thank everyone in the Electrooptic Devices Group at Lincoln Laboratory, especially Bob Bailey and John Woodhouse, for their time and help in fabricating the devices for this thesis.

I am also thankful to my family and friends for their encouragement and support throughout the years.

Contents

1	Introduction	9
1.1	Background.....	9
1.2	Basic Module for an Integrated Optical Phase Difference Measurement and Correction System.....	10
1.2.1	Dither Phase Difference Measurement Technique	11
1.2.2	System Requirements for Combining GaAs-AlGaAs Integrated Optics and Electronic Circuitry.....	13
1.3	Thesis Outline.....	14
2	Modeling and Design of Integrated Semiconductor Optical Components	17
2.1	Modeling of Dielectric Optical Waveguides	17
2.1.1	Dielectric-loaded Strip Waveguides	17
2.1.2	The Effective Index Method.....	18
2.1.3	Optical Loss in Dielectric Waveguides.....	24
2.1.4	Index of Refraction in GaAs- $\text{Al}_x\text{Ga}_{1-x}\text{As}$	26
2.1.5	Waveguide Design and Modal Characteristics.....	26
2.2	Modeling of Dielectric Waveguide Couplers.....	29
2.2.1	Coupled-Mode Theory Coupler Analysis	30
2.2.2	Evaluating the Coupling Coefficient κ	33
2.2.3	Waveguide Coupler Design.....	34
2.3	Phase Modulators	37
2.3.1	Linear Electrooptic Effect in Zinc Blende 43m Crystals	40
2.3.2	Phase Modulator Refractive Index Profile.....	42
2.3.3	Phase Modulator Design.....	44
2.4	Integrated Photodetectors	46
2.4.1	Rectifying Metal-Semiconductor Junctions.....	47
2.4.2	MSM Photodetector with TIR Coupling.....	49
2.4.3	Detector Design	51
3	Fabrication of the Integrated Optical Phase Difference Measurement and Correction System	53
3.1	Device Fabrication	53
3.1.1	Photodetector Definition	54
3.1.2	Phase Modulator Definition (Be^+ Implantation).....	55
3.1.3	Waveguide Patterning and Etching.....	56
3.1.4	TIR Mirror Etch.....	58

3.1.5	Detector and Phase Modulator Contact Deposition	59
3.1.6	Contact Pad Deposition.....	59
3.1.7	Backside Processing	59
3.2	Photolithographic Mask Set	60
3.3	Fabricated Optical Phase Measurement and Correction Device	62
4	Integrated Optics and Opto-Electronics Evaluation and Measurement System	65
4.1	Optical Components.....	65
4.2	Experimental Set-up for Evaluating Phase Measurement and Correction Devices.....	68
5	Device Characterization Measurements	71
5.1	Waveguide Phase Difference Measurement	71
5.2	Integrated Photodetector Operation	74
5.3	Waveguide Phase Difference Measurement with an Integrated Photodetector	80
6	Conclusion	85
6.1	Summary	85
6.2	Future Work.....	86
A	Five-Layer Slab Waveguide	87
B	Normal Modes of Two-Guide Couplers	91
C	Device Processing Recipes	93
	References	101

1 Introduction

1.1 Background

Integrated guided-wave optical devices have many advantages for the analog processing of optical wavefronts. The benefits include small size, no moving parts, high-speed, reliability, and reproducibility in fabrication. An integrated optical phase front correcting device could be used in numerous applications which include: removing optical phase distortions for imaging applications, phasing the output of laser arrays, or setting the phase between a number of optical waveguides.

In general, a phase front correcting device consists of a set-up which measures the phase variations in the wavefront (at the device input), and a phase corrector for removing of these phase variations. Wavefront phase correctors were implemented using both transmissive devices, employing acoustooptical or electrooptical effects, and reflective devices, such as segment mirrors, monolithic piezoelectric mirrors, continuous thin-plate mirrors, and membrane mirrors. At the present time, reflective devices are the most successfully implemented wavefront correcting devices. In such devices, the phase is corrected by using a variety of substrate material and methods for deforming the mirror surface and thus changing the optical path length over the input wavefront. The design of the active mirror and the drive circuitry depend on the spatial and temporal requirements of the specific application. Active mirrors can be made of discrete segments with individual piston and tilt controls; or they may have a continuously deformable surface attached to an array of piston-action actuators (typically made from a piezoelectric material) which control the mirror deformations. Active control mirrors were successfully implemented for correcting effects of atmospheric turbulence in astronomical optical systems [1].

The design of a wavefront correcting devices used in real-time phase correction systems must consider the requirements set by the specific application such as: required spatial resolution, acceptable phase errors, the intensity variations over the input wavefront, and the response time of the phase correcting system. At this time most wavefront phase measurement systems use one of two approaches for determining the point to point phase difference of a measured wavefront. For the case of coherent sources the phase at each point can be

compared to a phase reference signal and corrected accordingly. In general, if it is assumed that the radiation is locally coherent, the slope of the phase at each point can be determined, and subsequently used to reconstruct the wavefront itself. Frequently used methods for phase measurement include phase-shifting interferometry [2]-[6], the use of a Hartmann sensor [7]-[10], and lateral shearing interferometry [11].

Rediker et al. [12]-[13] have demonstrated an integrated optical guided-wave system for wavefront sensing. An array of guided-wave elements for wavefront sensing was implemented in lithium niobate, LiNbO₃. In this wavefront sensor, spatial variations in intensity and phase were recorded by an array of alternate straight waveguides and Y-junction interferometers. The detectors at the ends of the straight waveguides measured the intensity, whereas detectors at the Y-junctions were used to record the phase. The optical output power P_{ϕ_n} of the n th interferometer was given by

$$P_{\phi_n} = \frac{1}{2} [P_n + P_{n+1} + 2\sqrt{P_n P_{n+1}} \cos\phi_n] B_n \quad (1.1)$$

where P_n and P_{n+1} are the powers at the outputs of the two adjacent waveguides, ϕ_n is the phase difference between the two interferometer arms at the Y-junction, and B_n takes into account losses due to bends and branches.

The small-size and high-speed potential make integrated guided-wave devices particularly attractive for the implementation of phase front correcting devices. The GaAs-AlGaAs material technology is well developed for use in fabricating integrated optical devices operating at wavelengths around 0.85 μ m (and above). Thus, when combined with integrated electronic control circuits an all integrated wavefront correcting device can be implemented.

1.2 Basic Module for an Integrated Optical Phase Difference Measurement and Correction System

The basic module for use at GaAs wavelengths that incorporates phase measurement and correction in the same integrated optical device is shown as a part of a larger system in Figure 1-1. The input and output can be coupled to other devices via waveguides, or to free-space by the means of integrated optical antennas [14]-[15]. A small fraction of the power from the straight-trough waveguide is (evanescently) coupled into an interferometer to measure the phase relation between the waveguides. The signal from the integrated photodetector is

used to determine the actual phase difference and calculate appropriate phase correcting voltages. The feedback electronics makes it possible to control the integrated phase modulators on the straight-trough waveguides, thus correct any phase distortions in the input wavefront.

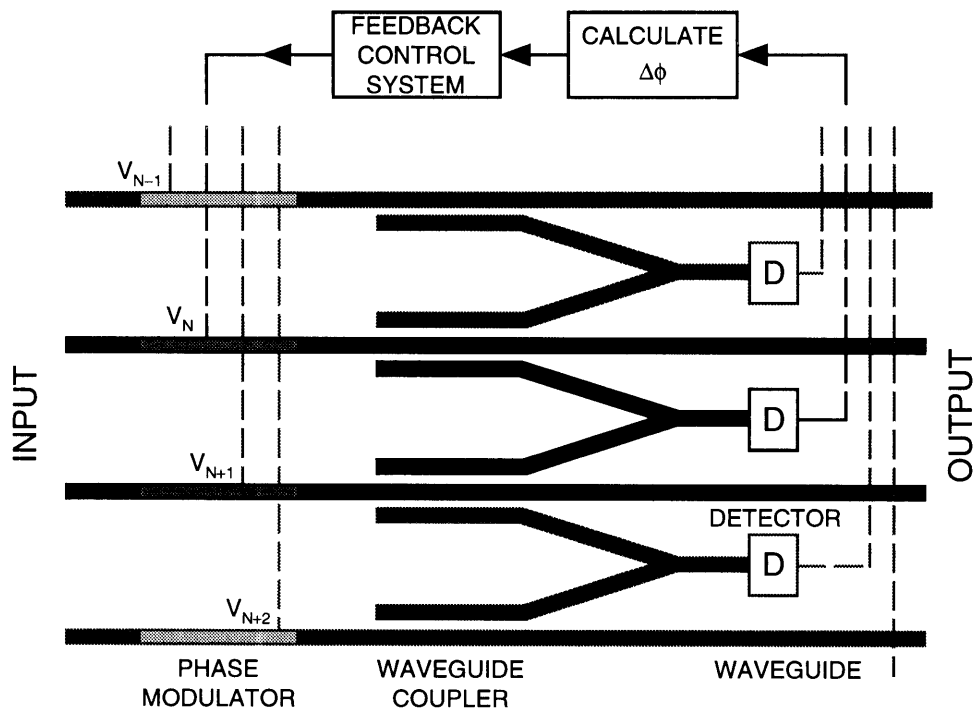


Figure 1-1: Section of an integrated wavefront correcting device. The highlighted part defines the basic module for phase difference measurement and correction. An actual phase front correcting device would consist of a large number of basic modules (>100).

This thesis had for the goal the proof-of-concept that a basic module that can be implemented as a single integrated optical device. The project required the modeling, design, and fabrication of low-loss AlGaAs guided-wave components including waveguides, bends, Y-junctions, couplers, modulators, and detectors. The device was designed for use with a dither interferometer technique such that phase measurements could be performed independent of the power and power ratio in the two interferometer arms [17].

1.2.1 Dither Phase Difference Measurement Technique

The interferometer technique used for determining the optical phase is similar to dither techniques used in optical fiber sensors [18]-[19], and phase-locked interferometry [20]-[21]. For this purpose an additional phase modulator

was incorporated into one of the Y-junction interferometer arms. If a sinusoidal phase change is applied to one interferometer arm (see Figure 1-2), the power at the detector is given by

$$P_{out} = |E_1|^2 + |E_2|^2 + 2E_1E_2 \cos(\Delta\phi - \Gamma \sin \omega t) \quad (1.2)$$

where E_1 and E_2 are the fields in the interferometer arms and the $\Delta\phi$ is the phase difference between the two arms. The cosine term in Equation (1.2) can be rewritten

$$\cos(\Delta\phi - \Gamma \sin \omega t) = \cos\Delta\phi \cos(\Gamma \sin \omega t) + \sin\Delta\phi \sin(\Gamma \sin \omega t) \quad (1.3)$$

and the time dependent terms can be expanded using Bessel functions

$$\cos(\Gamma \sin \omega t) = J_0(\Gamma) + 2 \sum_{k=1}^{\infty} J_{2k}(\Gamma) \cos[2k\omega t] \quad (1.4)$$

$$\sin(\Gamma \sin \omega t) = 2 \sum_{k=0}^{\infty} J_{2k+1}(\Gamma) \sin[(2k+1)\omega t] \quad (1.5)$$

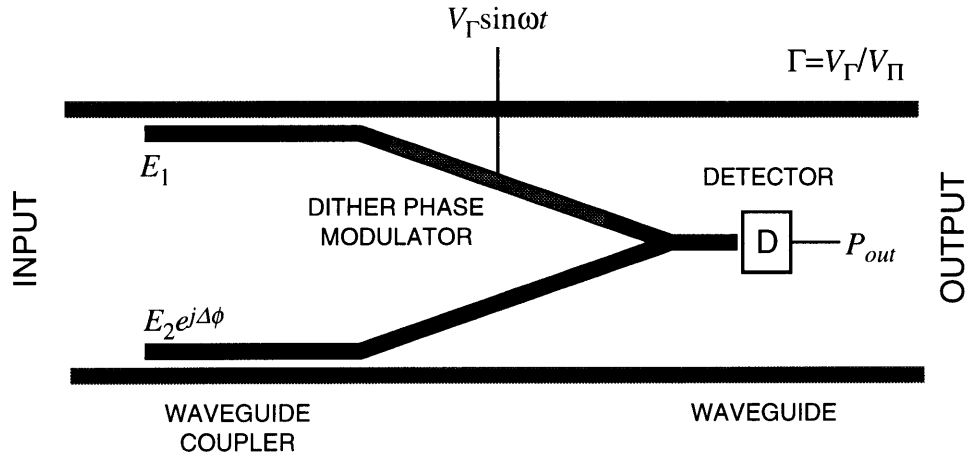


Figure 1-2: Interferometer with a dither modulator makes phase difference measurements independent of the power and power ratio in the interferometer arms possible.

Thus, if the signal in Equation (1.2) is passed through a pair of lock-in amplifiers set for the frequencies ω and 2ω (band-pass filters at ω and 2ω), the output amplitudes are described as follows:

$$A(\omega) = 2E_1E_2J_1(\Gamma) \sin\Delta\phi \quad (1.6)$$

$$A(2\omega) = 2E_1E_2J_2(\Gamma) \cos\Delta\phi \quad (1.7)$$

where $J_1(\Gamma)$ and $J_2(\Gamma)$ are Bessel functions of the first kind of order 1 and 2 respectively. Then the expression for the phase difference obtained from Equations (1.6) and (1.7) becomes

$$\Delta\phi = \arctan\left[\frac{A(\omega) J_2(\Gamma)}{A(2\omega) J_1(\Gamma)}\right] = \arctan\left[\frac{A(\omega) \left(\frac{\Gamma^2}{8} - \frac{\Gamma^4}{96} + \dots\right)}{A(2\omega) \left(\frac{\Gamma}{2} - \frac{\Gamma^3}{16} + \dots\right)}\right] \quad (1.8)$$

The number of terms required for evaluating the Bessel function is determined by the magnitude of the phase dither amplitude Γ . Moreover, the expression for the phase difference is independent of the power in the individual interferometer arms. The respective signs of the measured amplitudes $A(\omega)$ and $A(2\omega)$ are used to uniquely determine the quadrant of the phase difference $\Delta\phi$.

1.2.2 System Requirements for Combining GaAs-AlGaAs Integrated Optics and Electronic Circuitry

For this research the proof-of-concept devices were operated with off-chip control electronics. The long-term goal of this project, however, is to incorporate the optics, as well as the electronic circuitry on the same chip. Thus care was taken to ensure compatibility with the goal of monolithic integration in the future. The principal circuit requirements for implementing the phase measurement and correction system include the following:

- Sample and hold circuits to measure the amplitudes of the first and second harmonic of the dither frequency
- An oscillator for the dither frequency, and a frequency doubler to generate a reference for synchronous detection of the second harmonic
- A divider, arctan, and quadrant detection circuits for calculating the phase difference.

The complexity of the actual electronic circuit designs depends on the required accuracy of the phase measurement and correction system, and the desired speed of operation.

There are two major approaches to combined integration of the optics and electronics. Both, the optical and electronic components can be fabricated in the GaAs-AlGaAs material system. There is no fundamental obstacle to the fabrication of all the electronic circuitry in GaAs. However, since the technology

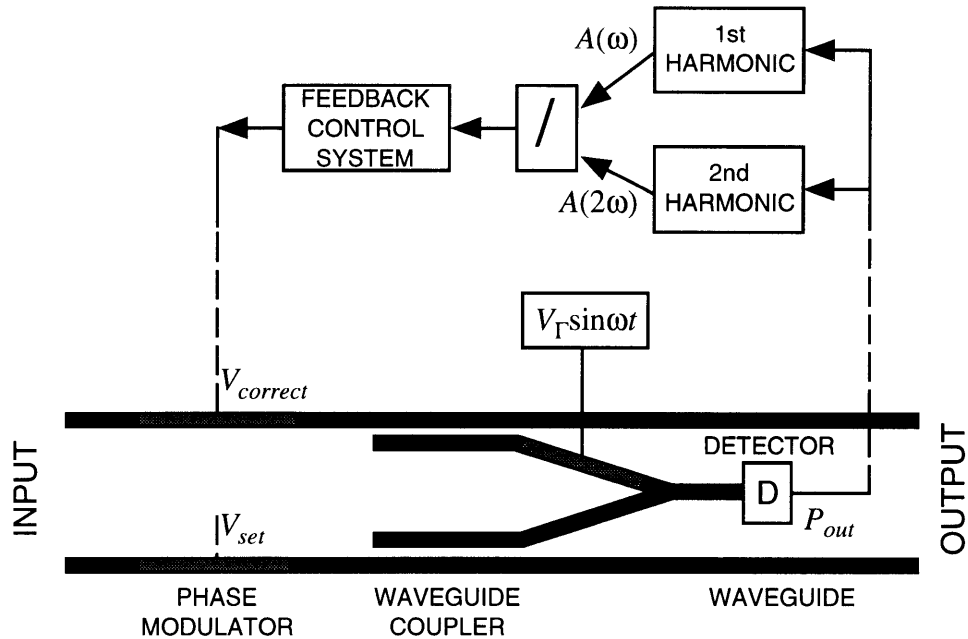


Figure 1-3: Basic module for a phase measurement and correction system. $V_{correct}$ is used to control the relative phase, whereas V_{set} can be used to induce an intentional phase imbalance when testing the device.

for fabricating GaAs electronic devices is less mature than for Silicon based devices, a hybrid technology is of interest. Hybrid techniques take advantage of the mature silicon fabrication technology to implement the necessary electronics, whereas GaAs materials can be used to fabricate the desired optical devices. In this integration scheme the GaAs-AlGaAs epitaxial layers would be grown on silicon substrates [22]. The silicon electronic devices can be fabricated first using commercial processing facilities. This is followed by the growth of the GaAs-AlGaAs epitaxial layers and the fabrication of the optical components. Work on hybrid devices for integrating silicon based electronics and GaAs optical devices is presently conducted by Prof. Fonstad at MIT.

1.3 Thesis Outline

This thesis is the continuation of the work conducted by Suzanne Lau [17] with the ultimate goal to fabricate an all-integrated optical phase front correcting device. Suzanne Lau in her work demonstrated that an integrated Mach-Zender interferometer can measure the relative phase between the two interferometer arms. The measured phase was independent of the power imbalance between the

two interferometer arms, and could be dynamically corrected by applying a voltage to the integrated phase modulators.

This work build on the results obtained by Suzanne Lau and further explored additional aspects of implementing an all-integrated optical phase correcting system. This thesis demonstrated the ability of measuring the phase between two waveguides by using a small portion of the power in each waveguide for the phase measurement. In this aspect an external detector was used to record the test interference signal used for evaluating the phase difference. Following this an integrated photodetector, fully compatible with the waveguide components and modulators, was successfully implemented and tested. Finally, the waveguide phase measurement setup was combined with the integrated detector and a phase measurement was successfully demonstrated using only integrated optical components.

2 Modeling and Design of Integrated Semiconductor Optical Components

2.1 Modeling of Dielectric Optical Waveguides

Dielectric optical waveguides are the basis of the field of integrated optics. Thus the first step to the implementation of an integrated optical device is the design of a structure which can confine and guide electromagnetic radiation - light. The confinement of light in one direction can be achieved by simply taking advantage of dielectric slab waveguides. However, for integrated optical applications it is necessary to confine the light in both the lateral, as well as the vertical direction. Waveguide structures of this kind are commonly referred to as *channel waveguides*. A few examples of such structures are show in Figure 2-1. The choice of a particular waveguide structure depends on its application, as well as the desired device characteristics, materials used, and ease of fabrication.

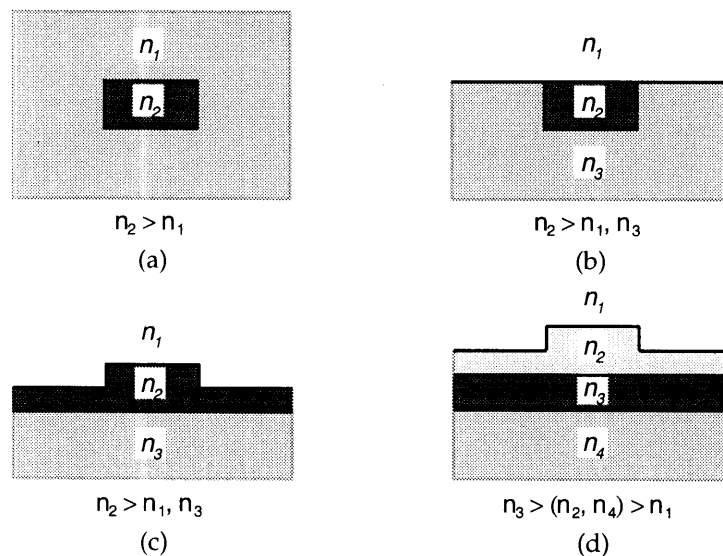


Figure 2-1: Cross sections of channel waveguide structures: (a) buried guide, (b) embedded strip guide, (c) rib guide, (d) loaded strip guide.

2.1.1 Dielectric-loaded Strip Waveguides

The dielectric-loaded strip waveguide design, shown schematically in Figure 2-2, was chosen for this research. Vertical light confinement, x-direction, is

achieved with the 4-layer dielectric nature of this structure. On the other hand, the lateral confinement of the optical mode, y -direction, is the result of the rib in the upper cladding. In such a structure, the thickness of the waveguide layer, and the rib height, determine the degree of lateral confinement and as such the propagation constant of the guided optical mode. When fabricating this structure it is important that one choose a fabrication technique which allows precise rib height control. Moreover, the thickness of the lower cladding must be sufficient so that a 4-layer slab analysis can be applied in the x -direction.

The exact analysis and calculation of the mode propagation constant in a dielectric-loaded strip waveguide is quite difficult, and only possible using numerical methods. However, for most applications one can resort to approximate methods which yield results in close agreement with the ones obtained using more exact methods.

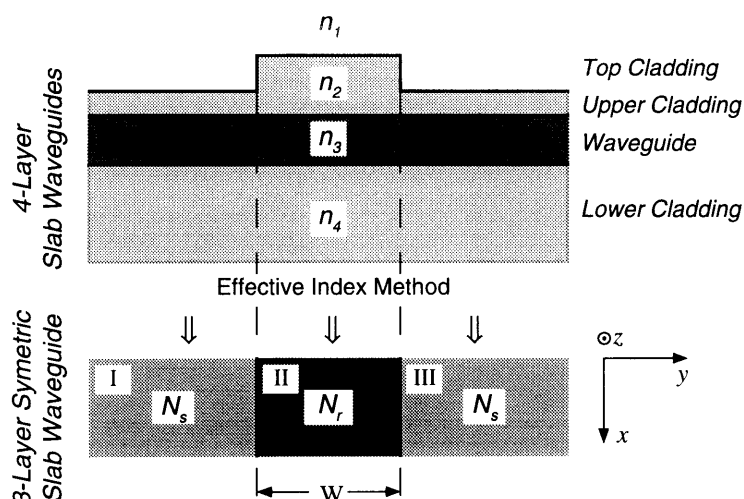


Figure 2-2: Schematic of a dielectric-loaded strip waveguide.

2.1.2 The Effective Index Method

The effective-index method (EIM) is one of the most commonly used methods for analyzing channel waveguides. This method has proven itself by producing results which are in close agreement with more exact computer results, as well as experimental results for a considerable number of practical guide structures [23].

The effective index method allows us to reduce the dielectric loaded ridge waveguide, to a simpler 3-layer symmetric waveguide. The dielectric loaded-strip

waveguide can be divided into three regions consisting of four dielectric layers each. If we treat each of these regions independently, and assume that the layers are of infinite extent in the y -direction, we obtain a set of three four-layer dielectric slab waveguide problems (since outer two slab regions are identical, so that the problem reduces to only two regions). Thus, we can calculate the effective indices N_s and N_r from the slab mode propagation constants, $\beta_{s,r}=2\pi N_{s,r}/\lambda$. If both slab regions support only a single mode, an unique effective index for each region can be determined, and such loaded-strip waveguide structure will support modes which have only one maximum in the x -direction.

After establishing effective indices for each region, the structure can be modeled as a 3-layer symmetric slab waveguide in the y - z plane (see Figure 2-2). The slabs are of uniform extent in the x -direction with an index N_s in the cladding region, and N_r in the guiding region. The analysis of this effective 3-layer slab structure yields an overall β and lateral propagation constants for the y -direction. Since these channel waveguides are designed for single-mode, quasi-transverse electric (TE) propagation, the electric field is predominantly in the y -direction. Thus, the TE slab boundary conditions are used in evaluating the 4-layer eigenvalues, and the transverse magnetic (TM) slab boundary conditions are used for the lateral 3-layer guide calculations.

Four-Layer Slab Waveguides

Maxwell's equations for a homogeneous dielectric medium of permittivity ϵ and permeability μ with no free charges present, as well as no current distributions are:

$$\nabla \times \mathbf{E}(\mathbf{r}, t) = -\mu \frac{\partial}{\partial t} \mathbf{H}(\mathbf{r}, t) \quad (2.1)$$

$$\nabla \times \mathbf{H}(\mathbf{r}, t) = -\epsilon \frac{\partial}{\partial t} \mathbf{E}(\mathbf{r}, t) \quad (2.2)$$

$$\nabla \cdot \epsilon \mathbf{E}(\mathbf{r}, t) = 0 \quad (2.3)$$

$$\nabla \cdot \mu \mathbf{H}(\mathbf{r}, t) = 0 \quad (2.4)$$

The general wave equation for the electric field is obtained from Maxwell's equations such that

$$\nabla^2 \mathbf{E}(\mathbf{r}, t) - \mu \omega \frac{\partial^2}{\partial t^2} \mathbf{E}(\mathbf{r}, t) = 0 \quad (2.5)$$

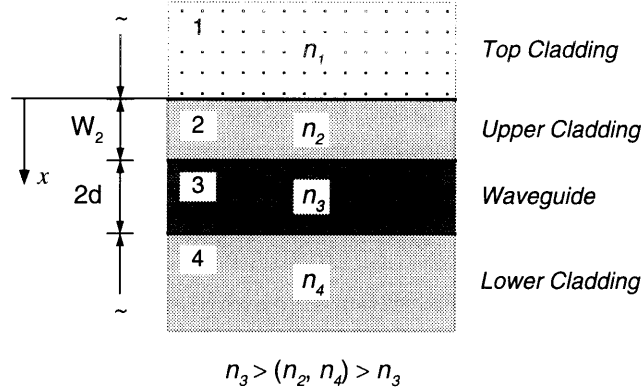


Figure 2-3: Four-layer slab waveguide. The structure is uniform in the y - z plane.

Applying our assumption of a planar slab waveguide (of infinite extent in the y -direction), we can eliminate one dimension to the wave equation since it is given that $\partial/\partial y=0$. For the case of transverse electric (TE) slab modes, where $\mathbf{E}(\mathbf{r}, t) = E(x, z, t)\hat{y}$, the following relations between the electric and magnetic field can be obtained

$$H_y = E_x = E_z = 0 \quad (2.6)$$

$$H_x = -\frac{\beta}{\omega\mu} E_y \quad (2.7)$$

$$H_z = \frac{j}{\omega\mu} \frac{\partial}{\partial x} E_y \quad (2.8)$$

To establish the modes propagating in a four-layer dielectric slab waveguide structure one has to find solutions which satisfy the wave Equation (2.5). Moreover, the boundary conditions require that E_y and H_z be continuous across the layer boundaries. Since μ is the same in all the layers, the continuity in H_z is equivalent to the continuity of $\partial E_y/\partial x$. The Equations (2.9)-(2.12) satisfy the wave Equation (2.5) in the applicable regions, and Equations (2.13)-(2.16) are the respective derivatives $\partial E_y/\partial x$ which are required to be continuous across the dielectric layer boundaries .

$$\text{Layer 1. } E_y = A_1 e^{\gamma_1 x} \quad (2.9)$$

$$\text{Layer 2. } E_y = A_2 \cosh \gamma_2 x + B_2 \sinh \gamma_2 x \quad (2.10)$$

$$\text{Layer 3. } E_y = A_3 \cos k_x u + B_3 \sin k_x u, u = x - (W_2 + d) \quad (2.11)$$

$$\text{Layer 4. } E_y = A_4 e^{-\gamma_4 v}, v = x - (W_2 + 2d) \quad (2.12)$$

$$\text{Layer 1. } \frac{\partial E_y}{\partial x} = \gamma_1 A_1 e^{\gamma_1 x} \quad (2.13)$$

$$\text{Layer 2. } \frac{\partial E_y}{\partial x} = \gamma_2 (A_2 \sinh \gamma_2 x - B_2 \cosh \gamma_2 x) \quad (2.14)$$

$$\text{Layer 3. } \frac{\partial E_y}{\partial t} = -k_x (A_3 \sin k_x u - B_3 \cos k_x u) \quad (2.15)$$

$$\text{Layer 4. } \frac{\partial E_y}{\partial x} = -\gamma_4 A_4 e^{-\gamma_4 v} \quad (2.16)$$

The quantities $\gamma_1, \gamma_2, \gamma_4$ are the field amplitude decay constants in the layers 1,2 and 4, whereas k is the propagation constant in the x -direction of layer 3, and β is the propagation constant in the z -direction. The quantities $\gamma_1, \gamma_2, \gamma_4$, and k are all related as follows:

$$\gamma_1 = (\beta^2 - k_1^2)^{1/2} \quad (2.17)$$

$$\gamma_2 = (\beta^2 - k_2^2)^{1/2} = k_0 (N_{eff}^2 - n_2^2)^{1/2} \quad (2.18)$$

$$\gamma_4 = (\beta^2 - k_4^2)^{1/2} \quad (2.19)$$

$$k_x = (k_3^2 - \beta^2)^{1/2} = k_0 (n_3^2 - N_{eff}^2)^{1/2} \quad (2.20)$$

where $k_0 = 2\pi/\lambda$ and $k_i = (2\pi/\lambda)n_i, i=1\dots 4$, λ is the operating wavelength, and N_{eff} is the effective index of the waveguide structure. By matching the boundary conditions for E_y and $\partial E_y/\partial x$, and solving the system of linear equations for the propagation constants, the following eigenvalue equation is obtained:

$$\tan(2k_x d) = \frac{k_x [\gamma_4 (\gamma_2 + \gamma_1 \tanh \gamma_2 W_2) + \gamma_2 (\gamma_1 + \gamma_2 \tanh \gamma_2 W_2)]}{k_x^2 (\gamma_2 + \gamma_1 \tanh \gamma_2 W_2) - \gamma_2 \gamma_4 (\gamma_1 + \gamma_2 \tanh \gamma_2 W_2)} \quad (2.21)$$

Equation (2.21) is a transcendental equation which relates the structure parameters to the propagation constants. Since there is no analytical solution to Equation (2.21), a solution for k can be found only numerically. However, a solution for k exists only if the thickness of the guiding layer (layer 3) is larger than the cutoff thickness of the fundamental mode. This cutoff thickness is given by

$$t_{cutoff} = \frac{1}{k_x} \arctan \left[\frac{\gamma_2 (\gamma_1 + \gamma_2 \tanh \gamma_2 W_2)}{k_x (\gamma_2 + \gamma_1 \tanh \gamma_2 W_2)} \right] \quad (2.22)$$

If the guiding layer is thicker than the cutoff thickness the total number of propagating guided modes, m , can be obtained from the condition,

$$t_{cutoff} + \frac{(m-1)\pi}{k_x} \leq 2d \quad (2.23)$$

Summarizing, by solving Equation (2.21) and using Equation (2.20) one can obtain the propagation constants β for the individual guided modes. Thus if the four-layer structure supports only one guided mode, an unique effective index $N_{eff} = \beta/k_0$ can be obtained.

Three-Layer Symmetric Slab Waveguides

When calculating the propagating modes in a three-layer slab structure one has to start with the wave equation. For the EIM analysis of the loaded strip waveguide structure, the modes in the three-layer symmetric slab waveguide have to satisfy the transverse magnetic (TM) boundary conditions. Thus, to simplify the analysis, instead of the E -field wave equation the H -field wave equation is used. The general form of the wave equation for the H -field is obtained from Maxwell's equation, and is given by

$$\nabla^2 \mathbf{H}(\mathbf{r}, t) - \mu \varepsilon \frac{d^2}{dt^2} \mathbf{H}(\mathbf{r}, t) = 0 \quad (2.24)$$

Applying our assumption of a planar slab waveguide (of infinite extent in

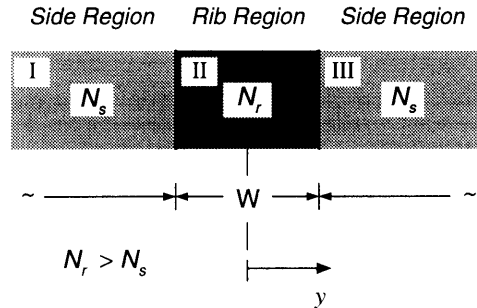


Figure 2-4: Three-layer symmetric slab waveguide. The structure is uniform in the x - z plane. The indices N_s and N_r are obtained using the effective index method.

the x -direction), we can eliminate one dimension to the wave equation since it is given that $\partial/\partial x=0$. For the case of TM slab modes, where $\mathbf{H}(\mathbf{r}, t) = H(y, z, t)\hat{x}$, the following relations between the electric and magnetic field can be obtained

$$E_x = H_y = H_z = 0 \quad (2.25)$$

$$E_y = \frac{\beta}{\omega\epsilon} H_x \quad (2.26)$$

$$E_z = -\frac{j}{\omega\epsilon} \frac{\partial}{\partial y} H_x \quad (2.27)$$

The boundary conditions require that H_x and E_z be continuous across the layer boundaries. The Equations (2.9)-(2.12) satisfy the wave Equation (2.24) in the applicable regions, and Equations (2.13)-(2.12) are the respective expressions for $E_z = -(j/\omega\epsilon)\partial H_x/\partial y$ which are required to be continuous across the dielectric layer boundaries.

$$\text{Layer I } H_x = A_I e^{\gamma_s(y+W/2)} \quad (2.28)$$

$$\text{Layer II } H_x = A_{II} \cos k_y y \quad (2.29)$$

$$\text{Layer III } H_x = A_{III} e^{-\gamma_s(y-W/2)} \quad (2.30)$$

$$\text{Layer I } E_z = \left(\frac{-j}{\omega\epsilon_s}\right) \gamma_s A_I e^{\gamma_s(y+W/2)} \quad (2.31)$$

$$\text{Layer II } E_z = \left(\frac{-j}{\omega\epsilon_r}\right) k_y A_{II} \cos k_y y \quad (2.32)$$

$$\text{Layer III } E_z = \left(\frac{-j}{\omega\epsilon_s}\right) \gamma_s A_{III} e^{-\gamma_s(y-W/2)} \quad (2.33)$$

The quantity γ_s is the field amplitude decay constant in cladding layers I and III, k_y is the propagation constant in the y -direction of layer II, and β is the propagation constant in the z -direction. The quantities γ_s , k_y and β are all related as follows:

$$\gamma_s = (\beta^2 - k_s^2)^{1/2} = k_0 (N_{eff}^2 - N_s^2)^{1/2} \quad (2.34)$$

$$k_y = (k_r^2 - \beta^2)^{1/2} = k_0 (N_r^2 - N_{eff}^2)^{1/2} \quad (2.35)$$

where $k_0 = 2\pi/\lambda$, λ is the operating wavelength, N_r and N_s are the effective indices of the ridge and side region, and $\beta = 2\pi N_{eff}/\lambda$. By matching the boundary conditions for H_x and E_z at $y = \pm W/2$, and solving the system of linear equations for the propagation constants, the following eigenvalue equation is obtained:

$$\tan\left(k_y \frac{W}{2}\right) = \left(\frac{N_s}{N_r}\right)^2 \left(\frac{\gamma_s}{k_y}\right) \quad (2.36)$$

Equation (2.36) is the transcendental eigenvalue equation which relates the structure parameters to the propagation constants. As with the four-layer

structure a solution can be found only numerically. For the three-layer structure there is no cutoff thickness for the fundamental mode, and there is always at least one guided mode present. The total number of propagating modes, m , corresponds to the condition

$$(m - 1) \frac{\pi}{\gamma_s} < W \quad (2.37)$$

The propagation constant β obtained as result of the EIM and the three-layer symmetric dielectric guide analysis above, is considered to be the propagation constant of the loaded-strip waveguide structure as a whole. If Equation (2.37) yields an $m=1$ (and the four-layer structures were single mode as well) the structure as a whole is expected to support only one guided mode.

2.1.3 Optical Loss in Dielectric Waveguides

An important consideration when designing dielectric optical waveguides is the amount of propagation loss of the optical mode in a particular structure. In general, losses in semiconductor waveguides can be attributed to absorption, scattering, and radiation.

Losses due to absorption can be of various sources, but in semiconductor waveguides band-edge absorption and free-carrier absorption are of primary concern. Band-edge absorption can be avoided if the material is chosen in such a way that the optical mode has a wavelength which is much longer than the wavelength corresponding to the bandgap. In the GaAs material system an increase in the bandgap can be achieved by choosing a high enough aluminum concentration for the $\text{Al}_x\text{Ga}_{1-x}\text{As}$ waveguide layers: increasing the aluminum concentration increases the bandgap energy and thus decreases the bandgap wavelength. For $\text{Al}_x\text{Ga}_{1-x}\text{As}$ semiconductors, the bandgap energy (in eV) is related to the composition x (for $0 \leq x \leq 0.4$) by [24]

$$E_g = 1.424 + 1.245x \quad (2.38)$$

The presence of free-carriers not only reduces the real part of the dielectric constant, but also increases the absorption of the semiconductor [23]. The free-carrier absorption is proportional to the number of free-carriers. Thus, free-carrier absorption can be minimized by growing epitaxial waveguide layers of material which is nominally undoped (as close as possible to intrinsic). The waveguide epitaxial structures for this research were grown by organometallic chemical vapor

phase epitaxy (OMVPE) with $n \approx 10^{15} \text{cm}^{-3}$ and $n \approx 10^{16} \text{cm}^{-3}$ for the GaAs and AlGaAs films respectively.

There are two sources of scattering loss in optical waveguides: volume scattering and surface scattering. Volume scattering is caused by imperfections within the volume of the waveguide. However, in all waveguides of interest, the number and size of imperfections is so small that volume scattering is negligible compared to surface scattering loss. Surface scattering losses are largely due to roughness at boundaries between the dielectric waveguide layers. Moreover, scattering losses are generally higher at boundaries where the refractive index changes Δn are greater. As a result, the loaded strip waveguides are less susceptible to interface roughness than ridge waveguides (see Figure 2-1). For loaded strip waveguides the fraction of the total optical mode intensity near the semiconductor-air interface (Δn large) is much smaller, resulting in less scattering loss for the same roughness profile [25]. To reduce scattering losses it is important to fabricate smooth dielectric interface layers, particularly if the Δn is large.

Optical energy can be lost from the waveguides by radiation, in which case optical energy is emitted into the material surrounding the waveguide without being guided. If the substrate is of larger index of refraction than the adjacent cladding layer, part of the waveguide mode may couple into substrate radiation modes. This type of attenuation can be minimized by reducing the coupling between the waveguide and substrate. This can be achieved by increasing the lower cladding thickness or increasing the vertical mode confinement [26].

Radiation losses occur at waveguide bends, changes in guide dimensions, and guide discontinuities [27] [23]. In fact, the limit on how much a waveguide can change direction per unit length, is set by the maximum acceptable loss for a given device. Since for most integrated optical devices waveguide bending is needed, radiation losses from curved waveguides must be considered in the device design. The waveguide bends have the effect of creating a disparity between the traveling distance of the evanescent mode tails along the inner and outer waveguide sides. This introduces coupling between the guided modes and radiation modes and as such introduces loss. The loss at abrupt bends decreases with increased lateral mode confinement, as well as smaller bend angles (less abrupt direction changes).

2.1.4 Index of Refraction in GaAs-Al_xGa_{1-x}As

The index of refraction of Al_xGa_{1-x}As can be controlled by the percentage of aluminum in the compound: the refractive index increases as the aluminum content decreases [28] [24]. *Casey et al.* [28] have measured the refractive index as function of energy for Al_xGa_{1-x}As films with aluminum compositions $0 \leq x \leq 0.38$. The refractive index of an Al_xGa_{1-x}As film depends nonlinearly on the aluminum concentration x and the operating wavelength λ . Since the experimentally obtained data are awkward for use in numerical modeling of waveguide structures, an alternate means of determining the refractive index of Al_xGa_{1-x}As is widely used.

In numerical modeling of the Al_xGa_{1-x}As structures ($0 \leq x \leq 0.40$), the refractive indices were calculated using the following Sellmeier equation

$$n^2 = (10.906 - 2.92x) + \frac{0.97501}{\lambda^2 - (0.52886 - 0.735x)^2} - 0.002467(1.41x + 1)\lambda^2 \quad (2.39)$$

Equation (2.39) is an empirical fit to measured data [27] for the refractive index of Al_xGa_{1-x}As as a function of x and λ . This model yields refractive indices which differ slightly from the experimental data by *Casey at al.* However, even though the absolute indices differ somewhat, the difference between films of different compositions are in close agreement. Thus, since the properties of a waveguide are largely dependent on the index differences between dielectric layers, the results of numerical simulations yield accurate estimates of waveguide properties.

2.1.5 Waveguide Design and Modal Characteristics

For the purposes of this research the waveguides are designed to propagate only the lowest guided mode. The first step in designing dielectric waveguides is to determine the composition of the individual dielectric slab layers. The dielectric layer structure shown in Figure 2-5 was chosen for this research. This choice of dielectric layers makes it possible to fabricate low loss waveguides for wavelengths around $0.85\mu\text{m}$ [17]. Moreover, this structure is fully compatible with the fabrication of other integrated optical components needed for this research. The n^+ doped lower cladding region is not needed for the waveguide design, but it actually may be causing some guiding loss. However, this layer is required for the implementation of integrated phase modulators discussed in Section 2.3. Once the composition and thicknesses of the individual dielectric layers was chosen, the

device performance was determined by the specific wavelength used, waveguide rib width, and height.

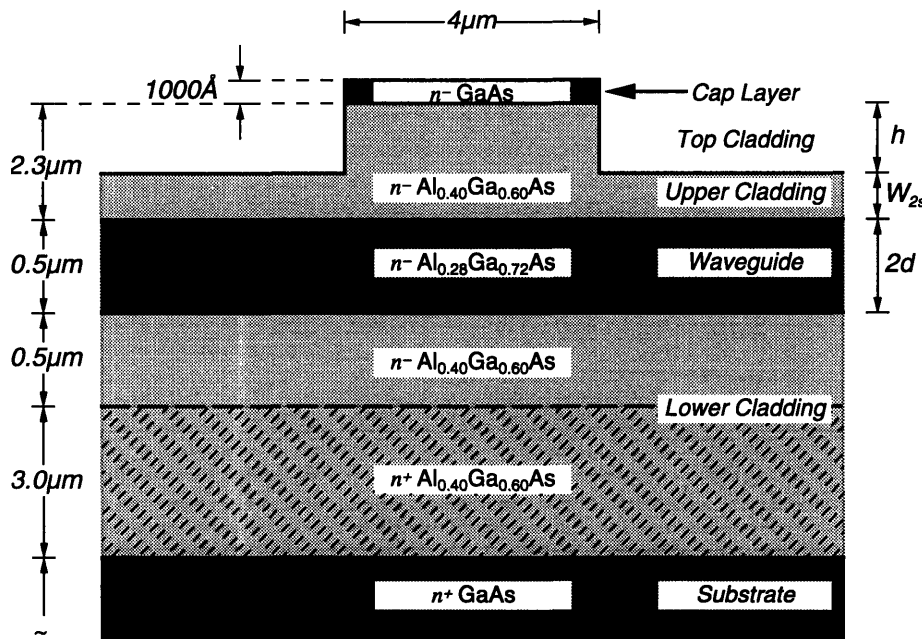


Figure 2-5: Dielectric-loaded strip waveguide cross section.

A number of numerical simulations of loaded-strip structures using the layer composition shown in Figure 2-5 was performed. For single mode operation, the rib width was chosen to be $4\mu\text{m}$, and was set by the photolithographic mask used for waveguide patterning. This width yields good single mode performance and is large enough to ensure consistent fabrication results. Thus, the only fabrication dependent variable was the actual rib height, which was controlled through the etching process.

The y -direction propagation constant (proportional to the mode confinement) was observed as a function of wavelength λ , and W_{2d} the side cladding thickness. In Figure 2-6 it can be seen that this particular loaded strip waveguide structure becomes more single mode as the wavelength decreases. This effect is a result of the change in the index of refraction of the individual AlGaAs layers with wavelength, and the change in the mode shapes of the four layer waveguide slabs it affects. As a consequence, the effective index of the side region N_s changes faster than that of the rib region N_r , resulting in smaller mode confinement. Thus, for the loaded strip waveguides structure an increase in excitation wavelength results in a larger cut-off width for the second guided mode.

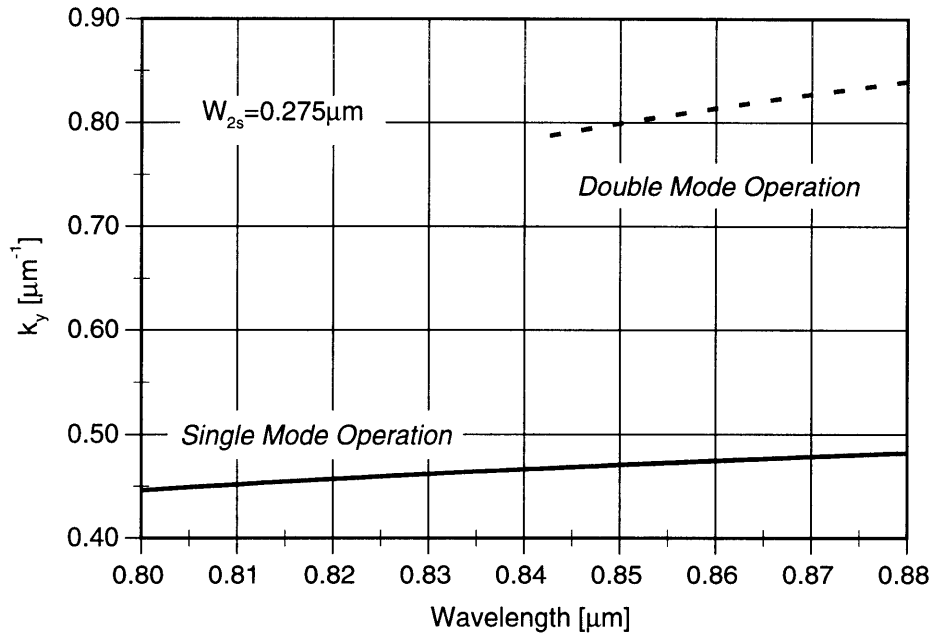


Figure 2-6: Dependence of the y-direction propagation constant k_y on the wavelength.

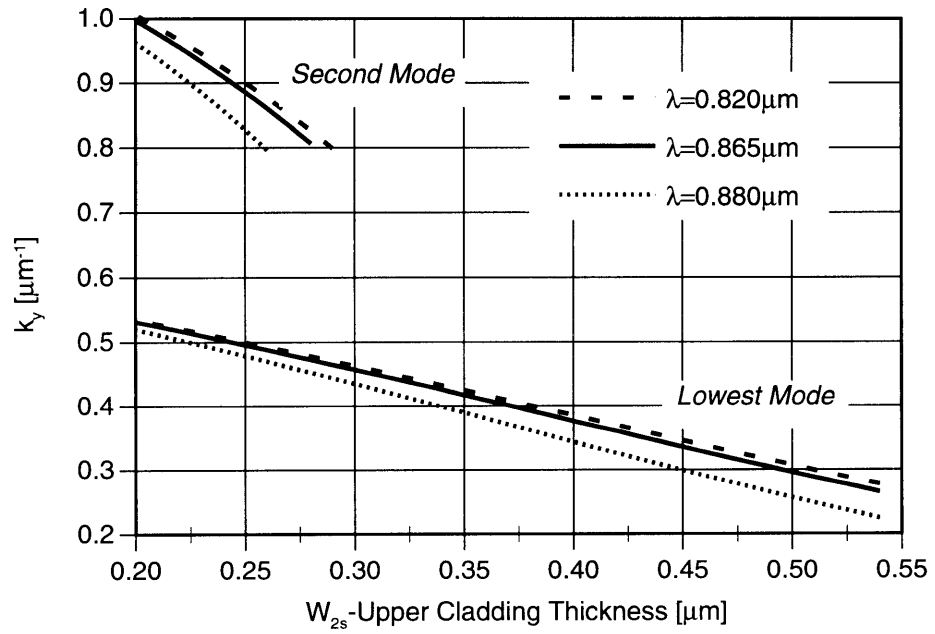


Figure 2-7: Dependence of the y-direction propagation constant k_y on W_{2s} .

When fabricating actual waveguides it is of interest how the change in fabrication parameters will affect the waveguide performance. Since the waveguide rib was fabricated by etching off the side regions, it was of interest how the device performance depended on changes in W_{2d} . Figure 2-6 shows how the k_y depends on W_{2d} at three particular wavelengths for the structure shown in Figure 2-5. The actual target value for W_{2d} was determined by considering the performance of other integrated optical components used in this project.

2.2 Modeling of Dielectric Waveguide Couplers

Waveguide couplers are integrated optical devices which perform the function of beam-splitters in bulk optics. They make it possible to split the power from one (loaded-strip) waveguide into two or more guides. One of the simplest coupler implementations consists of two parallel waveguides in close proximity to each other. Under these conditions, a fraction of the field in one guide interacts with the adjacent guide resulting in a power transfer. The power transfer is not unidirectional, but the power is exchanged back-and-forth between the guides as often as the length of the device permits it. Full power transfer however, is only possible for guides which have equal propagation constants in isolation. Guides with equal propagation constants are referred to as synchronous waveguides. Equal propagation constants, at all wavelengths, generally occur only when the two adjacent guides are identical. Nevertheless, under specific conditions, for particular wavelengths, it is possible that two dissimilar waveguides are synchronous and full power exchanges are possible [29].

The coupler operation can be described by the interaction of the orthogonal modes of the coupler structure. The waveguide coupler as a whole has a different set of normal modes than the individual waveguides. Thus, the power transfer within the waveguide coupler is described by the propagation of the modes of the coupler structure. If the field at the waveguide input is $\mathbf{E}(x,y)$, its propagation can be described in terms of the orthonormal set of guided modes \mathbf{F}_i and radiation modes $\mathbf{R}(\beta)$ of the coupler structure

$$\mathbf{E}(x, y, z) = a_1 \mathbf{F}_1 e^{j\beta_1 z} + a_2 \mathbf{F}_2 e^{j\beta_2 z} + \dots + \int b(\beta) \mathbf{R}(\beta) e^{j\beta z} d\beta \quad (2.40)$$

To describe the coupler operation using Equation (2.40) all the guided and radiation modes of the compound structure have to be calculated. In general, it can be assumed that it is too complicated to easily compute all the normal modes

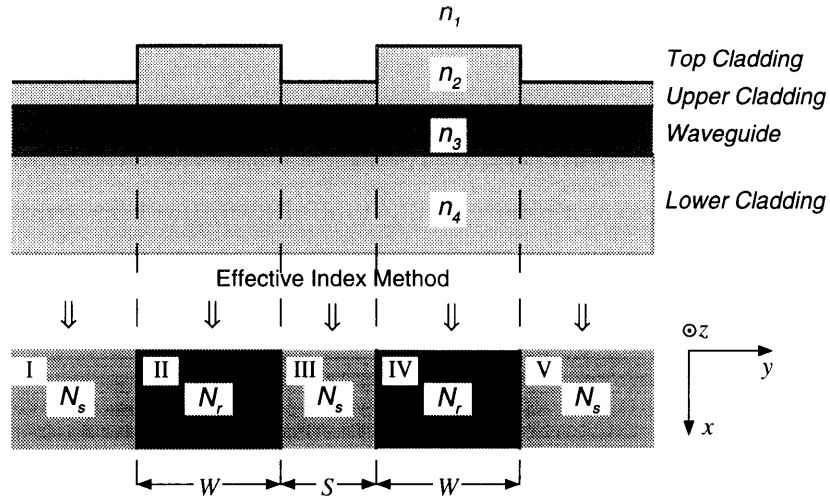


Figure 2-8: Schematic of a waveguide coupler. Two dielectric-loaded strip waveguides are separated by a distance S . The structure of two adjacent dielectric-loaded strip waveguides is reduced to a one dimensional, five-layer slab waveguide problem.

and their propagation constants. Thus, for many practical applications, the operation of waveguide couplers can be approximately described by the coupled-mode analysis [30].

The couplers used in this project consist of two single-mode waveguides which are separated by a distance S . The analysis of the structure is started by applying the EIM to reduce the two dimensional loaded strip waveguide to an one dimensional five-layer slab structure. Analogous to the single loaded strip waveguide analysis, TE boundary conditions are applied to solve the vertical four-layer structure to obtain the applicable effective indices. TM boundary conditions are applied for solving the slab coupler in the y -direction.

2.2.1 Coupled-Mode Theory Coupler Analysis

When analyzing waveguide couplers using the coupled-mode formalism, it is assumed that the two guides interact only weakly. The only interaction between the waveguides takes place via their fringe fields. It is assumed that the field at the coupler input, and its propagation, is fully described by the superposition of the lowest even and odd guided mode of the compound structure. Since the input is the superposition of the even and odd modes with different propagation constants, β_e and β_o , the relative phase between them will change as they propagate along z . Thus, if the fields were initially in-phase, they will be out-of-phase at $z=\pi/(\beta_e-\beta_o)$.

If at $z=0$ the total field in the coupler was the sum of the lowest even and odd mode, at $z=l$ this will correspond to the difference between the two modes. In effect, after an interaction length of L , all the power is transferred from one waveguide to the other. The propagation of the sum and difference fields can be described by two coupled first-order differential equations.

Coupled Equations for the Sum and Difference Fields

The input field at the coupler is the linear superposition of the compound structure modes. The fields G_1 and G_2 are the normalized fields in each of the coupler waveguides, F_e and F_o are the even and odd normal modes respectively. The coefficients which relate $G_{1,2}$ and $F_{1,2}$ can be defined as follows:

$$G_1 = c_1 F_e + c_2 F_o \quad (2.41)$$

$$G_2 = c_3 F_e + c_4 F_o \quad (2.42)$$

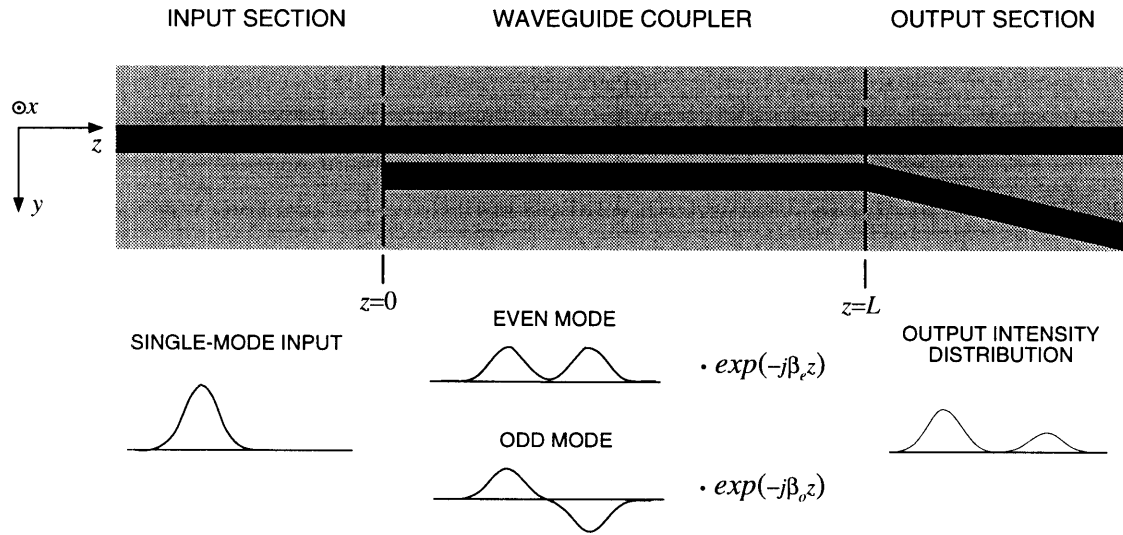


Figure 2-9: Top view of a synchronous waveguide coupler with a single-mode input waveguide. The input field can be expressed as the superposition of the even and odd mode of the compound coupler structure.

To describe the propagation and changing field pattern, z -dependent coefficients $a_1(z)$ and $a_2(z)$ for the field patterns G_1 and G_2 have to be introduced. Moreover, initial amplitude coefficients for F_e and F_o have to be defined. Thus, the propagation of the total field in the waveguide coupler can be expressed as:

$$a_1(z)G_1 + a_2(z)G_2 = b_1 F_e e^{-j\beta_c z} + b_2 F_o e^{-j\beta_o z} \quad (2.43)$$

Substituting (2.41) and (2.42) into (2.43), and grouping the coefficients for F_e and F_o respectively lead to the relationships

$$c_1 a_1(z) + c_3 a_2(z) = b_1 e^{-j\beta_e z} \quad (2.44)$$

$$c_2 a_1(z) + c_4 a_2(z) = b_2 e^{-j\beta_o z} \quad (2.45)$$

To obtain the change of the input fields with respect to z , Equations (2.44) and (2.45) are differentiated with respect to z , and the constants b_1 and b_2 are eliminated,

$$c_1 \frac{da_1}{dz} + c_3 \frac{da_2}{dz} = -j\beta_e (c_1 a_1 + c_3 a_2) \quad (2.46)$$

$$c_2 \frac{da_1}{dz} + c_4 \frac{da_2}{dz} = -j\beta_o (c_2 a_1 + c_4 a_2) \quad (2.47)$$

After solving Equations (2.46) and (2.47) for the da_1/dz and da_2/dz , the desired coupled-mode equations are obtained

$$\frac{da_1}{dz} = -j\beta_1 a_1 + \kappa_{12} a_2 \quad (2.48)$$

$$\frac{da_2}{dz} = -j\beta_2 a_2 + \kappa_{21} a_1 \quad (2.49)$$

The quantities β_1 and β_2 are the propagation constants for the two waveguides in isolation, and can be related to the coupler modes as follows

$$\beta_1 = \frac{c_1 c_4 \beta_e - c_2 c_3 \beta_o}{c_1 c_4 - c_2 c_3}, \beta_2 = \frac{c_1 c_4 \beta_o - c_2 c_3 \beta_e}{c_1 c_4 - c_2 c_3} \quad (2.50)$$

The coupling coefficients κ are defined by

$$\kappa_{12} = -j \frac{c_3 c_4}{c_1 c_4 - c_2 c_3} (\beta_e - \beta_o), \kappa_{21} = j \frac{c_1 c_2}{c_1 c_4 - c_2 c_3} (\beta_o - \beta_e) \quad (2.51)$$

From the Equations (2.48) and (2.49) the general solutions for the propagating fields in both waveguides can be found to be:

$$a_1(z) = \left[a_1(0) \left(\cos \beta_0 z + j \frac{\beta_2 - \beta_1}{2\beta_0} \sin \beta_0 z \right) + \frac{\kappa_{12}}{\beta_0} a_2(0) \sin \beta_0 z \right] e^{-j[(\beta_1 + \beta_2)/2]z} \quad (2.52)$$

$$a_2(z) = \left[\frac{\kappa_{12}}{\beta_0} a_1(0) \sin \beta_0 z + a_2(0) \left(\cos \beta_0 z + j \frac{\beta_1 - \beta_2}{2\beta_0} \sin \beta_0 z \right) \right] e^{-j[(\beta_1 + \beta_2)/2]z} \quad (2.53)$$

where

$$\beta_0 = \sqrt{\left(\frac{\beta_1 - \beta_2}{2}\right)^2 + \kappa_{12}\kappa_{21}} \quad (2.54)$$

The solutions (2.52) and (2.53) give the fields in the coupler waveguides as a function of the input fields, the individual guide propagation constants, and the coupling constants. The field amplitudes in the individual guides oscillate between minimum and maximum values as a result of the beating of the even and odd coupler mode.

In this project the coupler consists of two identical, single-mode waveguides such that $\beta_1 = \beta_2$. The coupler is used to split the power from one guide into two such that $a_1(0) \neq 0$ and $a_2(0) = 0$. This simplifies the general propagation equations to

$$a_1(z) = a_1(0)e^{-j\beta_1 z} \cos \kappa_{12} z \quad (2.55)$$

$$a_2(z) = a_1(0)e^{-j\beta_1 z} \sin \kappa_{12} z \quad (2.56)$$

2.2.2 Evaluating the Coupling Coefficient κ

The propagation constants of the even and odd modes of a synchronous TM waveguide coupler are calculated in Appendix B. Thus, after the propagation constants are obtained, the coupling coefficient can be found using Equations (2.51). However, since for many practical applications it is difficult to obtain the exact values for β_e and β_o , an alternate method for evaluating κ must be used.

From previous assumptions, total field in the coupler is the superposition of the field patterns of the individual guides:

$$\mathbf{E}(y, z) = a_1(z)\mathbf{G}_1 + a_2(z)\mathbf{G}_2 \quad (2.57)$$

where \mathbf{G}_1 and \mathbf{G}_2 are the fields of the individual waveguides in isolation. The power from waveguide 1 is transferred to waveguide 2 by a polarization current $j\omega\mathbf{P}_{21}$ generated in waveguide 2 by the evanescent field of guide 1. The coupling polarization current is, in effect, the change in polarization current due to the presence of waveguide 2 (and its high index region)

$$j\omega\mathbf{P}_{21} = j\omega\epsilon_0 (N_r^2 - N_s^2) a_1(z)\mathbf{G}_1 \quad (2.58)$$

The power transferred per unit length, ΔP , is the overlap between the polarization current and the field in the high index region of waveguide 2 (wg2), and is derived from the Poynting equation:

$$\begin{aligned}\Delta P &= -\frac{1}{4} \left[\int_{wg2} a_2^* \mathbf{G}_2^* (j\omega\epsilon_0 \mathbf{P}_{21}) da + \text{c.c.} \right] \\ &= -\frac{1}{4} \left[\int_{wg2} a_2^* \mathbf{G}_2^* j\omega\epsilon_0 (N_r^2 - N_s^2) a_1 \mathbf{G}_1 da + \text{c.c.} \right]\end{aligned}\quad (2.59)$$

The power transfer from waveguide 1 to waveguide 2 can also be expressed from the coupled mode Equations (2.48) and (2.49) as

$$\frac{d|a_2|^2}{dz} = a_2 \frac{da_2^*}{dz} + \frac{da_2}{dz} a_2^* = a_2 \kappa_{21}^* a_1^* + a_2^* \kappa_{21} a_1 \quad (2.60)$$

Thus, by comparing the terms in (2.59) with (2.60), an expression for the coupling coefficient κ_2 can be obtained to be

$$\kappa_{21} = -\frac{j\omega\epsilon_0}{4} \int_{wg2} \mathbf{G}_2^* (N_r^2 - N_s^2) \mathbf{G}_1 da \quad (2.61)$$

The same approach yields the expression for κ_{12}

$$\kappa_{12} = -\frac{j\omega\epsilon_0}{4} \int_{wg1} \mathbf{G}_1^* (N_r^2 - N_s^2) \mathbf{G}_2 da \quad (2.62)$$

Equations (2.61) and (2.62) are an approximate alternative to Equations (2.51). These approximate expressions relate κ to parameters of the two waveguides in isolation and eliminate the need for calculating the modes of the compound coupler structure. Thus, the approximate coupling coefficient for a synchronous TM slab waveguide coupler is obtained by evaluating the overlap integral in (2.61).

$$\kappa_{12} = -j \frac{(r\gamma k_y)^2}{[k_y^2 + r^2\gamma^2] \beta (r\gamma d + 1)} e^{-\gamma S}, r = \left(\frac{N_r}{N_s} \right) \quad (2.63)$$

where γ, k_y, β are the mode constants of the TM waveguide in isolation, $2d$ the guide width, and S the separation between the adjacent guides.

2.2.3 Waveguide Coupler Design

For fabricating waveguide couplers it is important to understand how the coupling changes as a function of design parameters. Since the coupler is in effect

two waveguides in close proximity, the epitaxial layers used are identical to those used for the single-mode waveguides. Moreover, the width of the individual waveguides was set to be $4\mu\text{m}$. Thus the fabrication dependent variables left were the guide separation S , the upper cladding in the side regions W_{2d} , and the actual interaction length between the two waveguides.

Two sets of devices were designed, each having different coupler parameters. One set of couplers was designed with $S=3.4\mu\text{m}$, and the other with $S=3.6\mu\text{m}$. Once the waveguide width and separation are fixed, the coupling between the waveguides becomes a function of W_{2d} . Figure 2-10 shows how the coupling length (needed to transfer all the power from one waveguide into the other) depends on W_{2d} . However, the couplers in this project were not used for full

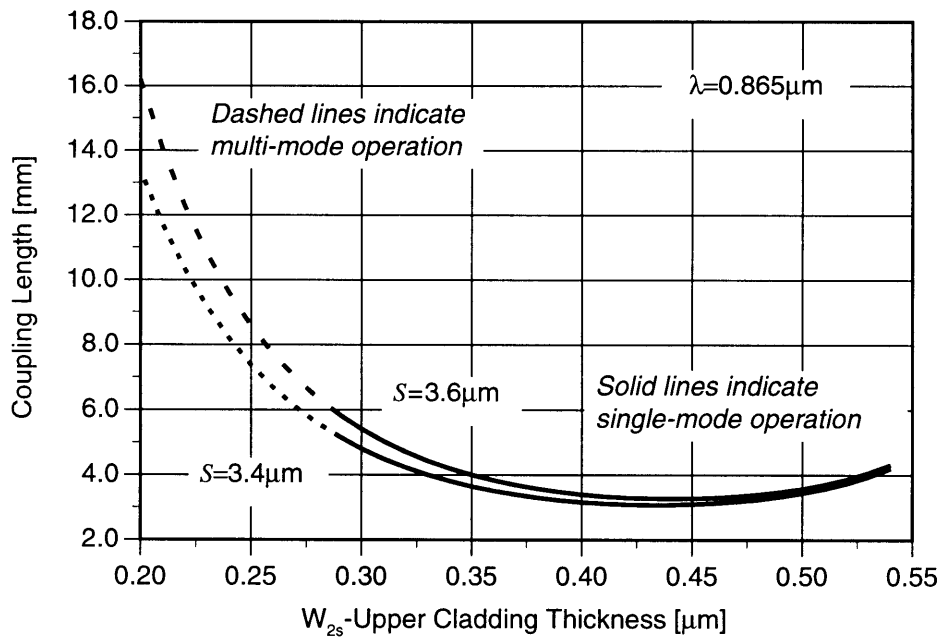


Figure 2-10: The coupling length as a function of W_{2s} for two different guide separations.

power transfer, but the interaction length was set to yield an approximate 0.10/0.90 power splitting ratio. The coupler with $S=3.4\mu\text{m}$ was made to have an interaction length $l=790\mu\text{m}$, whereas the $S=3.6\mu\text{m}$ had an interaction length $l=707\mu\text{m}$. Figures 2-11 and 2-12 show how the predicted power transfer varies with W_{2d} for different wavelengths.

The coupling coefficients κ used in the numerical simulations were evaluated using the normal modes of the compound waveguide coupler structure

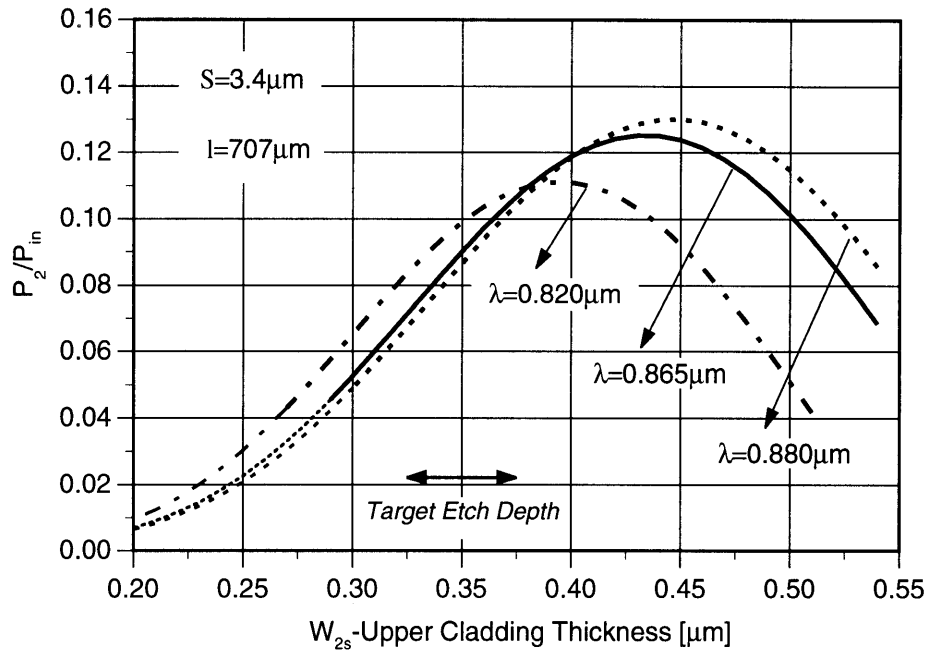


Figure 2-11: Percentage of the input power transferred into guide 2 as a function of W_{2s} for $S=3.4\mu\text{m}$ and $l=707\mu\text{m}$.

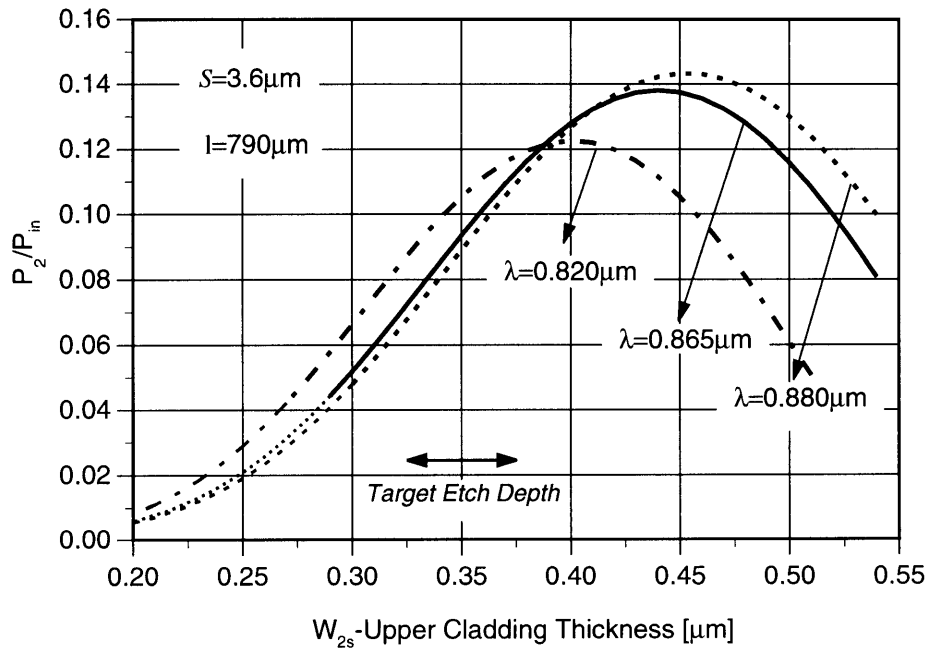


Figure 2-12: Percentage of the input power transferred into guide 2 as a function of W_{2s} for $S=3.6\mu\text{m}$ and $l=790\mu\text{m}$.

(see Appendix B). For the case of two identical, parallel waveguides, it was particularly easy to calculate the even and odd modes of the compound structure. However, in general it may be necessary to resort to the approximate method discussed in Section 2.2.2. The coupling coefficients obtained using the normal modes approach and the once obtained by using Equation (2.63) were in close agreement. One has to keep in mind that for the dielectric-loaded strip structures discussed both methods yield an approximate result since the EIM was used to simplify the analysis.

None of the above calculations performed took into account the effects of the transitions at the input or output of the actual waveguide coupler. The abrupt input transition, one isolated to two coupled waveguides, will result in radiation losses. Since the single-mode input field can only be approximated by the sum of the even and odd coupler mode, the resulting mode mismatch will in general be the source of radiation losses. Thus, the weaker the coupling (the better the approximation), the lower the radiation losses. At the output, the two parallel coupler waveguides are gradually tapered away from each other and, therefore, extend the effective interaction length [31]. While a more rapid guide separation (large angle) decreases the interaction length it introduces larger radiation losses [17]. The design of the coupler output section is, therefore, a compromise between interaction lengths and acceptable radiation losses.

2.3 Phase Modulators

Since the use of low-loss waveguide components is essential in the development of an all integrated wave front phase correcting device, the choice of phase modulator design was constrained by the compatibility with the overall system. The phase modulator design chosen for this project was the dielectric-loaded strip modulator extensively studied by Suzanne Lau [17]. This modulator is fully compatible with the waveguide design, moreover, the phase modulator insertion loss was minimized by considering the losses due to free-carrier absorption as well as electroabsorption.

A schematic of the dielectric-loaded strip phase modulator structure chosen for this project is shown in Figure 2-13. This phase modulator device is operated as a reverse biased heterojunction. In order to reduce the free-carrier absorption loss, the center waveguide modulator region was designed as a vertical (x -direction) p^+-i-n^+ structure. By selecting a p^+-i-n^+ structure, the highly doped n^+ and

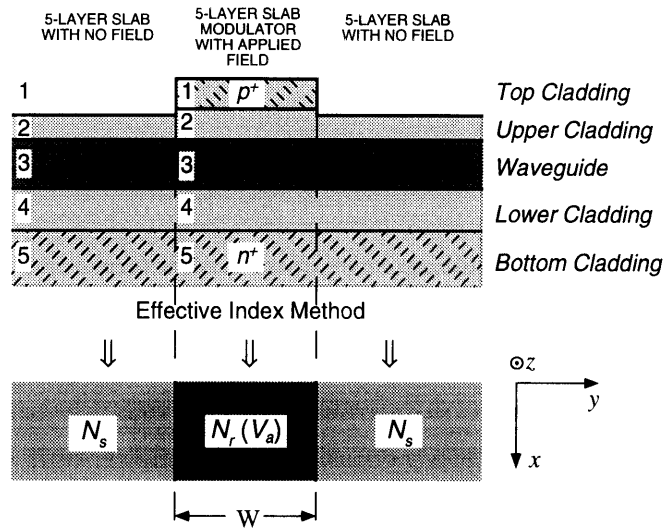


Figure 2-13: Schematic of an dielectric-loaded strip waveguide phase modulator. This modulator is operated with an reverse bias voltage.

p^+ regions are positioned in the outer cladding regions leaving the waveguide layer and some portions of the cladding nominally undoped. Such a design greatly reduces the overlap between the optical mode and the highly-doped regions, and minimizes the loss due to free-carrier absorption. However, the total thickness of the intrinsic semiconductor region is limited by the voltage required to achieve $>2\pi$ phase changes for a given modulator length. The thicker the intrinsic region, the higher the voltage required to achieve $>2\pi$ phase changes.

The reverse-biased phase modulators have to be designed such that the electroabsorption is minimized for the range of desired operating voltages. To avoid electroabsorption, the bandgap (determined by the material composition) of the waveguide material is chosen to be above the energy of the operating wavelength. However, the applied electric field induces a shift in the band-edge of the material via the Franz-Keldysh effect [32] [33] which, in effect, reduces the band gap. This voltage induced change in the bandgap has to be considered when determining the operating wavelength.

The choice of a p^+i-n^+ device structure for reducing the free-carrier absorption precludes the use of free-carrier effects to achieve phase modulation. Furthermore, the concerns for reducing losses due to electroabsorption prevent the use of electrorefraction to achieve phase modulation. The phase modulators used in this project utilize the linear electrooptic effect as the dominant mechanism for

achieving phase modulation of the optical waveguide modes. The actual modulator characteristics and performance depend on the composition, dimensions, and doping of the various layers. Thus, the final device design is the result of balancing acceptable insertion loss and operating voltages to achieve a device which operates at desired wavelengths.

The fabrication of the modulator chosen for this research (see Figure 2-13) is fully compatible with the processing requirements for the dielectric-loaded strip waveguides discussed earlier. Before etching the waveguide ridge, the device regions which are designated to become modulators, are p^+ doped by subjecting them to a selective Be implant, and a rapid thermal annealing process. Following the waveguide ridge etch, p -type contacts are deposited on the modulator waveguide ridges, and a common n -type contact is made by metalizing the bottom of the sample. It is to be pointed out that due to limitations in the growth of the epilayers, it is not possible to achieve a true p^+i-n^+ , but the actual modulator structure is a $p^+-n^-n^+$ heterojunction device. However, the effort should be made to keep the n^- -layer as intrinsic as possible. The performance of both, modulators and the waveguides, are a function of the layer thickness, composition, and carrier concentration, as well as the dimensions of the waveguide ridge.

The waveguide modulators were analyzed by using the effective index method (EIM). However, instead of using a four-layer analysis for the structure in the x -direction, a five-layer slab guide approach was chosen to account for the index changes in the cladding layers due to different carrier concentrations. The eigenvalue equation for the modes of a five-layer slab waveguide structure is derived in Appendix A. In this analysis it is assumed that the electric field generated by the reverse biased heterojunction device is fully confined to the center (ridge) region. All possible fringing effects into the side regions were neglected. Thus, the center region was treated as a five-layer slab waveguide with the p^+ -layer as the top cladding. The effect of the applied voltage on the effective index of the center region can be modelled using a perturbation approach, or a more exact series solution approach [17]. This makes it possible to calculate the effective index of the center region $N_r(V_a)$, as a function of the applied modulator voltage V_a . Thus, by combining the effective index of the center region $N_r(V_a)$, and the unperturbed effective index of the side regions N_s , the overall propagation constant $\beta(V_a)$ can be calculated using the symmetric three-layer waveguide analysis discussed in Section 2.1.2. The net change in the phase of the propagating mode due to an applied voltage is then given by

$$\Delta\phi = \beta(V_a) - \beta(0) \quad (2.64)$$

where $\beta(0)$ is the propagation constant of the waveguide mode without applied voltage.

2.3.1 Linear Electrooptic Effect in Zinc Blende $\bar{4}3m$ Crystals

The GaAs-AlGaAs compounds used in this research are crystals of the zinc blende $\bar{4}3m$ symmetry class. This section will describe the change in optical properties of such crystals under the influence of an external electric field-electrooptic effect.

The linear electrooptic effect is the change in the index of refraction caused by and is proportional to an applied electric field. In general, the direction dependent index of refraction of a lossless material can be described by its impermeability and the changes thereof as follows

$$\kappa = \kappa_{ij} + \Delta\kappa_{ij}(\mathbf{E}) = \begin{bmatrix} 1/n_x^2 & 0 & 0 \\ 0 & 1/n_y^2 & 0 \\ 0 & 0 & 1/n_z^2 \end{bmatrix} + \begin{bmatrix} \Delta\kappa_1 & \Delta\kappa_6 & \Delta\kappa_5 \\ \Delta\kappa_6 & \Delta\kappa_2 & \Delta\kappa_4 \\ \Delta\kappa_5 & \Delta\kappa_4 & \Delta\kappa_3 \end{bmatrix} \quad (2.65)$$

When referring to phase modulators, κ denotes the impermeability tensor of a material (not the coupling coefficient). The linear change in the coefficients $\Delta\kappa$ due to an arbitrary field $\mathbf{E}(E_x, E_y, E_z)$ is defined by

$$\begin{bmatrix} \Delta\kappa_1 \\ \Delta\kappa_2 \\ \Delta\kappa_3 \\ \Delta\kappa_4 \\ \Delta\kappa_5 \\ \Delta\kappa_6 \end{bmatrix} = \begin{bmatrix} \Delta(1/n^2)_1 \\ \Delta(1/n^2)_2 \\ \Delta(1/n^2)_3 \\ \Delta(1/n^2)_4 \\ \Delta(1/n^2)_5 \\ \Delta(1/n^2)_6 \end{bmatrix} = \begin{bmatrix} r_{11} & r_{12} & r_{13} \\ r_{21} & r_{22} & r_{32} \\ r_{31} & r_{32} & r_{33} \\ \textcircled{r_{41}} & r_{42} & r_{34} \\ r_{51} & \textcircled{r_{52}} & r_{35} \\ r_{61} & r_{62} & \textcircled{r_{36}} \end{bmatrix} \begin{bmatrix} E_x \\ E_y \\ E_z \end{bmatrix} \quad (2.66)$$

The 6×3 matrix with elements r_{ij} is called the electrooptic tensor. The form of the tensor can be derived from crystal symmetry considerations, which dictate which of the 18 tensor coefficients are zero, as well as the relationship that exists between the remaining coefficients [34]. In crystals of the zinc blende $\bar{4}3m$ symmetry class there are only three nonzero elements $r_{41}=r_{52}=r_{36} \neq 0$ (see the circled elements in Equation (2.66)). The coordinate system x', y', z' , is determined by the

crystallographic axis and is, in general, not identical to the coordinate system shown in Figure 2-13.

One approach to analyzing the linear electrooptic effect is by applying the *index ellipsoid* method. In general, the effect of an external electric field on a crystal can be mathematically formulated as follows

$$(\epsilon_0 \kappa_{ij} + r_{ij} E_k) x_i x_j = 1 \quad (2.67)$$

However, in GaAs-AlGaAs, when no external electric field is applied, the indices along all directions are the same, $n_x = n_y = n_z$. Thus, if the modulator shown in Figure 2-13 is subjected to an external electric field applied only along the x' -direction Equation (2.67) simplifies to

$$\frac{x'^2}{n_0} + \frac{y'^2}{n_0} + \frac{z'^2}{n_0} + 2r_{41} E_{x'} y' z' = 1 \quad (2.68)$$

The above y' - z' coordinates can be rotated to lie along the principal axes of the ellipse such that

$$z = \frac{z' + y'}{\sqrt{2}}, y = \frac{z' - y'}{\sqrt{2}} \quad (2.69)$$

where the z is the [100] direction and, y is the $[1\bar{1}0]$ crystallographic direction. The x' and x are identical and are oriented along the [110] direction. Thus using the device coordinates (see Figure 2-13) Equation (2.68) can be rewritten as

$$\frac{x^2}{n_0} + \left(\frac{1}{n_0^2} + r_{41} E_x \right) y^2 + \left(\frac{1}{n_0^2} - r_{41} E_x \right) z^2 = 1 \quad (2.70)$$

The new indices along the principal device axes are given by

$$\frac{1}{n_y} = \frac{1}{n_0} + r_{41} E_x$$

$$\frac{1}{n_z} = \frac{1}{n_0} - r_{41} E_x$$

However, for most practical applications, $|r_{41} E_x| \ll 1$ such that

$$n_y \cong n_0 + \frac{1}{2} n_0^3 r_{41} E_x \quad (2.71)$$

$$n_z \cong n_0 - \frac{1}{2} n_0^3 r_{41} E_x \quad (2.72)$$

For the GaAs-AlGaAs device structure shown in Figure 2-13, when a reverse-bias ($E_z < 0$) voltage is applied, there is no linear electrooptic effect for TM

modes. However, for TE modes the index of refraction decreases along the [110] crystallographic direction

$$\Delta n_z(E_x) = -\frac{1}{2}n_0^3 r_{41} |E_x| \quad (2.73)$$

and along the $[1\bar{1}0]$ direction it increases with an applied field as

$$\Delta n_y(E_x) = +\frac{1}{2}n_0^3 r_{41} |E_x| \quad (2.74)$$

Thus, for a device oriented according to Equation (2.70) and Figure 2-13, in which the propagating mode is predominantly TE, it can be expected that the index of refraction increases with an applied reverse-bias voltage.

2.3.2 Phase Modulator Refractive Index Profile

The step-index profile for the unperturbed five-layer waveguide modulator structure, $n_0(x)$, is shown in Figure 2-14. The layer 1 of the rib is p^+ -type doped whereas layer 5 is n^+ -type. Layers 2, 3, and 4 are lightly n -type and are, as discussed earlier, nominally undoped to minimize free-carrier absorption losses. When a reverse bias voltage is applied across the p - n junction, the effects of an increasing applied electric field on the refractive index profile is treated according to four cases, each corresponding to successive depletion and punch-through of layers 2, 3, and 4 [17]. Since the individual layers are assumed to have constant carrier concentrations, the electric field within will vary linearly with depth. Thus if the linear electrooptic effect is the dominant index changing mechanism, the refractive index profile will also have a linear depth dependence.

The refractive index profile for the case where all layers are depleted is shown in Figure 2-15. The change in refractive index due to the depletion of free-carriers is given by

$$dn_i = \frac{N_i q^2 \lambda^2}{8\pi^2 \epsilon_0 (n_i - dn_i) c^2 m^*} \quad (2.75)$$

where λ is the wavelength, m^* is the effective mass of the carrier, and N_i is the carrier concentration in region i . The linear electrooptic change in the refractive index at the layer interfaces is given by

$$\Delta n_i = +\frac{1}{2}n_i^3 r_{41} |E_i| \quad (2.76)$$

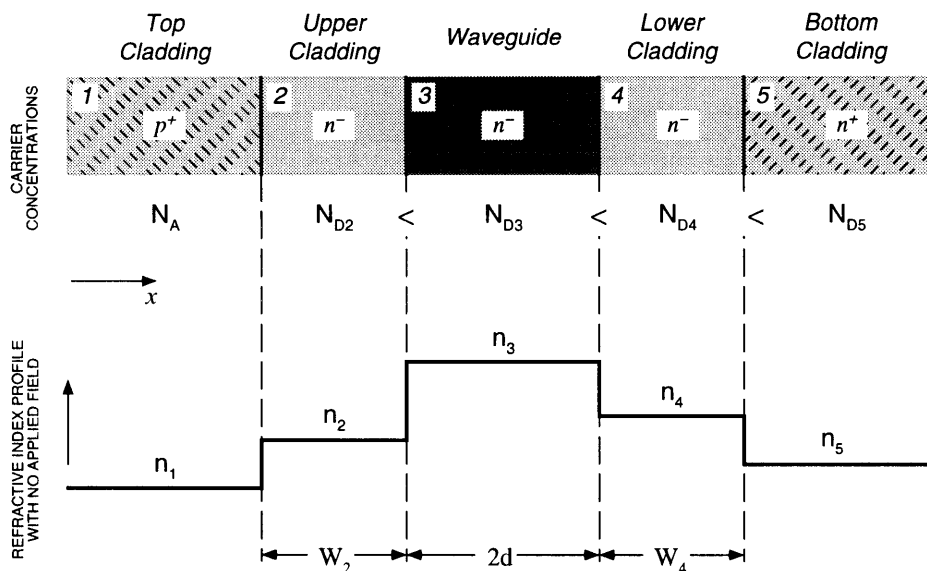


Figure 2-14: Step-index profile of the five-layer waveguide modulator structure without applied bias voltage.

where n_i is the index in the upper region (including the effect of free-carriers), and E_i is the electric field at the interface.

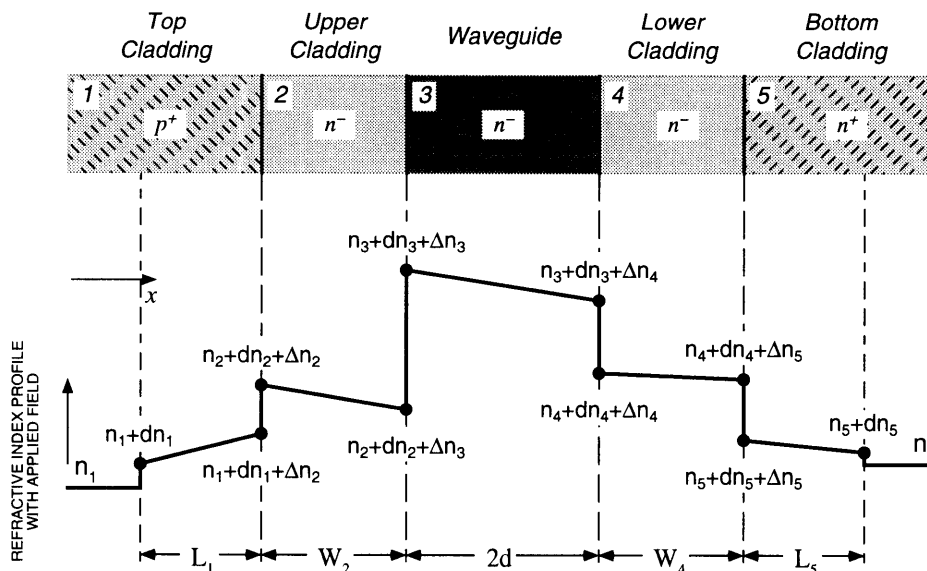


Figure 2-15: Phase modulator refractive index profile for the general case when the applied voltage is sufficiently high to deplete all layers.

The voltage dependent index profile shown in Figure 2-15 is used for calculating the voltage dependent effective index of the center five-layer

modulator region. The modulator performance was modeled by Suzanne Lau [17] using two different analysis methods. The perturbation approach uses first order perturbation theory to account for the electric field dependent index change. This approach works well for linear index changes $n(x)$ and small $\Delta n(x)$, however, its evaluation becomes prohibitively complex for nonlinear index variations. However, once a structure is analytically analyzed, numerical results can be attained in short computation times. The alternate analysis method is more exact and expands the square of the refractive index $n^2(x)$ in each region as a polynomial function of position x . In the regions where the index of refraction is not constant, the TE polarized electric field is expressed as a polynomial series of position. Since both, the index profile and the electric field are a polynomial series, any desired accuracy can be achieved by including a large enough number of terms when solving the wave equation. This approach to the modulator analysis is general for nonlinear index profiles, and is not limited to small index changes. However, its generality may result in long computation times when used in computer modeling. A more detailed discussion of both methods and their comparison can be found in [17].

2.3.3 Phase Modulator Design

The composition of the epilayers used to fabricate the integrated optical components were chosen for single-mode operation of a waveguide with a width of $\approx 4\mu\text{m}$, and for minimal electroabsorption for applied reverse-biased modulator voltages up to 25V.

The differences in aluminum concentration between the AlGaAs layers, and thus refractive indices, as well as the dimensions of the individual layers were chosen such that single-mode operation was possible. Thus, since the modal behavior of a waveguide is largely a function of the index *difference* between the individual layers, and *not* the actual values, a number of different aluminum concentrations was considered. However, the difference in energy between the bandgap of the material and the operating wavelength, determines the amount of loss due to electroabsorption [32] [33]. Since the aluminum concentration determines the bandgap, it had to be chosen such that the resulting band gap wavelengths were less than the operating wavelength. Moreover, since an applied voltage results in lowering of the effective bandgap of the AlGaAs compounds the operating wavelength should be longer than the wavelength corresponding to the

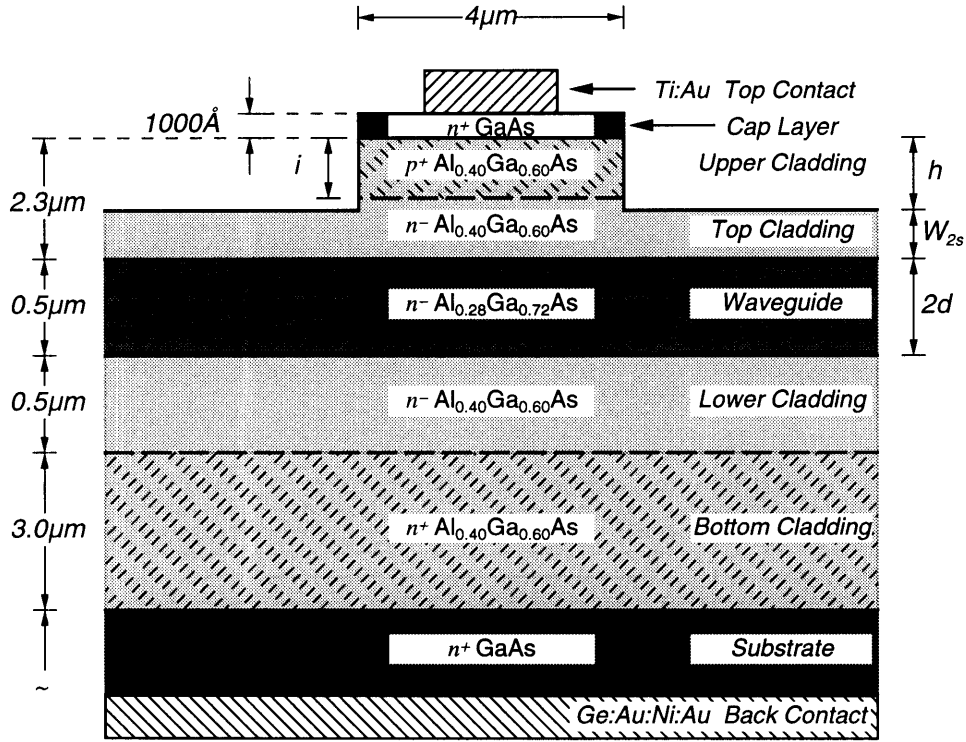


Figure 2-16: Dielectric loaded-strip waveguide phase modulator. The material composition is the same as for the simple waveguide, except that the rib-region is subjected to Be implantation.

bandgap at the maximum bias voltage (25V). Thus, for applied voltages of up to 25V, the band gap lowers about 0.33eV [17]. Table 2-1 shows the bandgap wavelengths of the $\text{Al}_x\text{Ga}_{1-x}\text{As}$ compounds used in this project for no applied bias and a bias of 25V.

Table 2-1: Bandgap wavelength with and without applied bias.

Composition	$\lambda_g(V=0V)$	$\lambda_g(V=25V)$
$\text{Al}_{0.28}\text{Ga}_{0.72}\text{As}$	0.700 μm	0.861 μm
$\text{Al}_{0.40}\text{Ga}_{0.60}\text{As}$	0.646 μm	0.780 μm

To implement the proposed integrated phase modulator it was necessary to form a $p^+n^-n^+$ heterojunction device. Thus, the ridge region was designed to be Be ion implanted up to a depth of about $i=1.8\mu\text{m}$ to form the p^+ region. The lower cladding region was initially n^+ doped using selenium. This process was afterwards turned off, and the remainder of the cladding was grown nominally undoped. However, due to residual doping in the reactor, the actual carrier

concentration profile was in effect graded, decreasing through the lower cladding to the waveguide layer. For applying the desired reverse-bias voltage ohmic contacts were placed onto the p^+ and n^+ regions. The modulator structure designed for this research is shown in Figure 2-16. For device compositions used to fabricate the devices for this research, numerical simulations predict a largely linear relationship between phase modulation and applied modulator reverse-bias voltages [17]. The larger the applied reverse-bias modulator voltage, the larger the phase modulation.

2.4 Integrated Photodetectors

When integrating waveguides and photodetectors onto the same device, the different material-composition requirements for the two have to be combined. The waveguides should have low loss at the wavelength used, whereas the photodetectors should have strong interband absorption for carrier generation. Thus, the choice of the integrated photodetector design was mainly dictated by its compatibility with the performance and fabrication requirements of the waveguides and integrated modulators. Integration of detectors and waveguides can be achieved by a number of techniques (see Figure 2-17). Butt-coupled

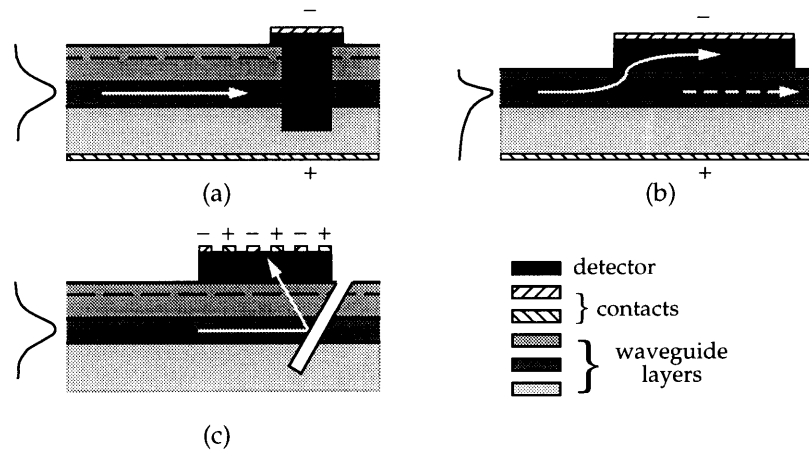


Figure 2-17: Schematics of various integrated detector designs: (a) loaded strip waveguide and butt-coupled detector, (b) rib waveguide with evanescent-coupling detector, (c) loaded strip waveguide and MSM detector with TIR mirror coupling.

detectors [35] [36] are placed as a termination of a waveguide making very efficient coupling possible. Moreover, a small interaction length, and a small area make

them very suitable for high-speed applications. However, their major drawback is that their implementation requires an epitaxial regrowth of the absorbing detector layer. Another implementation of integrated photodetectors is based on the evanescent-coupling approach [37]-[40]. In this implementation, a vertically integrated structure is used, such that part of the power is coupled into a lossy region where detection occurs. This approach, though regrowth free, is incompatible with the use of dielectric-loaded strip waveguides used in this project. The detector implementation chosen for this project is one demonstrated by Bossi *et al.* [41]. This detector is a metal-semiconductor-metal (MSM) detector utilizing total-internal reflection (TIR) to couple light into the absorbing detection layer. This implementation does not require any epitaxial regrowth, and is fully compatible with the dielectric-loaded strip waveguides and modulators discussed previously.

2.4.1 Rectifying Metal-Semiconductor Junctions

Many of the useful properties of a $p-n$ junction can be obtained by making an appropriate metal-semiconductor contact. Thus, the ease of fabrication, in addition to their high-speed performance potential, makes metal-semiconductor junctions of particular interest for integrated photodetector implementations. Such rectifying metal-semiconductor junctions are referred to as *Schottky barrier diodes* [42].

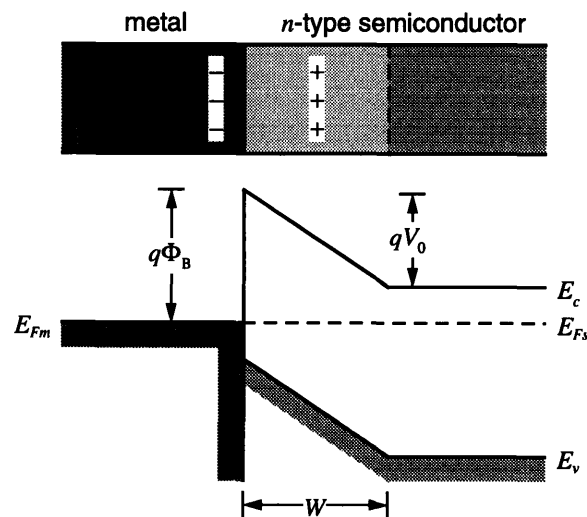


Figure 2-18: A Schottky barrier formed by contacting an n -type semiconductor with a metal having a larger-work function.

When a metal with a work function $q\Phi_m$ is put in contact with a semiconductor having a work function $q\Phi_s$, a charge transfer occurs until the Fermi levels of the materials become equal in equilibrium (see Figure 2-18). For the case where $\Phi_m > \Phi_s$, the Fermi level of the semiconductor is initially higher than in the metal. Thus, to align the two Fermi levels the electron energy of the semiconductor must be lowered with respect to that of the metal. As a result a depletion region, of width W , is formed in the semiconductor near the junction. For a n -type semiconductor, this region will contain positive charges which will be matched by negative charges on the metal. The resulting electric field and the bending of the energy bands within the depletion region are quite similar to the effects found in p - n junctions. The potential barrier Φ_B prevents electron injection from the metal into the semiconductor conduction band. And the equilibrium contact potential V_0 , prevents net electron diffusion from the semiconductor conduction band into the metal, its magnitude is defined as $\Phi_m - \Phi_s$. The potential barrier height V_0 , can be decreased or increased by applying either a forward- or reverse-bias voltage.

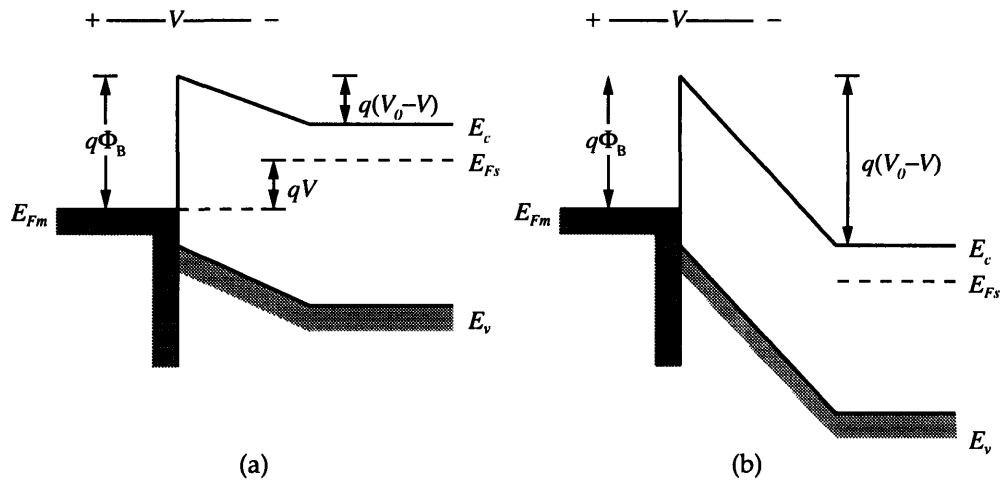


Figure 2-19: Effects of an applied bias voltage on a rectifying metal-semiconductor junction (Figure 2-18): (a) forward-bias ($V > 0$), (b) reverse-bias ($V < 0$).

When a forward-bias voltage is applied to the Schottky barrier in Figure 2-18, the contact potential is reduced from V_0 to $V_0 - V$. As a result, electrons in the conduction band of the semiconductor can diffuse into the metal giving rise to a forward current through the junction. On the other hand, a reverse bias increases the barrier and the electron flow from the semiconductor to the metal becomes negligible. The forward current in each case is due to the injection of *majority* carriers from the semiconductor into the metal. Thus, unlike p - n junctions,

Schottky barrier diodes are essentially majority carrier devices. Although there is an absence of minority carrier injection, the resulting Schottky barrier diode equation is qualitatively similar to the familiar form for a p - n junction:

$$I = I_0 (e^{qV/kT} - 1). \quad (2.77)$$

In actual Schottky barrier diodes the reverse saturation current I_0 can not be established as easily as for p - n junctions. Since the metal-semiconductor junction includes the termination of the semiconductor crystal, and the deposition of a metal film, effects of this material interface can not be neglected. The interface contains *surface states* due to incomplete covalent bonds at the crystal cleave, as well as other effects which can lead to a charge buildup at the interface. Moreover, in practice it is difficult to attain an interface which is perfect on the atomic level. Finally, the interface can be contaminated by an oxide layer affecting the barrier height Φ_b and the current through the junction. Due to surface states, imperfections in the interface layer, and other effects, it is difficult to accurately calculate barrier height values. Therefore, measured, tabulated barrier height values Φ_b are used in actual device design [43].

2.4.2 MSM Photodetector with TIR Coupling

The metal-semiconductor junctions can be used as photodetectors and operate similarly to p - n junction photodetectors. For use as a photodetector the semiconductor material must have an energy bandgap small enough such that light can be absorbed and generate free-carriers. If these carriers are generated in the depletion region (see Figure 2-18), the there present electric field will cause the holes to move to the metal and the electrons to the n -type semiconductor. This tends to make the metal more positive with respect to the n -side, and an open-circuit voltage can be measured between the two diode terminals.

The metal-semiconductor-metal (MSM) detector consists of two, back-to-back Schottky barriers. Two metal contacts are deposited onto a semiconductor (intrinsic) for which the bandgap is smaller than the frequency of the light which will be detected. To be used as a photodetector this device must be operated with an applied bias voltage. When a bias voltage is applied, one of the junctions becomes forward biased, whereas the other, reverse biased junction operates as a photodetector. The field in the depletion region of the reverse biased junction assures the collection of generated carriers. Whereas the forward biased junction allows the photocurrent (and dark current) to flow.

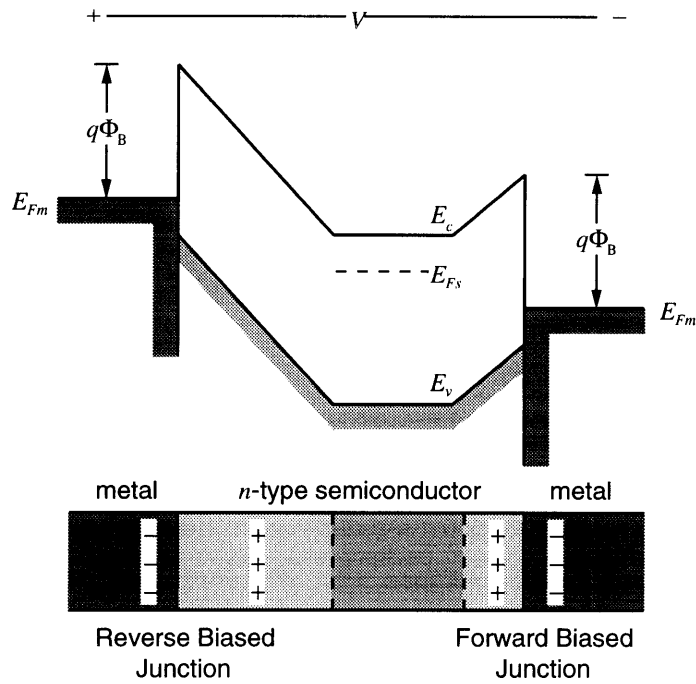


Figure 2-20: Two back-to-back metal-semiconductor junctions with applied bias ($V < 0$). Carriers are generated in the semiconductor region. The depletion region of the reverse biased junction facilitates the carrier collection.

The TIR mirror makes the vertical integration of the dielectric-loaded strip waveguides and detectors possible. The absorbing detection layer is placed above the waveguide and does not compromise the low loss properties of the waveguide (see Figure 2-13). A TIR mirror is etched into the material such that the light is deflected upward, away from the waveguide, into the overlaying detection layer. Interdigitated electrodes are placed on top of the detector mesa. These are used for applying the necessary bias voltage, and measuring the generated photocurrent.

The dielectric-loaded strip waveguide consists of dielectric slabs of different indices of refraction. For efficient coupling into the detection layer the TIR reflection condition has to be satisfied for all layers such that

$$\theta_{TIR} \geq \text{asin} \frac{n_1}{n_i}, n_i = 2 \dots 4 \quad (2.78)$$

When designing this detector system it has to be considered that the reflected light passes through several thin films, and the reflections of the interfaces may reduce the coupling efficiency to the detector. However, for most practical dimensions and refractive indices this does not induce a considerable loss.

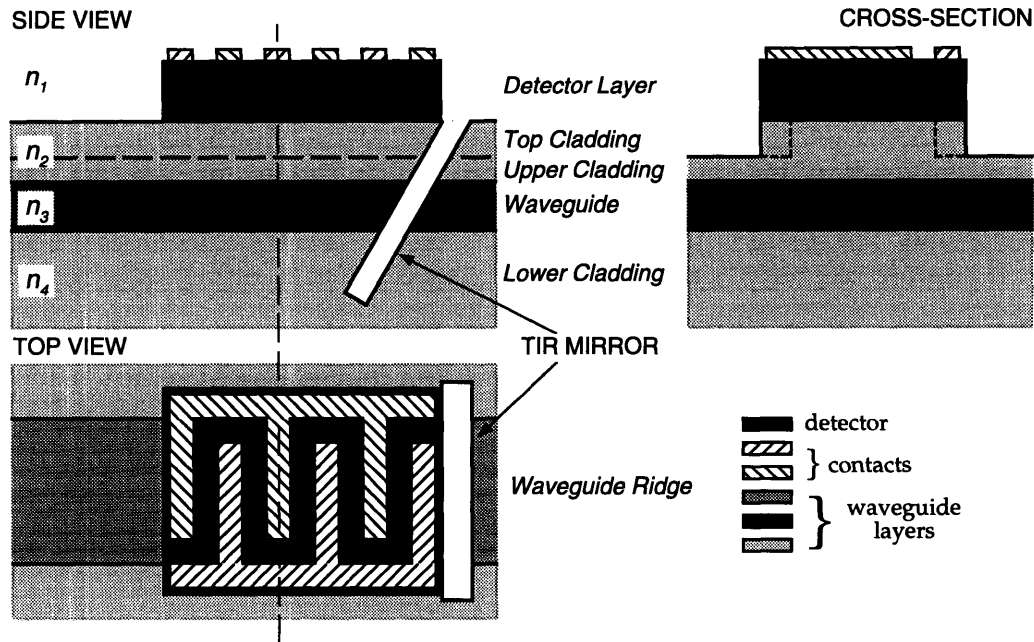


Figure 2-21: Dielectric-loaded strip waveguide and MSM detector with TIR mirror coupling.

The mode confinement is compromised once the mode is in the region under the detector. The lateral confinement is lost once the mode is under the detector, whereas the vertical component remains guided until the mode get reflected form the TIR mirror. Thus, the minimal detector area is determined by considering the mode size within the waveguide, and its dispersion due to unguided propagation.

2.4.3 Detector Design

The MSM detector was designed such that its material needs are fully compatible with other integrated optical components. The epitaxial waveguide/modulator layers are kept unchanged but additional stop-etch and detector layers are grown on top. Thus assures that the optimized waveguide and modulator performance is not compromised by adding a $1.3\mu\text{m}$ GaAs detector layer to the structure. The 500\AA $\text{Al}_{0.60}\text{Ga}_{0.40}\text{As}$ stop-etch layer separating the waveguide and the detector material was needed to assure good fabrication results and has no operational significance.

The detector and stop-etch layer were removed everywhere but in $17\times 69\mu\text{m}$ regions where the detectors were placed. The TIR mirror consisted of a groove etched at an angle greater than the critical angle θ_c . The θ_c was determined by the

index difference between the AlGaAs layers and the TIR mirror material. For the simplest case this would be air, however, it was decided to coat the TIR mirrors with a SiO₂ layer for protection. Since the index difference between AlGaAs and SiO₂ results in a larger θ_c the later was chosen to determine the TIR mirror angle θ . Thus the mirror angle was made to be at $\theta=30^\circ$ with respect to the sample normal. The groove forming the TIR mirror was about 6 μ m deep and 10 \times 13 μ m in area.

The interdigitated Ti/Au detector contacts were 2 μ m wide fingers with 2 μ m spacing between them. These fingers were connected to contact pads used for applying a desired bias voltage and for measuring the generated photocurrent.

3 Fabrication of the Integrated Optical Phase Difference Measurement and Correction System

3.1 Device Fabrication

The optical phase difference measurement and correction device presented in this work was fabricated from an epitaxial layer structure as shown in Figure 3-1. The epilayers were grown by organometallic vapor phase epitaxy (OMVPE) in a vertical rotating-disk reactor [44].

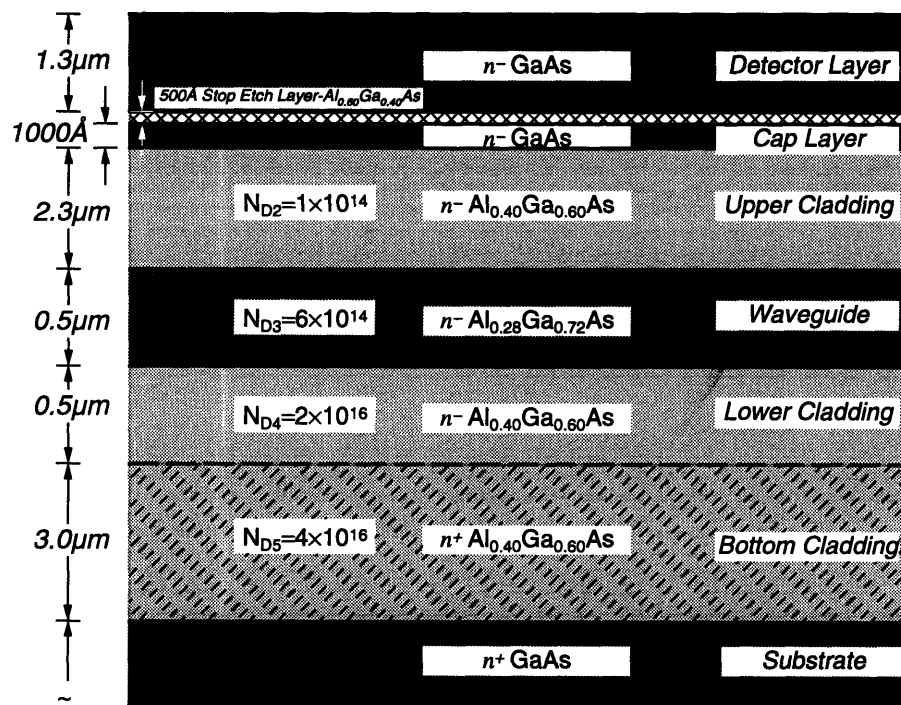


Figure 3-1: Epitaxial layers for fabrication of the Integrated Optical Phase Measurement and Correction System are grown by OMVPE.

The vertical rotating-disk reactor consists of vertical quartz tube and a RF-heated rotating molybdenum susceptor. The process gases are introduced through a stainless steel mesh to ensure uniform gas flow into the reactor tube. The source materials were trimethylgallium (TMG), trimethylaluminum (TMA), 100% arsine (AsH_3), and selenium (H_2Se). Purified hydrogen was the carrier gas, and the reactor pressure was maintained at 0.2 atm. or less. The substrate used for epitaxial

growth was a 2 inch, n^+ doped horizontal Bridgeman grown [100] GaAs substrate (purchased from Sumitomo), tilted 2° towards the nearest [110] plane. Prior to the epitaxial growth the substrates were degreased in organic solvents and etched for 30 seconds in H_2SO_4 , followed by a 60 seconds etch in $H_2SO_4:H_2O_2:H_2O$ (5:1:1) mixture at room temperature.

The completed epitaxial layer wafer (2 inches in diameter) is cleaved up into four rectangular pieces of approximately 17×12 mm in size. These pieces can be used for fabricating the proposed device, whereas the remaining pieces are used for processing and fabrication tests.

3.1.1 Photodetector Definition

For implementing the proposed MSM photodetector design it was necessary to remove the top GaAs layer in all parts of the sample but the regions designated to be used as photodetectors. This processing step required two etching steps to reach, and stop, at the stop etch layer. Moreover, an additional etch step was needed for removing the actual stop etch layer.

The sample was initially cleaned with organic solvents and an appropriate photoresist (PR) mask was deposited to protect the designated detector regions from being etched. The sample was pre-etched using an ion beam assisted chlorine etch (IBAE- Cl_2). However, since the etch rates for this process do not differ significantly for different aluminum considerations, the etching process does not selectively etch GaAs and stop at the $Al_{0.60}Ga_{0.40}As$ layer. Thus, the IBAE was used to etch up to a depth within approximately 2000 \AA of the stop etch layer, whereas a selective wet etch technique was used to etch up to the stop etch layer itself.

The selective etch was a mixture of H_2O_2 and NH_4OH which has different etch rates for GaAs and $Al_{0.60}Ga_{0.40}As$ depending on the pH of the solution. A solution with $pH=7.5$ was chosen because it did not etch $Al_{0.60}Ga_{0.40}As$ measurably, but etched GaAs at about $3000 \text{ \AA}/\text{min}$. Thus, it was possible to assure that all the GaAs was removed without concern that the etch stop layer would be punctured in places where the GaAs may etch more quickly. The sample was etched by immersing it into the etch solution and hand agitating it. Once the etch stop layer was reached, it became, and remained smooth and of one color only. The resulting structure had mesas in places (PR masked regions) and was of uniform level everywhere else. The etch stop layer was removed by submerging the sample for

about 5-10 seconds in HF and rinsing it in DI H₂O. This process etches Al_{0.60}Ga_{0.40}As at about 5000Å/min but etches Al_{0.40}Ga_{0.60}As at a comparably negligible rate.

The selective wet etching could not be used for etching of the whole mesas. It was observed that for samples of the size used in this project, the pH etching technique would not yield good results when etching more than 1µm of GaAs. This problem seems to be due to the difficulty of providing enough fresh etch solution to all parts of the sample throughout the etch time. Thus, the sample was pre-etched to remove most of the GaAs using IBAE. An alternate wet etch could have been used, however, since wet etches result in sloped structure side-walls, and an IBAE system was available, the latter method was selected.

3.1.2 Phase Modulator Definition (Be⁺ Implantation)

The first major processing step to fabricating the integrated phase modulators is the selective Be ion implantation, followed by rapid thermal annealing of the designated modulators regions. This process makes it possible to obtain the *p⁺-n⁻-n⁺* structure shown in Figure 2-16 needed for a functioning modulator.

Beryllium is probably the most extensively studied *p*-type dopant for III-V compounds [45] [46]. The diffusion of Be has been found to be very concentration-dependent. A multi-energy Be ion implant based on data published by *Donnelly* [47] was chosen the energies and doses were chosen to give a flat profile with a junction depth in the range 1.8-2.0µm. The implant schedule used for the ion implantation is shown in Table 3-1.

Table 3-1: Be ion implant schedule, at RT, 0° tilt. $N_T=3.9 \times 10^{14} \text{cm}^{-2}$.

Energy [keV]	Dose [cm ⁻²]
400	5/13 N_T
220	4/13 N_T
100	4/13 N_T

The selective implant regions were defined by a thick ($\approx 5\mu\text{m}$) photoresist mask. Following the Be ion implantation, the photoresist was removed by overnight soaking in acetone and O₂ reactive ion etching if needed. The sample was then covered with an anneal cap consisting of a 700Å layer of pyrolytic nitride

(Si₂N₄) deposited. To protect this anneal cap from mechanical damage, an additional, 2000Å layer of poly-silica glass (PSG) was deposited at 300°C. A rapid 900°C thermal anneal was carried out in a flowing N₂ environment for 10 seconds. After the anneal process the PSG and Si₂N₄ layers were removed in a 50:50 HF:H₂O solution.

The Be ion implant profile of a typical sample was obtained by stripping Hall measurements [48] [49]. Hall measurements were taken after repeated removal of thin layers of Be implanted GaAs. Each Hall measurement yields the sheet resistivity ρ_s in Ω/sq , the sheet carrier concentration, N_s in cm⁻², and the sheet mobility, μ_s in cm²/Vs. The measured values for N_s and μ_s at a given etch depth are weighted averages over the actual values of $n(z)$ and $\mu(z)$:

$$N_s = \frac{\left[\int_0^\infty n(z)\mu(z)dz \right]^2}{\int_0^\infty n(z)\mu^2(z)dz} \quad (3.1)$$

$$\mu_s = \frac{\int_0^\infty n(z)\mu^2(z)dz}{\int_0^\infty n(z)\mu(z)dz} \quad (3.2)$$

where z is the depth from the top of the semiconductor. The effective sheet carrier concentration N_s is always less than or equal to the true sheet concentration given by the integral of $n(z)dz$. The equality holds only for the special case when μ is constant through the entire implanted region. The data shown in Figure 3-2 was obtained from a stripping Hall measurement of a Be implanted GaAs, n^- doped sample. The p^+ carrier concentration was calculated using Equation (3.1) to be $\approx 3 \times 10^{18} \text{cm}^{-3}$ and the junction depth is about 1.8 μm .

3.1.3 Waveguide Patterning and Etching

The upper waveguide cladding was etched using an ion beam assisted chlorine etch system (IBAE-Cl₂). The IBAE-Cl₂ was chosen because of its good etch depth uniformity over the whole sample, etch rate reproducibility, and etch depth control to within 500Å. Samples were loaded through a air-lock which minimized etch chamber contamination.

Initially, the samples were cleaned with organic solvents and an 1000Å thick layer of SiO₂ was deposited. The SiO₂ layer was put down using an plasma assisted chemical vapor deposition (PECVD) system which makes it possible to attain extremely uniform dielectric layers. Following the oxide deposition, the

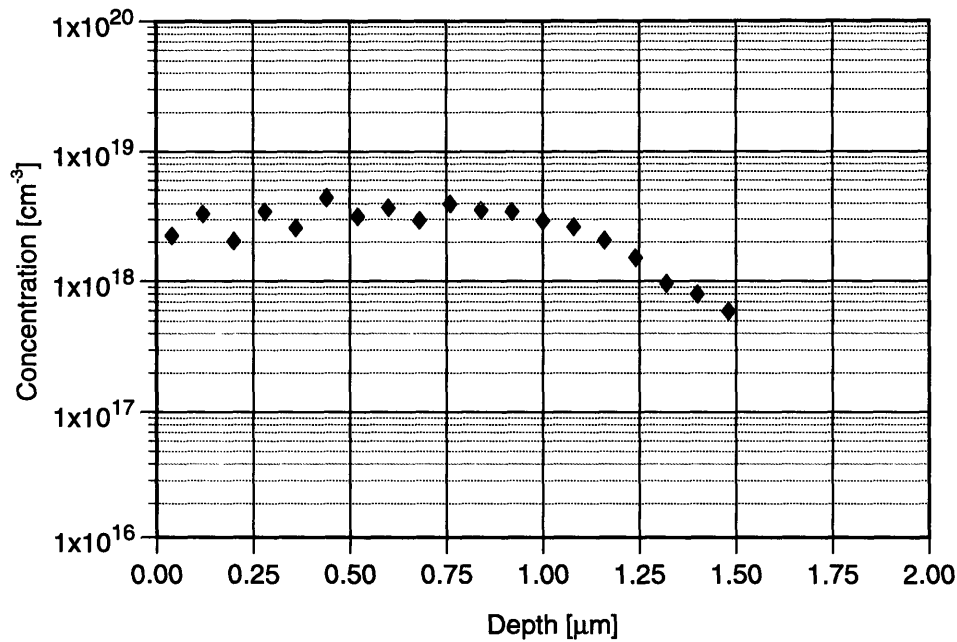


Figure 3-2: Data from stripping Hall measurements of a Be ion implanted, *n*-doped GaAs sample.

SiO₂ layer thickness was measured in several places throughout the sample with an ellipsometer. The oxide was covered with a PR mask, and photolithographically patterned to protect regions which were not to be etched. Afterwards, the samples were put in a parallel plate CF₄-RIE system to etch the SiO₂ layer in places where no PR was present. The resulting structure consisted of a combined PR and SiO₂ mask which was used for the IBAE-Cl₂. The target etch depth (rib height) was determined by the single-mode waveguide design (see Section 2.1.5), and was conservatively chosen to be 1000Å less to account for possible etch rate overshoots.

After the IBAE-Cl₂ was completed, the PR was removed and the rib height determined using a Dektak (this instrument drags a stylus over the surface of the sample and plots the resulting depth profile). The measured etch profile is the sum of the actual etched depth and the thickness of the SiO₂ mask measured earlier. For the cases where the sample was under etched, the remaining SiO₂ mask made it possible to perform additional etches to come closer to the desired target depth. In general, the attained etch depth was within less than 1500Å of the target, and any additional etching was done using a H₂SO₄:H₂O₂:H₂O (1:5:100) mixture at room temperature. This mixture has an etch rate of 70-90Å/sec for Al_{0.40}Ga_{0.60}As and

allows good etch depth control. After the desired results were obtained the SiO₂ mask was removed in buffered hydrofluoric acid (BHF).

3.1.4 TIR Mirror Etch

To couple the light from the waveguide into the detector it is necessary to fabricate a total internal reflection (TIR) mirror. This is achieved by etching a groove at an angle that satisfies the TIR condition (see Section 2.4.3). For etching the TIR mirrors an IBAE-Cl₂ system was used. The sample was mounted at the desired angle with respect to the ion beam (see Figure 3-3) to achieve the desired angle cut.

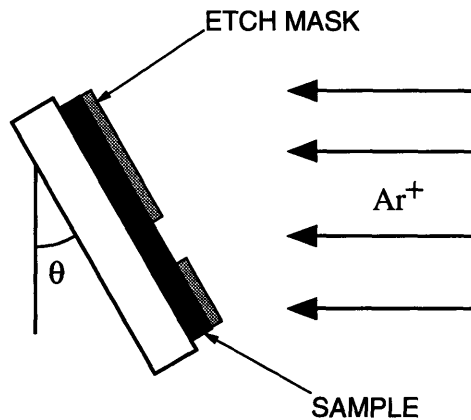


Figure 3-3: Etching of the TIR mirrors using an IBAE-Cl₂ system. The sample is mounted at the desired angle with respect to the ion beam.

A combined SiO₂ and PR mask was used to define the TIR mirror regions. The SiO₂ layer was about 1500Å thick, and the PR was chosen to be 5µm on the average. Such a thick PR was essential to assure coverage of all regions of the sample. At this point in the processing, the sample had detector mesas that were ~3.5µm, and waveguides that were ~2.0µm above the sample level. It was of paramount concern that the PR is thick enough at the tops of these structures and form a sufficient etch mask. Standard photolithography techniques were used to pattern the PR.

In addition to the TIR mirrors, this processing step was also used to etch a groove between the two input waveguides. This 3µm wide groove blocks any light radiating between the two waveguides as a result of radiation loss at the input Y-junction.

3.1.5 Detector and Phase Modulator Contact Deposition

A metal lift-off process was used to deposit contacts to the top of the modulators, and defines the interdigitated MSM detector electrodes. For defining the small features of the detector electrodes it was necessary to use a combined SiO₂ and PR lift-off mask. The PR was patterned such that the phase modulator contacts and detector electrodes were left uncovered. Afterwards, the oxide was etched away in the open areas using BHF. The etch time was chosen to be somewhat longer than needed to remove the SiO₂, such that the resulting undercutting of the PR would facilitate the metal lift-off. A electron beam metal evaporation system was used to deposit 300Å Ti and 1000Å Au. Following the metal deposition the sample was soaked in acetone to facilitate the metal lift-off.

3.1.6 Contact Pad Deposition

The contact pads and the metal strip connecting the to the opto-electronic devices were deposited using metal sputtering. Sputtering was chosen over metal evaporation to assure good side wall coverage of the waveguides and detector mesas. A ~5µm PR mask was used to define the open areas where metallization is desired. A 300Å Ti and 3500Å Au layer were deposited. Afterwards the sample was soaked and sprayed in acetone to remove the excess metal.

3.1.7 Backside Processing

Before starting the processing of the sample backside, a PI2555 polyimide layer was spun on the top surface and soft-baked at 120°C. The polyamide layer serves a protective layer to the top side structures during the backside processing. The sample was mounted top side down on a polishing jig with locwax (heated to 100°C and cooled afterwards). The substrate was lapped to a thickness ≈120µm and then polished using Clorox™ to ≈110µm. After removing the sample from the polishing jig using hot trichloroethylene, the polyimide was removed in AZ606 (7:1) developer. A 300Å Ge : 600Å Au : 300Å Ni : 2000Å Au contact was deposited on the sample backside and microalloyed at 400°C for 30 seconds.

The final processing was to scribe and cleave the sample to obtain mirror-smooth facets. The finished sample was attached on a metal mount using conductive silver paint.

3.2 Photolithographic Mask Set

The photolithographic mask set designed for fabricating the integrated optical phase measuring and correction system consisted of seven individual masks. The masks required for the photolithographic patterning are associated with the following processing steps:

1. Reference alignment marks
2. Detector definition
3. Selective Be ion implantation
4. Waveguide rib etching
5. TIR mirror etching
6. Detector and phase modulator contact deposition
7. Contact pad deposition

In processes with multiple photolithographic steps it is essential to include alignment marks for lining up subsequent patterning steps to preexisting structures on a sample. For this purpose the first mask is used to etch reference alignment marks into the surface of the sample prior to any actual device component fabrication.

A “box and cross” alignment mark system, shown in Figure 3-4 was used in this research. In this alignment system crosses with $2\mu\text{m}$ features are etched onto the sample before any actual device fabrication is performed. Subsequent processing steps have masks with $3\mu\text{m}$ box patterns which have to be aligned with a corresponding cross pattern. In general a particular cross pattern corresponds to a specific processing step. However, if a processing step is non-destructive to an alignment mark, (e.g. Be ion implantation) the corresponding cross pattern may be reused later.

The particular reference mark sets used in this research are shown in Figure 3-5. In addition to the alignment marks needed for each of the photolithographic steps, an additional reference box pattern was etched onto the sample to make mask orientation easier. The alignment mark sets were placed roughly every 2.5mm throughout the mask. By using all the alignment marks on a sample, mask were aligned to within a fraction of a micron over the sample as a whole (17×12mm).

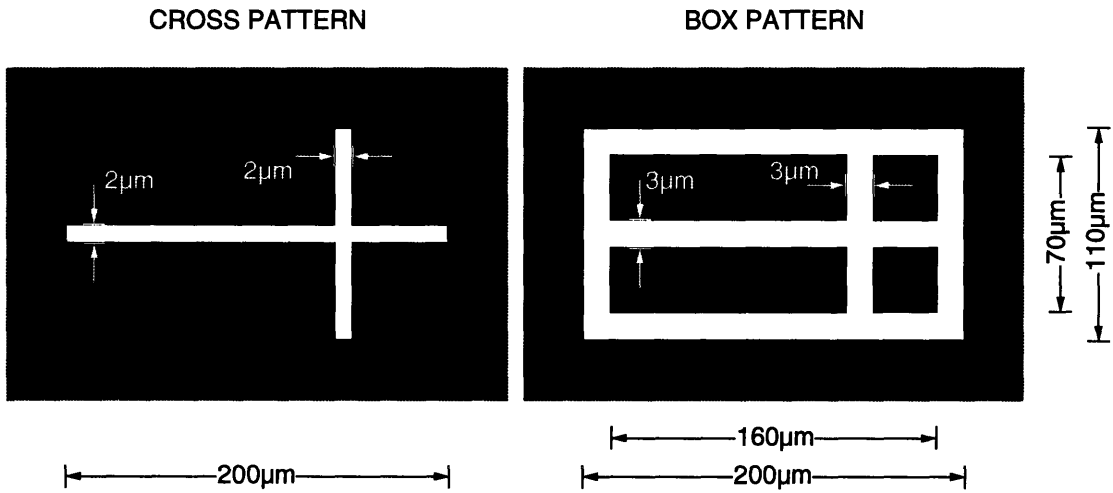


Figure 3-4: "Box and cross" alignment mark system.

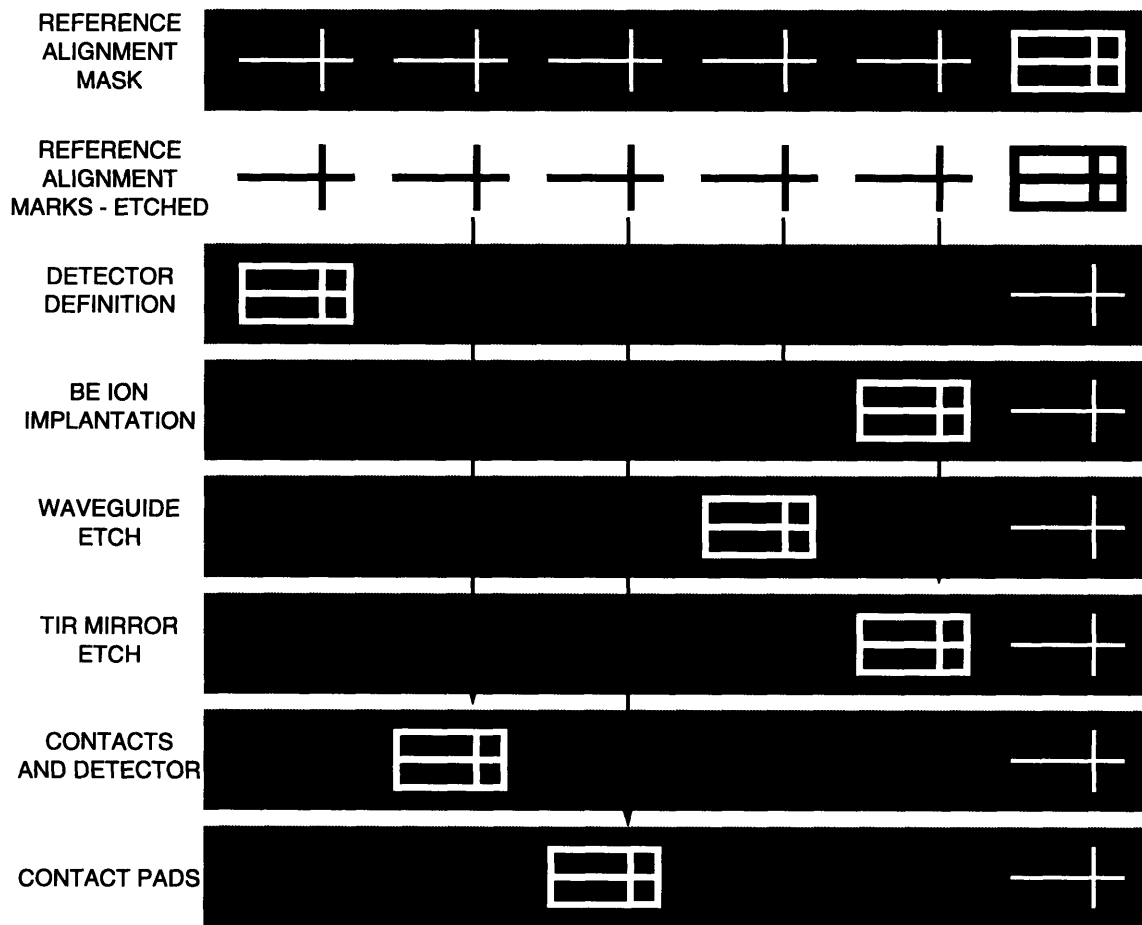


Figure 3-5: Alignment marks for each photolithographic patterning step. The etched crosses are used for aligning subsequent mask.

3.3 Fabricated Optical Phase Measurement and Correction Device

The optical phase measurement and correction device was implemented to demonstrate the feasibility of making a device which can measure and control the output phase between two waveguides. A waveguide coupler is used to tap-off a small portion of the power (less than 10% per guide) for measuring the phase between the two guides. The signals from the two waveguides are combined in a waveguide Y-junction where an interference signal is generated. This interference signal is recorded with an integrated MSM detector. The detected signal is used for establishing the phase relation between two waveguides. Necessary phase corrections can be performed via the integrated phase modulators incorporated in the pass-through waveguides.

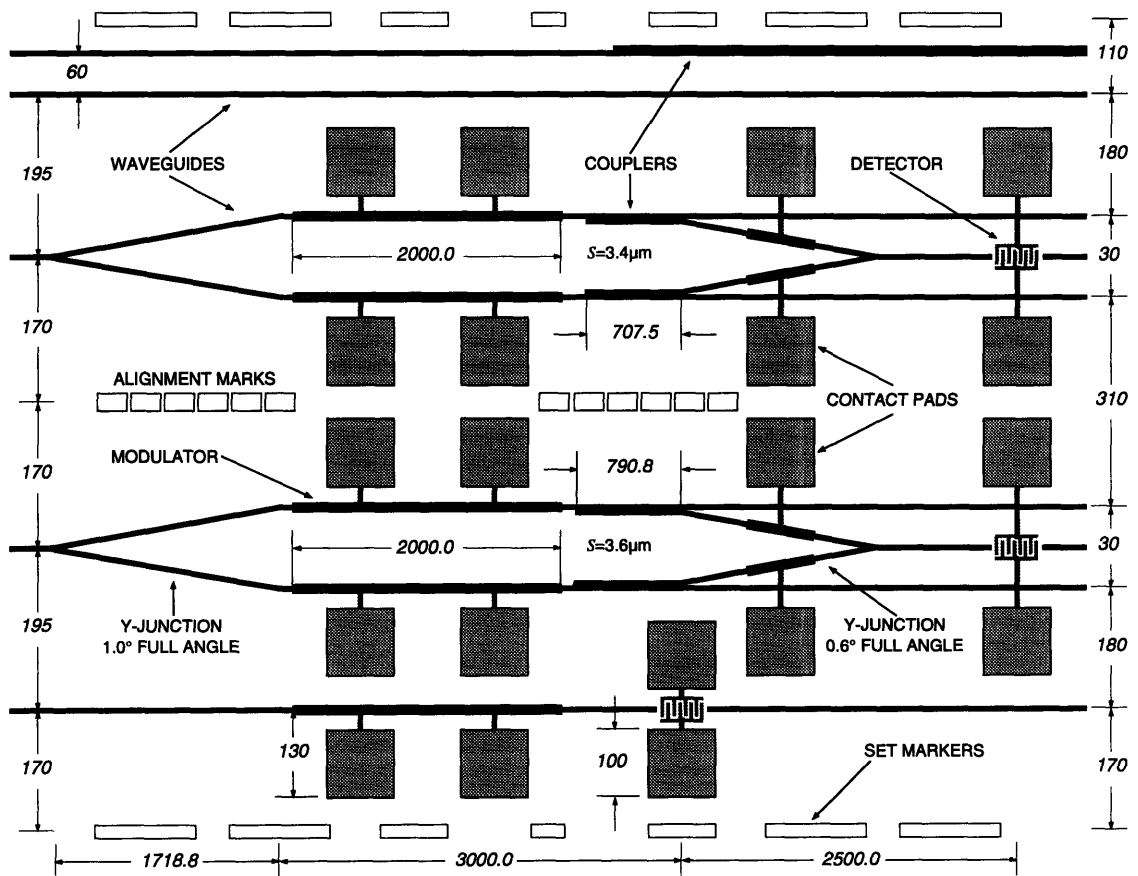


Figure 3-6: A set of devices as they are laid out on an actual sample. All dimensions are in microns [μm].

As discussed, the fabrication of the full device required seven photolithography steps. Each sample was fabricated with ten sets like the one schematically shown in Figure 3-6. Within each set there were two interferometric devices differing only by slightly different coupler parameters. In addition, a straight waveguide, a waveguide coupler, and a straight waveguide with a 2mm modulator and detector were included for testing purposes. The individual sets were separated by a 20 μm wide broken line. A shorter segment was placed at the input Y-junction for easier left/right placement.

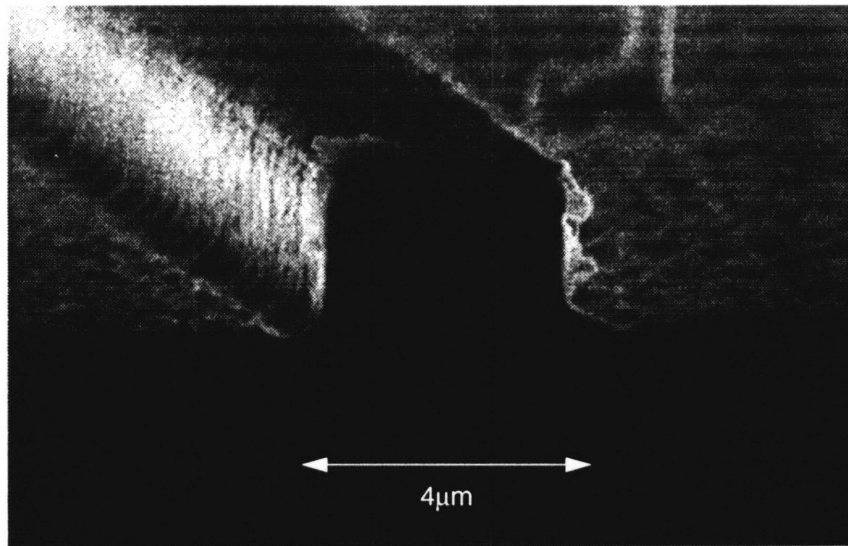


Figure 3-7: Scanning electron microscope (SEM) perspective view of a typical fabricated waveguide.

Figure 3-8 shows the schematics and selected top view microscope photographs of a typical fabricated optical phase measurement and correction device. An 1.0° full angle input Y-junction was used to split the single waveguide input into two parallel waveguides. Each of the waveguides was equipped with a 2.0mm phase modulator with two contact pads connected to each of the modulators. The waveguide couplers were of two different lengths and guide separations, however, both were designed to result in similar power transfers. The signals which were tapped off were combined in a 0.6° full angle Y-junction leading to an integrated MSM detector used for monitoring the interference signal. Each of the branches of the Y-junction were outfitted with an 1.0mm phase modulator to be used for phase dithering. All the opto-electronic components were connected to 100 μm square contact pads which allow for convenient electrical connection using either probe stations or wire bonds.

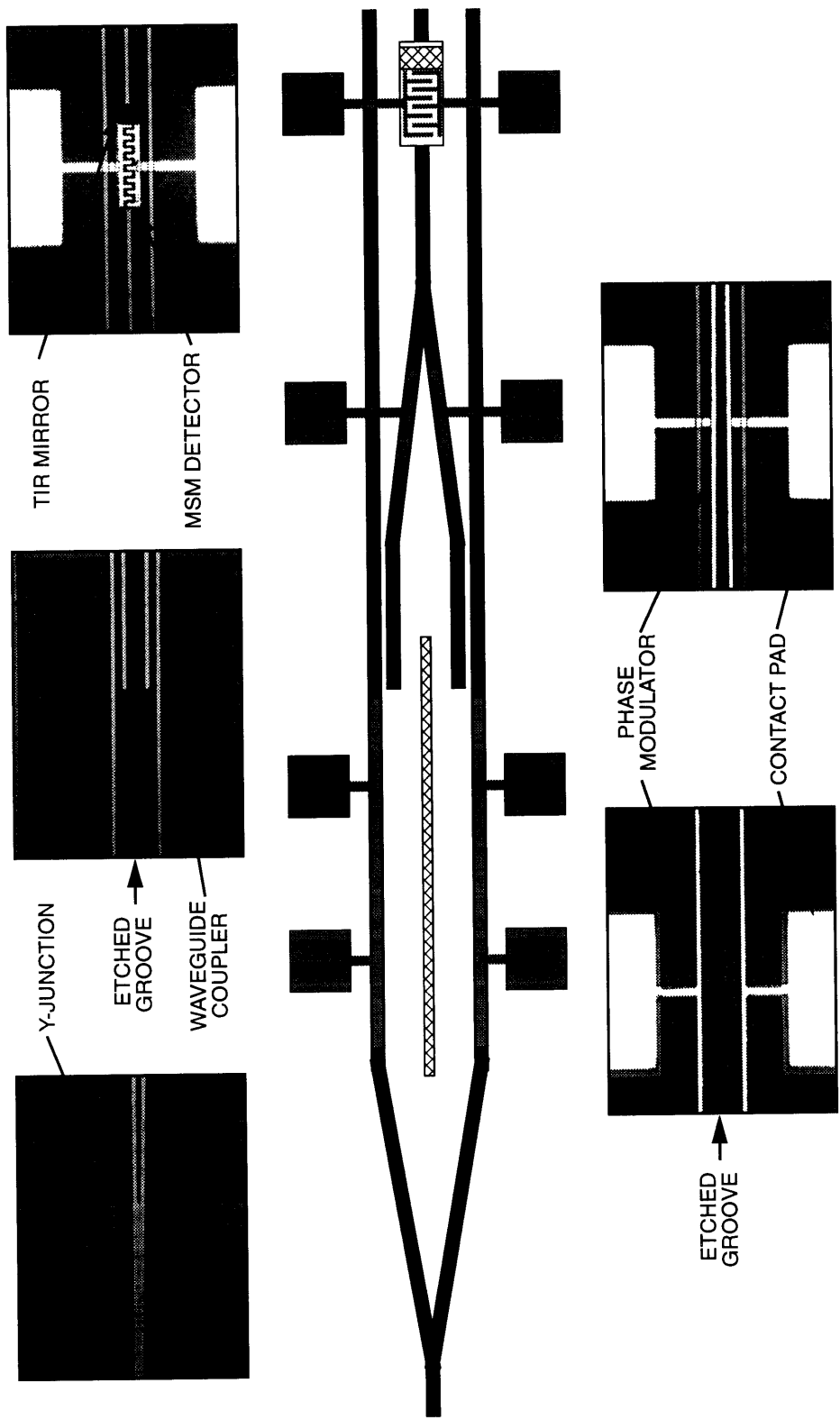


Figure 3-8: Top view microscope photographs of a typical fabricated integrated optical phase measurement and correction device.

4 Integrated Optics and Opto-Electronics Evaluation and Measurement System

4.1 Optical Components

The evaluation system used for this research was specifically designed for evaluating integrated optical and opto-electronic components. The system is equipped for testing of components in a wide wavelength range centered at 0.85 μm . A list of available laser sources and applicable detection apparatus are shown in Table 4-1. Optical components in the setup were uncoated and chosen

Table 4-1: List of available laser sources and corresponding detectors and camera systems used.

Laser Source	Detector Type	Camera Type
HeNe Laser (PMS LSRR-0100) $\lambda=632.8\mu\text{m}$		CCD (Sony XC-37)
Collimated pen lasers (Philips) $\lambda=0.820\mu\text{m}$ $\lambda=0.865\mu\text{m}$ $\lambda=0.880\mu\text{m}$	Germanium or Silicon photodiode	CCD (Sony XC-37)
Single-mode semiconductor laser $\lambda=0.862\mu\text{m}$	Germanium or Silicon photodiode	CCD (Sony XC-37)
HeNe Laser (PMS LSIP-0100-115) $\lambda=1.15\mu\text{m}$	Germanium photodiode	Vidicon (Teltron Model 2200 with TV 2202 tube)

for broadband operation whenever possible. A Newport RS-48-18 optical table with isolation legs XL4A-16 was used as the carrier of the experiment optics.

At the input of the "optical train", the desired laser source can be selected by the means of "flip mirrors". These flip mirrors were originally designed at Lincoln Laboratory and consists of a fixture which allows a 1 inch diameter mirror to be pivoted in and out of the optical path without affecting the optical alignment.

Each of the laser beams is reflected off two mirrors with adjustable horizontal and vertical tilt to facilitate alignment.

The second part of the evaluation optic consists of the optical train. This is the section where the incoming light is inserted into the sample, and the device output collected for detection. The optical path is defined by the centers of two iris diaphragms placed about 30cm apart. All light beams passing through the centers of two diaphragms are colinear, and any necessary realignment of sources is simplified. Since all actual test sources are in the infra-red (IR) part of the spectrum, a red HeNe laser is used as an alignment reference. For wavelengths near $0.85\mu\text{m}$, a disk Polarcor polarizer is used to polarize the input light for TE propagation. At longer wavelengths, a Special Optics polarizing cube was used to polarize the input light. The disk polarizer is preferred because of minimal beam translation.

The light is focused at the device input using a $20\times$ microscope objective. This input objective was mounted on an XYZ translation stage equipped with low voltage piezoelectric translators mounted on the micrometer of each axis. A typical waveguide is $4\mu\text{m}$ wide, with a guiding layer of about $0.5\mu\text{m}$. Under these conditions, the backlash of the micrometer prevents accurate and reproducible light coupling without the piezoelectrics. The piezoelectric translators are continuously adjustable with a travel of $0\text{-}30\mu\text{m}$ by applying a voltage in the range $0\text{-}150\text{V}$. Thus, the piezoelectrics are essential for maximizing and reproducing the input coupling to the waveguides.

The integrated optics samples were mounted onto holders which could be screwed onto a sample stage. The sample stage was designed with many degrees of freedom such that it was possible to optimize the position and alignment of the sample after it is mounted. Thus, the sample is mounted on an XYZ translation stage, a horizontal rotation stage with ultrafine adjustments, and a goniometer head. The rotational stage allows the rotation of the sample in the plane of the optical table, whereas the goniometer head can be adjusted for tilting the sample with respect to the optical table plane. A stereozoom microscope with up to $50\times$ magnification is used for monitoring the sample from above.

The output section of the optical system contains the output imaging optics, cameras for observation, and detectors for power measurements. A trinocular microscope was mounted on a XYZ positioner and equipped with a switching mirror to direct the output to either the camera tube (straight-through) or the eyepiece. When the camera tube output is used, the output is redirected (using

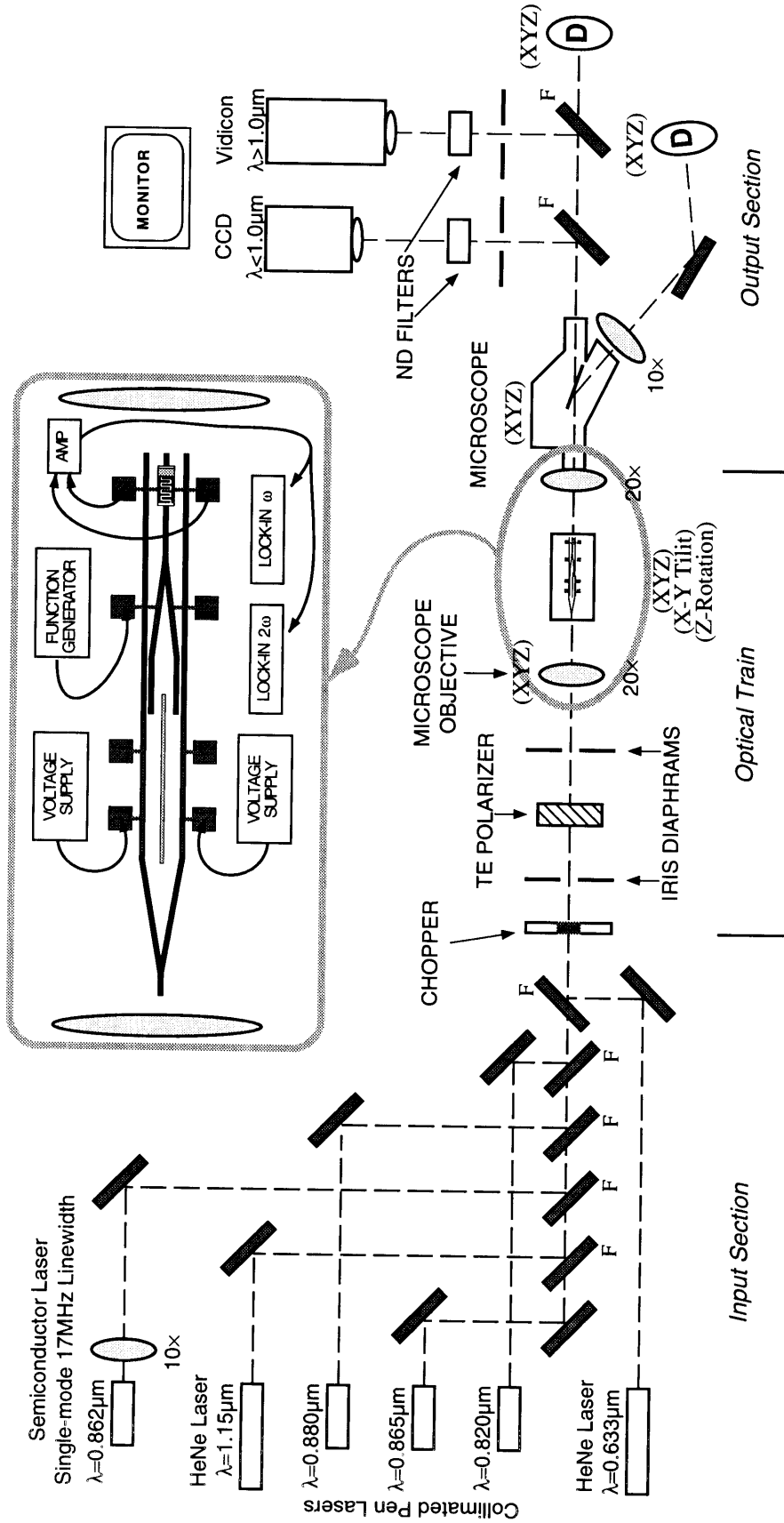


Figure 4-1: Schematic of the experimental set-up used for testing of the optical phase measurement and correction module. The mirrors marked "F" are flip mirrors.

flip-mirrors) either to CCD camera or the vidicon, or the light is passed through to a detector. The integrated optical device output is imaged by a 20× microscope objective at the camera and the detector planes simultaneously. The waveguide output can be switched between the cameras and the detector without realignment and refocusing. The output is focused by illuminating the output facet with white light, which reflects off the mirror cleaved output facet, and the image is focused at the camera (and detector) plane. As a result of the different wavelength, the infrared is slightly out of focus at this position, and can be readily identified and focused when the white light is turned off.

If the output image is directed through the eyepiece output, it is further magnified by a 10× eyepiece. Either a scanning or an ordinary mirror can be used to direct the output to a detector. The scanning mirror is convenient for scanning multiple waveguide outputs over the detector and recording the spatial (y-direction) power distribution. Pinhole apertures in front of the detectors are used for blocking stray light.

4.2 Experimental Set-up for Evaluating Phase Measurement and Correction Devices

The experimental set-up used for evaluating the phase measurement and correction devices is shown schematically in Figure 4-1. The lasers used for evaluating the devices were the Philips collimated pen lasers listed in Table 4-1. The light was TE-polarized and coupled into the input waveguide using a 20× microscope objective. These laser diodes have a coherence length much shorter than the length of the sample so that it was possible to avoid Fabry-Perot resonances. The light at the device output was collected using a 20× microscope objective, and was imaged either onto a CCD camera, or a detector. A flip mirror made easy switching between the two detection systems possible. Moreover, a 200μm pinhole aperture was placed in front of the detector to block out stray light.

Probe stations were built for applying electrical signals to the modulator and detector contact pads. Each probe station consisted of 1.8μm diameter gold wire soldered to the center conductor of a rigid coaxial cable. The coaxial cable was attached, but electrically isolated, to a XYZ translation stage. Electrical signals could be applied (received) using standard coaxial connectors. The translation stages were used to bring the gold wires in contact with the contact pads. A stereozoom microscope was used to monitor the wire as it touched the pad and the

bending of the wire was observed to confirm actual contact. The outer coaxial conductors were connected to a common ground. However, the modulator and detector circuitry were kept electrically isolated to avoid ground loops.

Probes were connected to the MSM detector contact pads to apply a desired bias voltage and collect the generated photocurrent. The detected signal was amplified by a transimpedance amplifier. Lock-in amplifiers were used to measure the amplitudes of the first and second harmonics of the dither frequency. Programmable power supplies were used for setting desired bias voltages to the modulator probes, and a programmable function generator was used to provide the dither signal and the reference to the lock-in amplifiers. The lock-in amplifiers were configured such to measure the first and second harmonic of the reference frequency (dither frequency). An IBM PS/2 Model 80 computer with a IEEE-488 interface card was used to remotely control the test instruments. This made it possible to make the testing fully automated and form an active feedback loop. HP Basic programs were written to collect the lock-in readings and set the desired voltages on the programmable power supplies.

5 Device Characterization Measurements

5.1 Waveguide Phase Difference Measurement

Figure 5-1 shows the experimental setup used for measuring the phase difference between two waveguides. To characterize the integrated modulators and verify the interferometer operation the output was recorded as a function of the reverse-bias voltage applied to one of the 2.0mm modulators. The other 2.0mm modulator was driven by a sinusoidal dither signal with an voltage offset V_{offset} assuring that the modulator remains reverse biased at all times. The data obtained using the phase dither approach confirmed the predicted linear voltage/phase relationship for the fabricated modulators. To demonstrate the interferometer and modulator operation an external photodetector was used for recording the interferometer output signal.

The modulator reverse-bias voltage V_{set} was stepped from 0 to 25V in steps of 0.25V. Measurements of the interferometer output were conducted for several dither amplitudes and offset voltages V_{offset} , always assuring that the modulators were reverse biased at all times. A typical set of data, obtained using a dither amplitude $V_r=2.0V$ is shown in Figure 5-2. The voltage needed for obtaining a π phase-shift was $V_\pi=5.0V$. Equation (5.1) was used to successfully recover the phase difference between the two adjacent pass-through waveguides.

$$\Delta\phi = \arctan \left[\frac{A(\omega) J_2(\Gamma)}{A(2\omega) J_1(\Gamma)} \right] = \arctan \left[\frac{A(\omega) \left(\frac{\Gamma^2}{8} - \frac{\Gamma^4}{96} + \dots \right)}{A(2\omega) \left(\frac{\Gamma}{2} - \frac{\Gamma^3}{16} + \dots \right)} \right] \quad (5.1)$$

The Bessel functions in Equation (5.1) were calculated using the first two terms and the simple linear relationship for the amplitude of the phase dither $\Gamma=\pi V_r/V_\pi$ (see Section 1.2.1). The range of phase angles was chosen such that it always falls in the range between $-\pi$ and $+\pi$. This particular phase range is arbitrary since the phase could have been represented by any 2π interval. The breakdown voltages for the modulators were in excess of 40V.

Using the setup in Figure 5-1 the phase between two adjacent waveguides was successfully recovered. An external Germanium detector was used for detecting the interferometer output signal. A 200 μ m pinhole was placed in front of the detector to block-out stray light from hitting the detector. The first and

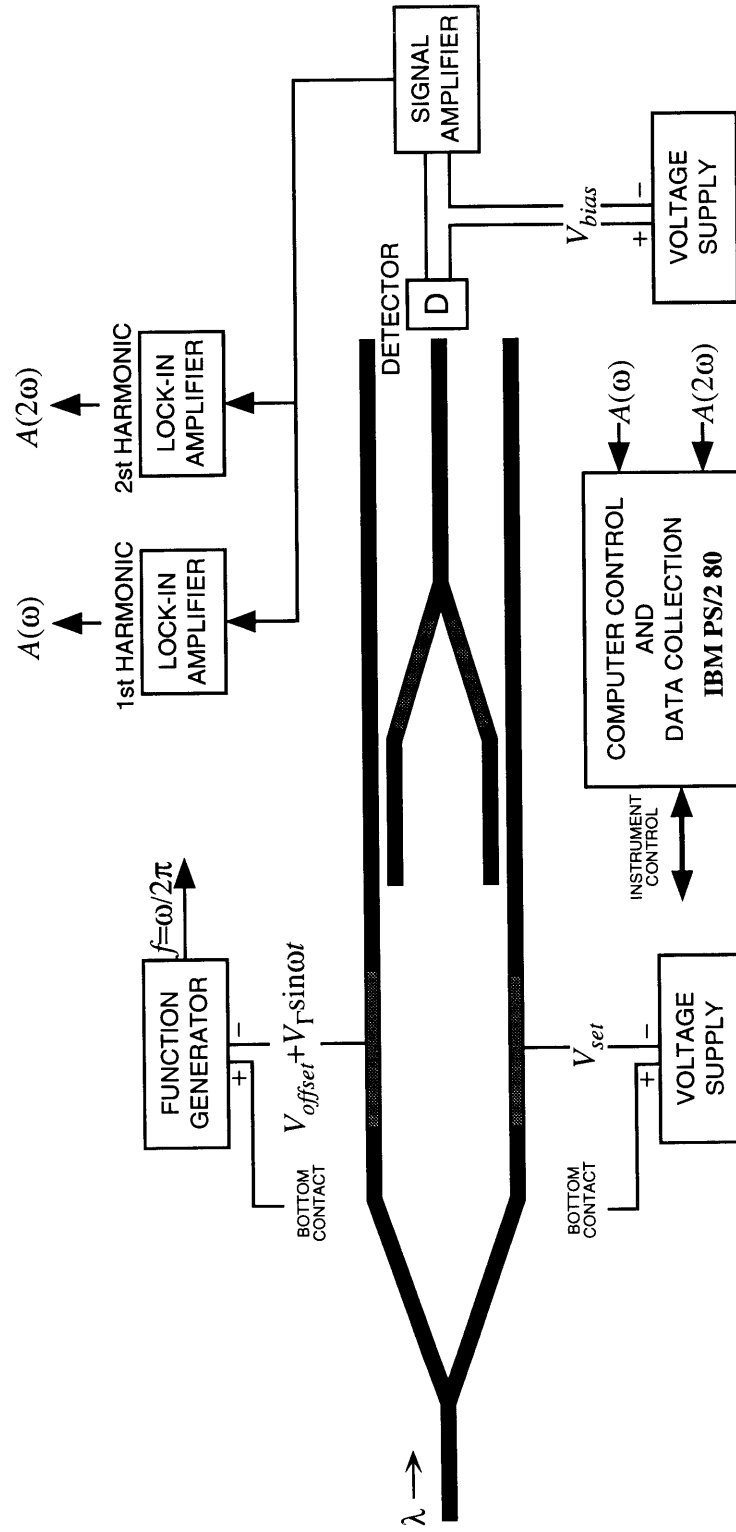


Figure 5-1: Characterization of the modulator and interferometer performance. The phase difference between the waveguides can be measured using the integrated interferometer. The phase can be set by applying a voltage to the integrated phase modulators.

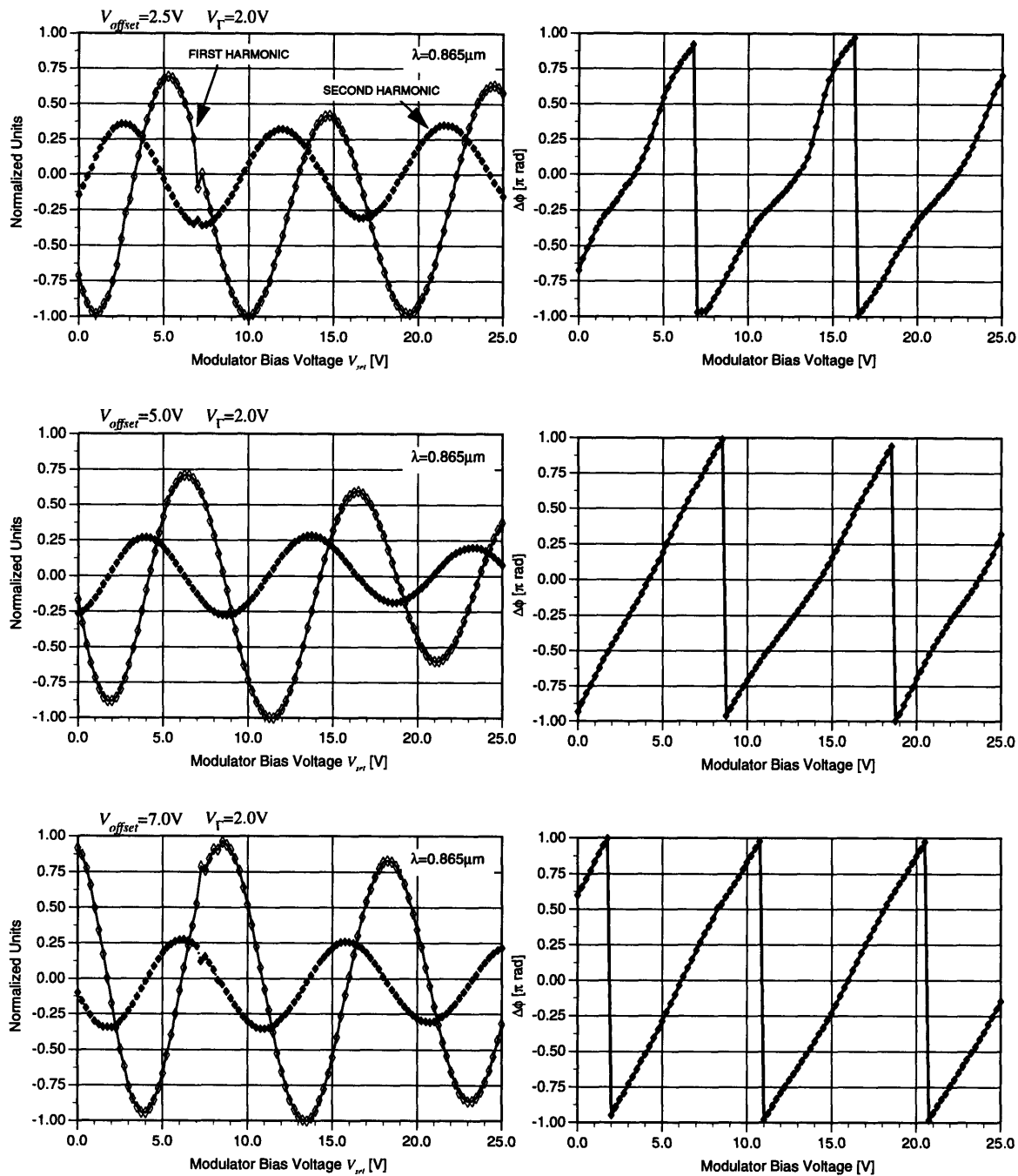


Figure 5-2: Typical interferometer outputs obtained using the setup shown in Figure 5-1. On the left are measured amplitudes for the first and second harmonic of the detector signal. The corresponding calculated phase differences between the two waveguides are shown on the right.

second dither harmonic were separated with lock-in amplifiers and the amplitudes were sent to the computer where the phase was calculated using Equation (5.1).

The nonlinearity in the recovered phase for $V_{offset}=2.5V$ is not due to a fundamental device limitation. To reduce the need for additional processing steps, the top modulator contact was not an ohmic contact. Since this contact was deposited in the same fabrication step as the detector electrodes, Schottky barrier modulator contacts were obtained. To punch-through the Schottky barrier and the modulator layers [17], dither bias voltages of $V_{offset} \geq 5.0$ were used for obtaining the desired phase information.

To measure the coupling coefficient the power in the pass-through waveguides and the signal at the interferometer output were measured. Using Equation (1.2) the power splitting for the couplers was calculated to be $P_2/P_{in} \approx 0.02$. The upper cladding thickness in this portion of the device was measured to be $0.23\mu m$, thus, the experimentally obtained coupling coefficient is in close agreement with the theoretically calculated values shown in Figure 2-12. The waveguide outputs were imaged on a CCD camera to determine the mode profile. The fabricated waveguides were $4.0\mu m$ wide and, as predicted by the theoretical modeling, the waveguide outputs were single-mode.

5.2 Integrated Photodetector Operation

The sample used for testing the photodetector operation was fabricated with all other optical components functioning but was cleaved in such way that the input Y-junction was removed. This allowed for injecting light into only one of the pass-through waveguides and measure the signal coupled into only one branch of the Y-junction (see Figure 5-4) without interference effects. In addition, measurements were conducted on test structures consisting of a straight waveguide with a detector terminating the guide and detecting the injected light.

The integrated photodetector with TIR mirror coupling was tested in two configurations. In the first configuration, the detector was operated as a Schottky barrier photodetector. Both sets of the Interdigitated electrodes on top of the detector mesa were connected together to form a single top contact. The bottom contact on the back-side of the sample was used as the other detector contact. When a reverse-bias voltage is applied to this structure the device is operated as a vertical metal-semiconductor junction photodetector. Alternately, the structure

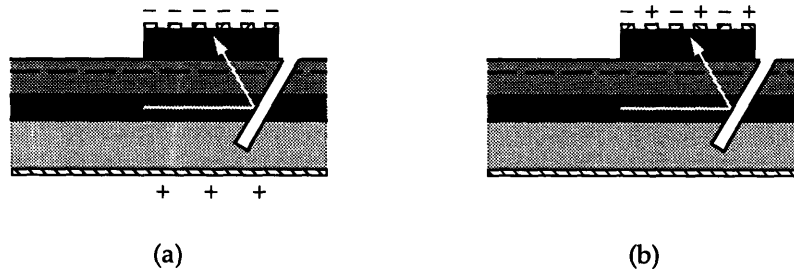


Figure 5-3: (a) Detector operated in Schottky barrier configuration. Both top electrodes are used as a single negative, and the bottom electrode as the positive contact. (b) When operated in the MSM detector configuration, both detector contacts are made to the top electrodes.

was operated as an MSM photodetector. In this configuration a bias voltage is applied across the two electrodes and the photocurrent is amplified and measured.

To demonstrate the operation of the integrated detector the setup in Figure 5-4(a) was used. The detector photocurrent was recorded as function of detector bias voltage. The photocurrent response of the Schottky photodiode is shown in Figure 5-5. When operated in this configuration the device had breakdown voltages in excess of 40V. The photocurrent response of the MSM photodetector operation is shown in Figure 5-6. This detector configuration had breakdown voltage was $V_{breakdown} \approx 15V$. This lower breakdown voltage is attributed to surface breakdown effects between the two interdigitated detector electrodes (see Figure 3-8).

The detector operation was also tested by using the set-up schematically shown in Figure 5-4(b). The data obtained using the vertical Schottky barrier configuration are shown in Figure 5-7, whereas the data for the MSM configuration are shown in Figure 5-8.

Figure 5-9 shows the MSM detector response as a function of optical beam attenuation. The detector was biased with $V_{bias} = 9.0V$. Different neutral density (ND) filters were placed at the input of the test waveguide shown in Figure 5-4(a). The photocurrent was recorded for a number of attenuation factors ranging from 10^0 to 10^{-4} . The results shown are normalized to the signal without any ND filters at the input. The data confirm the expected linear relationship between the optical power and the detector photocurrent. Moreover, the ratio between the saturation currents in Figure 5-5 and Figure 5-6, the ratio between the saturation currents in

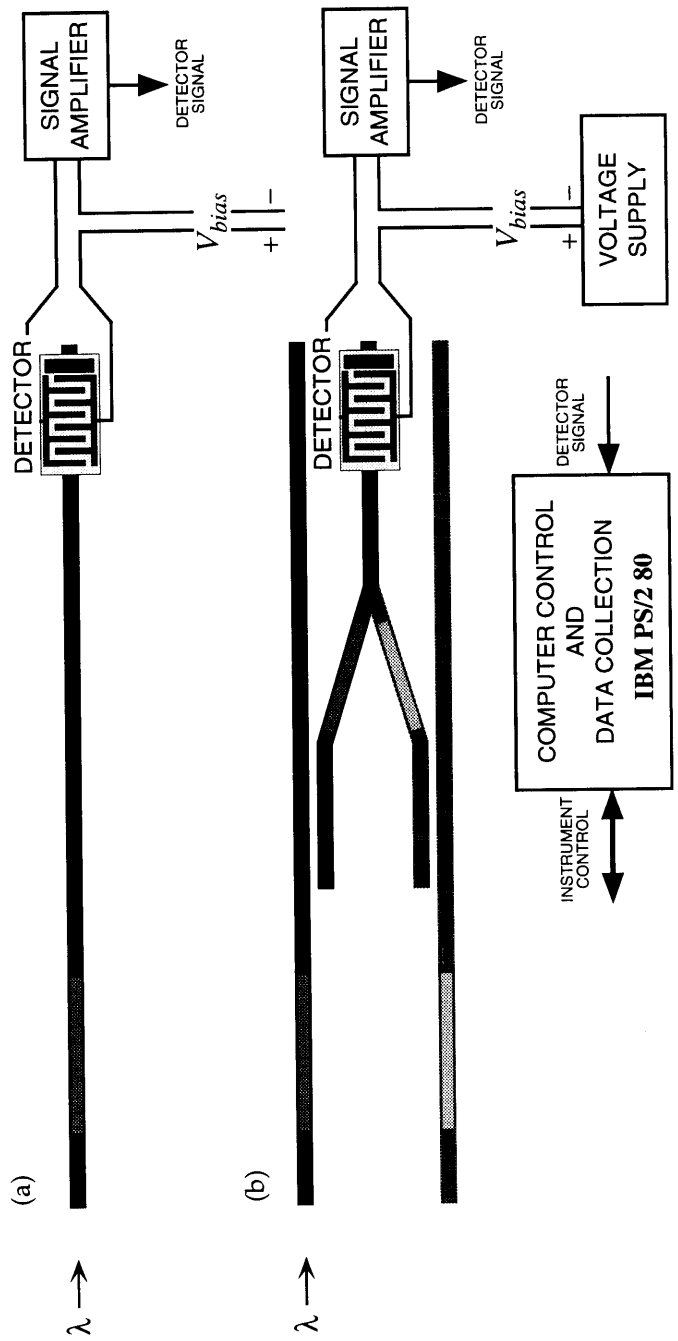


Figure 5-4: (a) Waveguide terminated with an integrated detector. (b) Part of the power in the pass-through waveguide is coupled into the Y-junction and detected with the integrated detector.

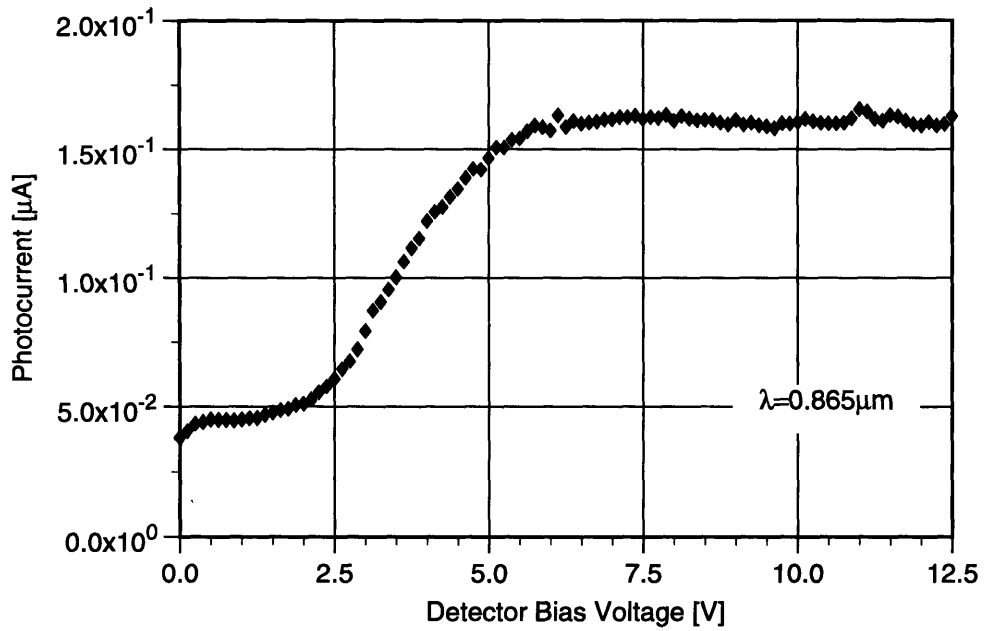


Figure 5-5: Photocurrent measurement of the vertical Schottky barrier detector using the set-up shown in Figure 5-4(a).

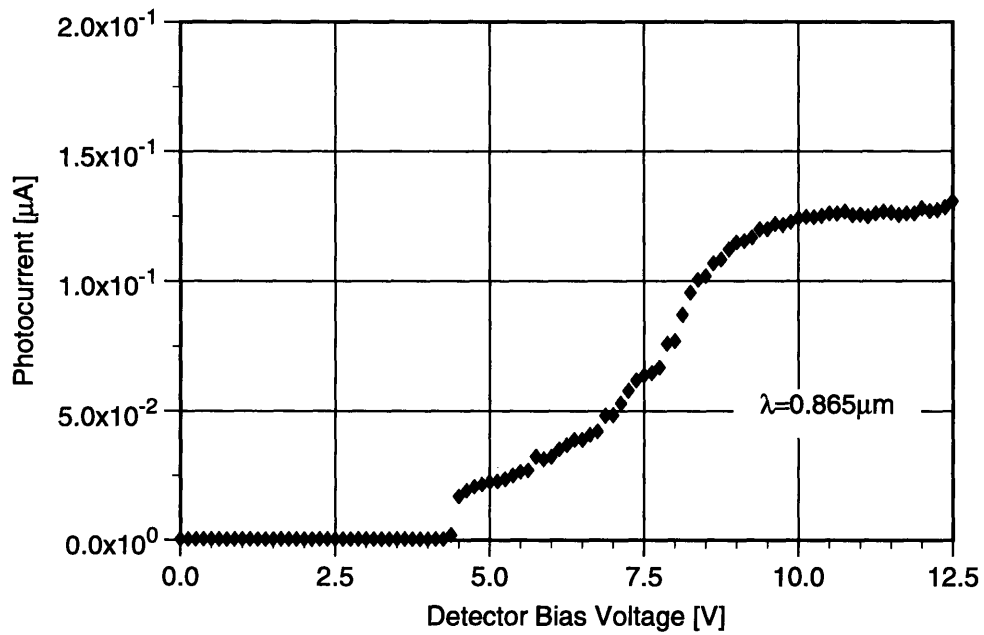


Figure 5-6: Photocurrent measurement of the MSM detector using the set-up shown in Figure 5-4(a).

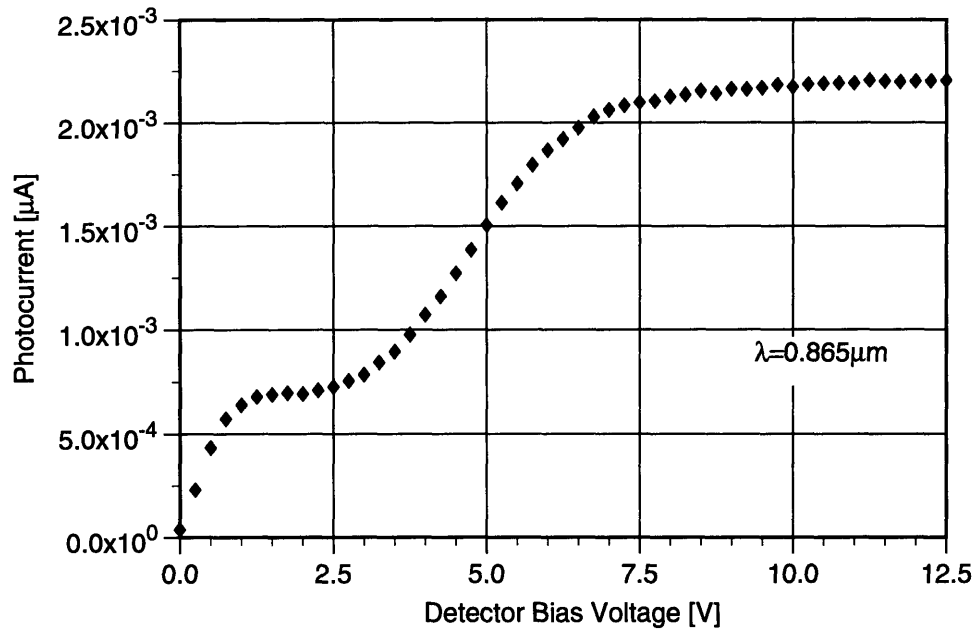


Figure 5-7: Photocurrent measurement of the vertical Schottky barrier detector using the set-up shown in Figure 5-4(b).

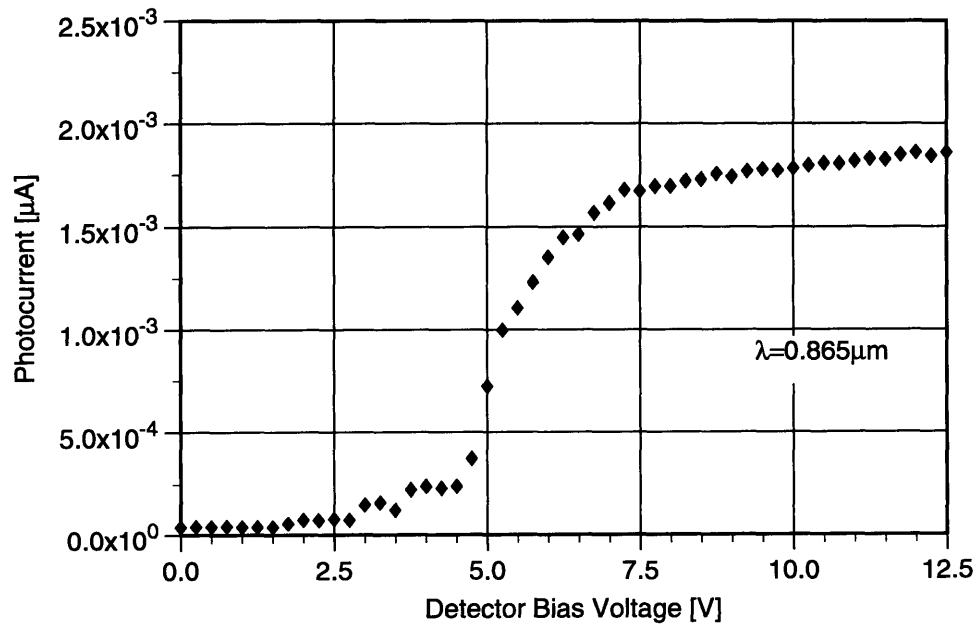


Figure 5-8: Photocurrent measurement of the MSM detector using the set-up shown in Figure 5-4(b).

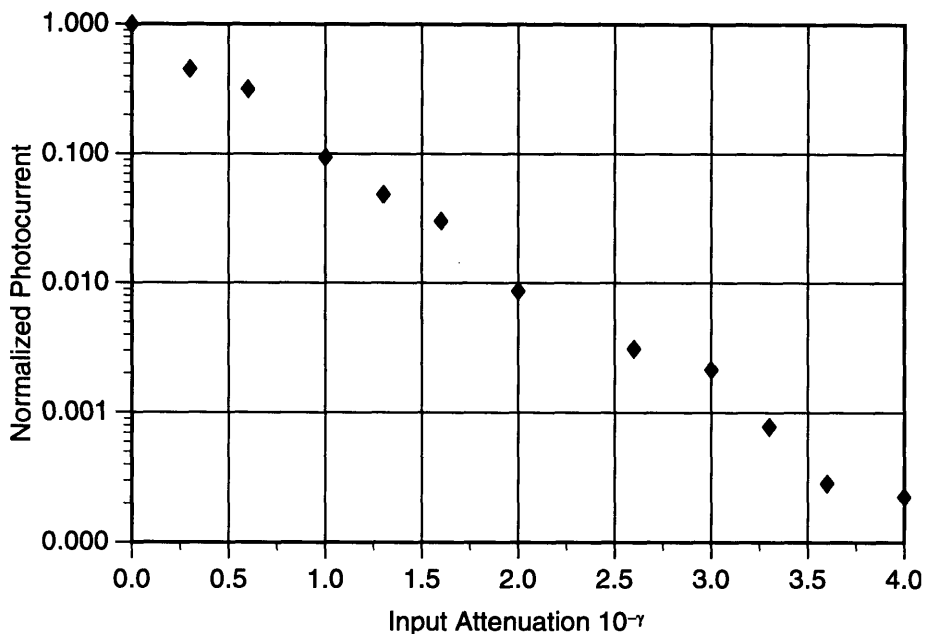


Figure 5-9: Normalized photocurrent as a function of waveguide power attenuation. ND filters were placed at the waveguide input to change the power in the test waveguide.

Figure 5-7 and Figure 5-8, are consistent with the expected power coupling between to the pass-through waveguide and the Y-junction.

The shape of the Photocurrent vs. Bias Voltage data curves were somewhat different for different MSM detectors. However, the saturation currents were in general very similar. The differences are attributed to the different relative position of the optical beam and the MSM detector electrodes. The beam diameter is estimated to be less than $1.5\mu\text{m}$. Depending on the relative alignment of the TIR mirror and detector electrode masks, the reflected beam position varied for different processing runs. In some instances the light was closer to one of the electrodes. Thus, depending on the polarity and magnitude of the detector bias voltage the carrier collection efficiency was different depending on the specific detector geometry. In general, a bias voltage greater than 9.0V assured operation in the saturation regime for which different detectors had photocurrents in close agreement.

In many application the MSM detector configuration is preferred since it allows for high speed operation. However, the fabrication of the MSM detector becomes increasingly more difficult as the detector size is made smaller. The interdigitated detector electrodes are, due to their small size, and placement on top of small mesas difficult to fabricate. Thus, for applications were high speed

operation is not needed, but small size is desired, the fabrication of detectors with a single top electrode and a contact on the bottom of the sample may be preferred.

5.3 Waveguide Phase Difference Measurement with an Integrated Photodetector

The sample tested in this section was fabricated to demonstrate the phase measurement using an integrated photodetector for recording the interference signal. This device was successfully used to demonstrate the phase measurement with all optic and opto-electronic components needed integrated on the same device. The interferometer output was recorded as the function of the 2.0mm phase modulator (see Figure 5-10) reverse-bias voltage. The other 2.0mm phase modulator was used for dithering the phase difference. The data obtained were in close agreement with the once obtained using the external modulator

The modulator reverse-bias voltage V_{set} was stepped from 0 to 25V in steps of 0.25V. Measurements of the interferometer output were conducted for dither amplitudes and offset voltages $V_{offset}=5.0$ and 7.0V. A typical set of data, obtained using a dither amplitude of 1.0V is shown in Figure 5-11. The voltage needed for obtaining a π phase-shift was $V_{\pi}=4.6$ V. The integrated MSM detector was biased $V_{bias}=9.0$ V, and the detector signal was fed into the lock-in amplifiers. The first and second dither harmonic were sent to the data acquisition computer where the phase difference was calculated. The phase was calculated using Equation (5.1), and the device yielded the predicted linear voltage/phase relationship for the fabricated modulators.

All phase data presented were collected by using one of the 2.0mm modulators for applying the phase dither. The 2.0mm modulators were chosen since changes in the applied bias to the 1.0mm modulators (on the Y-junctions) resulted in changes in the coupling between the modulated Y-junction waveguide and the pass-through waveguide (see Figure 5-12). The bias dependent coupling changed the signature of the first and second harmonic making it difficult to reliably recover the waveguide phase difference information. This coupling does not represent a fundamental device limitation but is a result of the close proximity of all optical components. In the next device generation, etched grooves (similar to the one etched between the pass-through waveguides, see Figure 3-8) will be placed between the pass-through and Y-junction waveguides, as well as between

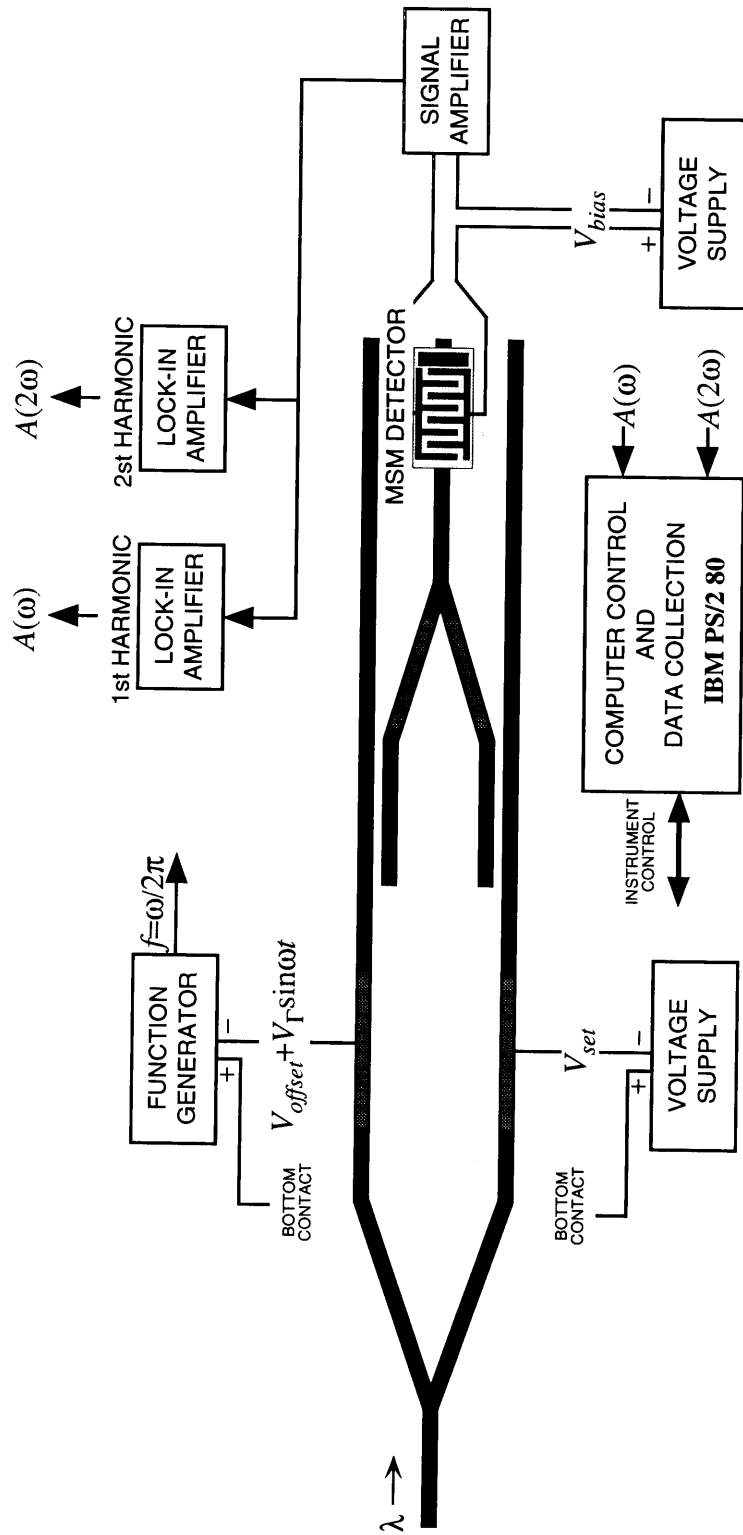


Figure 5-10: Characterization of the waveguide phase difference measurement and correction device. Waveguides, modulator, and integrated detector were fabricated on the same sample.

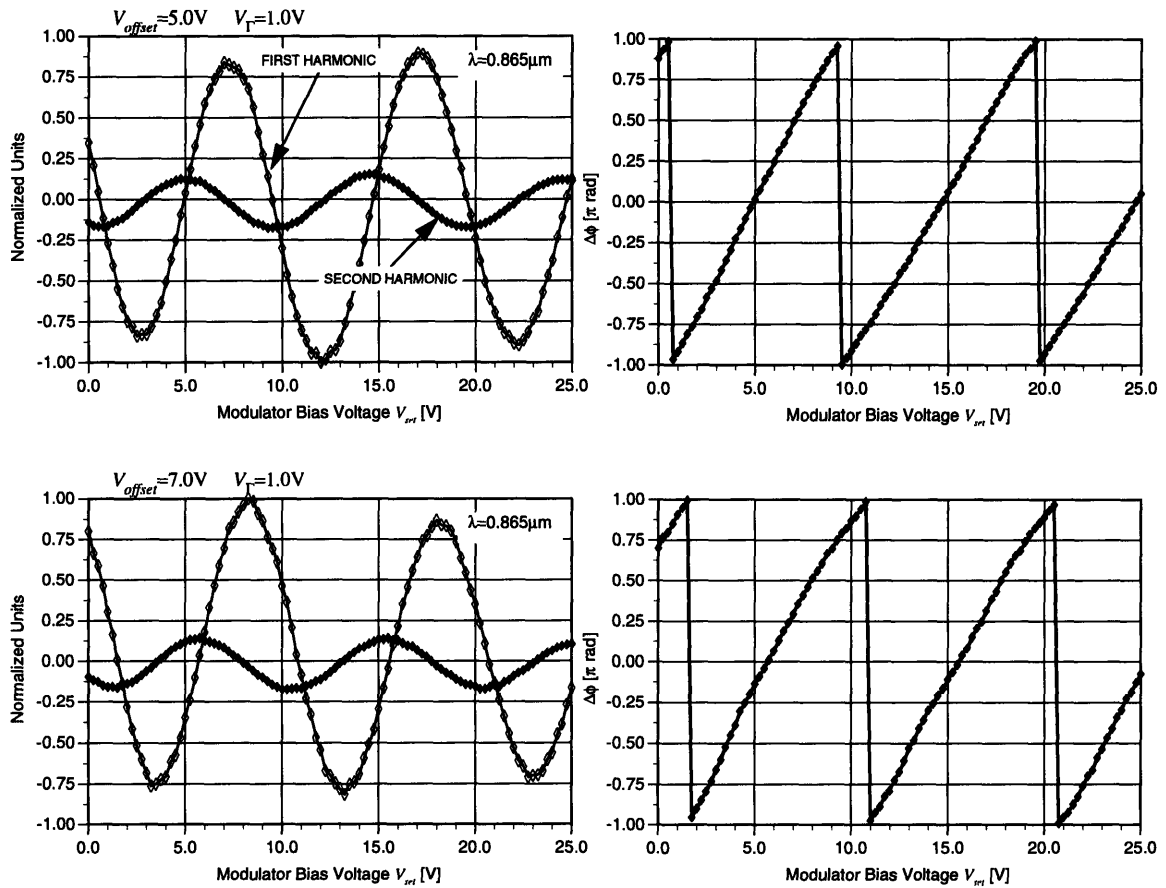


Figure 5-11: Typical interferometer outputs obtained using the setup shown in Figure 5-10. On the left are measured amplitudes for the first and second harmonic of the detector signal. The corresponding calculated phase differences between the two waveguides are shown on the right.

the Y-junction arms. The etched grooves will eliminate the undesired coupling and make it possible to reliably use the Y-junction modulators for phase dithering.

The data in Figure 5-11 show the successful implementation of a device which can measure and control the phase difference between two waveguides by using a small portion of the signal in the pass-through waveguides for phase measurements. All required waveguides (straight guides, bends, junctions, and couplers), modulators, and the photodetector were fabricated on the same GaAs-AlGaAs sample. The integrated photodetector was made small enough ($17 \times 69 \mu m$) to fit between the two test waveguides and was successfully used for phase measurements.

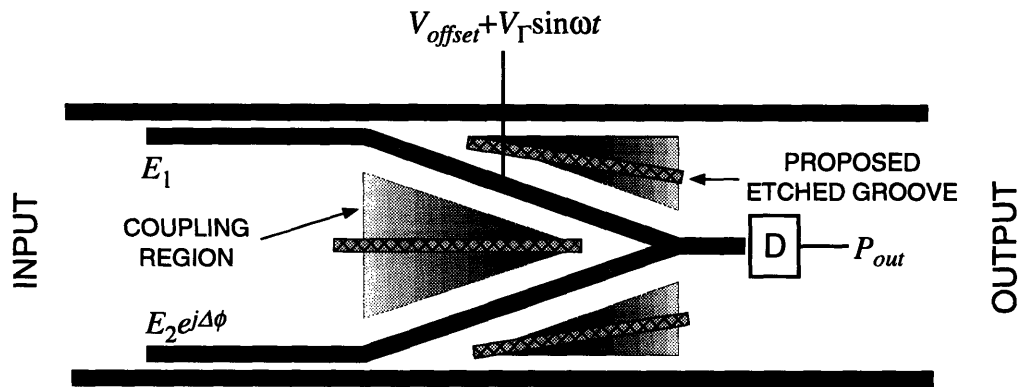


Figure 5-12: Proposed device modification such that the Y-junction phase modulators can be used for applying the phase dither. Grooves are etched to eliminate coupling between adjacent waveguides.

6 Conclusion

6.1 Summary

This thesis demonstrated the operation of a basic module for optical phase measurement and correction between two waveguides. All necessary guided-wave components, modulators, and the integrated photodetector were fabricated on the same substrate.

The theoretical modeling, design, and fabrication of the required AlGaAs guided-wave components was described in detail. The dielectric-loaded strip waveguide design was chosen for this research. All waveguide components were designed for single-mode operation at the wavelength $\lambda=0.865\mu\text{m}$. The input Y-junction was fabricated with a 1.0° full angle, whereas the interferometer Y-junction had a smaller, 0.6° full angle to minimize radiation losses. The phase modulators were fabricated by selective Be ion implantation followed by rapid thermal annealing such that a $p^+n^-n^+$ structure was formed. The phase was modulated by applying a reverse-bias voltage to the junction and inducing a linear electrooptic effect. An integrated metal-semiconductor-metal (MSM) detector using TIR mirror coupling was fabricated for measuring the phase between the two waveguides. The detector design implemented is fully compatible with the low-loss requirements for the guided-wave components used in this device. It allows for the optimization of the waveguide and modulator design without compromising the detector performance.

The devices fabricated for this thesis demonstrated the feasibility of using a small portion of the power in the two pass-through waveguides to measure and control the phase between two waveguides. The device was successfully operated with as little as 2% of the power in the pass-through waveguides being used for the phase measurement. An integrated, on chip, detector was operated with an interferometer to measure the signal containing the phase information. Both, the interferometer and detector were placed between the two waveguides separated by $30\mu\text{m}$. The phase information was recovered, and phase modulators on the pass-through waveguides were used to control the relative phase between the two guides.

6.2 Future Work

This work is a continuation of the work done by Suzanne Lau [17] and is one of the steps to the implementation of an all integrated optical phase front correcting system. *Lau* demonstrated the dynamic phase measurement and correction of the phase difference in the arms of an integrated Mach-Zehnder interferometer. Moreover, it was demonstrated that the phase measurement is independent of the relative power imbalance between the two interferometer arms. This thesis research built on the work done by *Lau* and demonstrated that it is possible to use only a portion of the signal in the pass-through waveguides for the phase measurement. Moreover, by developing an integrated photodetector compatible with other device components it was possible to measure the phase difference without the use of an external detector. This work demonstrated the combined operation of all optical and electro-optic components of the basic phase measurement and correction module.

Future work towards the implementation of an all integrated optical phase front correcting system can be devised into three categories: fabrication and operation of multiple modules in parallel, the optimization of the single module, and development of the integrated control electronics. The fabrication of multiple modules (3-5) would allow for the study of the interdependence of the modules as a part of a larger array. Moreover, such a device would make it possible to study the far-field signature of the multiple module device as a function of the phase difference between the array waveguides. The optimization of the basic module would allow for determining what minimal optical input powers are required for conducting phase measurements. And would identify internal noise sources and device components limiting weak signal operation. This device optimization would also incorporate the etched grooves proposed in Figure 5-12. Finally, future work on incorporating electronics with the integrated optics will benefit from research conducted in related opto-electronic projects. Professor Fonstad's research group at MIT is presently working on the integration of GaAs-AlGaAs lasers and amplifiers with control electronics. The research experiences and results of that effort will be directly applicable to work on the integrated control electronics for the phase front correcting system.

A Five-Layer Slab Waveguide

The analysis of the guided mode in a five-layer slab waveguide structure is similar to the four-layer analysis discussed in Section 2.1.2. A schematic of a five-layer slab waveguide is shown in Figure A-1. The propagation constants are obtained by matching the boundary conditions for E_y and H_z at each layer interface. For the purposes of this research transverse electric (TE) boundary conditions were used in analyzing the five-layer structure.

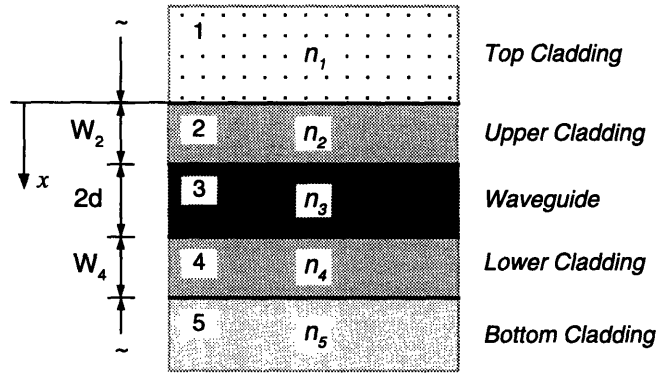


Figure A-1: Five-layer slab waveguide. The structure is uniform in the y - z plane.

As in the case of the four-layer slab waveguide, the TE slab modes for which $\mathbf{E}(\mathbf{r}, t) = E(x, z, t)\hat{y}$, the following relations between the electric and magnetic field can be obtained

$$H_y = E_x = E_z = 0 \quad (\text{A.1})$$

$$H_x = -\frac{\beta}{\omega\mu} E_y \quad (\text{A.2})$$

$$H_z = \frac{j}{\omega\mu} \frac{\partial}{\partial x} E_y \quad (\text{A.3})$$

The electric fields in all the individual regions have to satisfy the wave equation

$$\nabla^2 \mathbf{E}(\mathbf{r}, t) - \mu\omega \frac{\partial^2}{\partial t^2} \mathbf{E}(\mathbf{r}, t) = 0 \quad (\text{A.4})$$

Moreover, the boundary conditions require that E_y and H_z (which is equivalent to $\partial E_y / \partial x$) are continuous across the layer boundaries. Equations (A.5)-(A.9) satisfy the wave equation in the applicable layers, whereas Equations (A.10)-(A.14) are the

respective derivatives $\partial E_y/\partial x$, which all have to be continuous across the dielectric layer boundaries.

$$\text{Layer 1. } E_y = A_1 e^{\gamma_1 x} \quad (\text{A.5})$$

$$\text{Layer 2. } E_y = A_2 \cosh \gamma_2 x + B_2 \sinh \gamma_2 x \quad (\text{A.6})$$

$$\text{Layer 3. } E_y = A_3 \cos k_x u + B_3 \sin k_x u, u = x - (W_2 + d) \quad (\text{A.7})$$

$$\text{Layer 4. } E_y = A_4 \cosh \gamma_4 x + B_4 \sinh \gamma_4 x, v = x - (W_2 + 2d + W_4) \quad (\text{A.8})$$

$$\text{Layer 5. } E_y = A_5 e^{-\gamma_5 v} \quad (\text{A.9})$$

$$\text{Layer 1. } \frac{\partial E_y}{\partial x} = \gamma_1 A_1 e^{\gamma_1 x} \quad (\text{A.10})$$

$$\text{Layer 2. } \frac{\partial E_y}{\partial x} = \gamma_2 (A_2 \sinh \gamma_2 x - B_2 \cosh \gamma_2 x) \quad (\text{A.11})$$

$$\text{Layer 3. } \frac{\partial E_y}{\partial x} = -k_x (A_3 \sin k_x u - B_3 \cos k_x u) \quad (\text{A.12})$$

$$\text{Layer 4. } \frac{\partial E_y}{\partial x} = \gamma_4 (A_4 \sinh \gamma_4 v - B_4 \cosh \gamma_4 v) \quad (\text{A.13})$$

$$\text{Layer 5. } \frac{\partial E_y}{\partial x} = (-\gamma_5 A_5) e^{-\gamma_5 v} \quad (\text{A.14})$$

The transverse decay constants $\gamma_1, \gamma_2, \gamma_4, \gamma_5$, the propagation constant k_x , and β the propagation constant in the z -direction, are related as follows:

$$\gamma_1 = (\beta^2 - k_1^2)^{1/2} \quad (\text{A.15})$$

$$\gamma_2 = (\beta^2 - k_2^2)^{1/2} = k_0 (N_{eff}^2 - n_2^2)^{1/2} \quad (\text{A.16})$$

$$\gamma_4 = (\beta^2 - k_4^2)^{1/2} \quad (\text{A.17})$$

$$\gamma_5 = (\beta^2 - k_5^2)^{1/2} \quad (\text{A.18})$$

$$k_x = (k_3^2 - \beta^2)^{1/2} = k_0 (n_3^2 - N_{eff}^2)^{1/2} \quad (\text{A.19})$$

where $k_0 = 2\pi/\lambda$ and $k_i = (2\pi/\lambda)n_i, i=1\dots4$, λ is the operating wavelength, and N_{eff} is the effective index of the waveguide structure. By matching the boundary conditions

for E_y and $\partial E_y/\partial x$, and solving the system of linear equations for the modal propagation constants, the following eigenvalue equation is obtained:

$$\tan 2k_x d = \frac{k_x \left[\gamma_4 \left(\frac{\gamma_5 + \gamma_4 \tanh \gamma_4 W_4}{\gamma_4 + \gamma_5 \tanh \gamma_4 W_4} \right) (\gamma_2 + \gamma_1 \tanh \gamma_2 W_2) + \gamma_2 (\gamma_1 + \gamma_2 \tanh \gamma_2 W_2) \right]}{k_x^2 (\gamma_2 + \gamma_1 \tanh \gamma_2 W_2) - \gamma_2 \gamma_4 \left(\frac{\gamma_5 + \gamma_4 \tanh \gamma_4 W_4}{\gamma_4 + \gamma_5 \tanh \gamma_4 W_4} \right) (\gamma_1 + \gamma_2 \tanh \gamma_2 W_2)}$$

(A.20)

Equation (A.20) relates the physical parameters of the five-layer structure to the mode propagation constants. Solutions to the transcendental eigenvalue equation can be attained only by using numerical methods.

B Normal Modes of Two-Guide Couplers

The analysis of the synchronous coupler structure in Figure 2-8 is similar to the analysis of the simple loaded-strip dielectric waveguide. First, the two dimensional structure is reduced to an one dimensional slab structure by applying the (approximate) EIM. As in the single waveguide problem, TE boundary conditions are invoked when calculating the propagation constants and effective indices of the four-layer slab structures. This is followed by finding the solutions to the wave equation in each of the regions, and applying the TM boundary conditions to solve the five-layer structure in the y -direction.

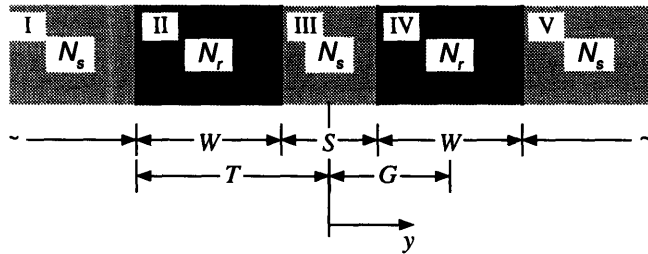


Figure B-1: Synchronous two-guide coupler. The five-layer structure is uniform in the x - z plane. The indices N_s and N_r are obtained using the effective index method.

To establish the coupling coefficients κ_{12} and κ_{21} it is necessary to calculate the propagation constants of the even and odd modes (β_e and β_o) for the structure in Figure B-1. Equations (B.1)-(B.5) are the H_x -fields in the individual layers, whereas equations (B.1)-(B.5) show the E_z -fields in the corresponding dielectric slabs.

$$\text{Layer I } H_x = A_I e^{\gamma(y+T)} \quad (\text{B.1})$$

$$\text{Layer II } H_x = A_{II} \cos [k_y (y + G)] + B_{II} \sin [k_y (y + G)] \quad (\text{B.2})$$

$$\text{Layer III } H_x = A_{III} \cosh [\gamma y] + B_{III} \sinh [\gamma y] \quad (\text{B.3})$$

$$\text{Layer IV } H_x = A_{IV} \cos [k_y (y - G)] + B_{IV} \sin [k_y (y - G)] \quad (\text{B.4})$$

$$\text{Layer V } H_x = A_V e^{-\gamma(y-T)} \quad (\text{B.5})$$

$$\text{Layer I } E_z = \left(\frac{-j}{\omega \epsilon_s} \right) \gamma A_I e^{\gamma(y+T)} \quad (\text{B.6})$$

$$\text{Layer II } E_z = \left(\frac{-j}{\omega \epsilon_r} \right) k_y \{ A_{II} \cos [k_y (y + G)] + B_{II} \sin [k_y (y + G)] \} \quad (\text{B.7})$$

$$\text{Layer III } E_z = \left(\frac{-j}{\omega \epsilon_s} \right) \gamma \{ A_{III} \cosh [\gamma y] + B_{III} \sinh [\gamma y] \} \quad (\text{B.8})$$

$$\text{Layer IV } E_z = \left(\frac{-j}{\omega \epsilon_r} \right) k_y \{ A_{IV} \cos [k_y (y - G)] + B_{IV} \sin [k_y (y - G)] \} \quad (\text{B.9})$$

$$\text{Layer V } E_z = \left(\frac{-j}{\omega \epsilon_r} \right) k_y \{ A_V e^{-\gamma(y-T)} \} \quad (\text{B.10})$$

The quantity γ is the field amplitude decay constant in the side layers, whereas k_y is the propagation constant in the y -direction of the ridge layer, and β is the propagation constant in the z -direction. These quantities are mutually related as follows:

$$\omega^2 \mu_0 \epsilon_s = k_y^2 + \beta^2 \Leftrightarrow k_y = (k_0^2 N_s^2 - \beta^2)^{1/2} \quad (\text{B.11})$$

$$\omega^2 \mu_0 \epsilon_r = \beta^2 - \gamma^2 \Leftrightarrow \gamma = (\beta^2 - k_0^2 N_s^2)^{1/2} \quad (\text{B.12})$$

where $k_0 = 2\pi/\lambda$, λ is the operating wavelength, N_r and N_s are the effective indices of the ridge and side region respectively. By assuring that the values for H_x and E_z are continuous across the boundaries, a system of equation can be obtained, and expressions for the field coefficients and propagation constants can be obtained. Eigenvalue equation (B.13) relates the propagation constants and structure parameters:

$$\frac{(k_y + r\gamma \tan k_y d) (k_y - r\gamma \tan k_y d)}{(k_y^2 + r^2 \gamma^2) \tan k_y d} = \pm e^{-2\gamma a}, r = \frac{\epsilon_r}{\epsilon_s} = \left(\frac{N_r}{N_s} \right)^2 \quad (\text{B.13})$$

To calculate the propagation constant β_e of the symmetric mode, the right hand side is set to be positive. To calculate the propagation constant β_o of the anti-symmetric mode, the right hand side is set to be negative. Solutions to Equation (B.13) can be found only numerically.

For the case of a five-layer slab coupler with TE boundary conditions, the analysis yields the same eigenvalue equation as (B.13) with the only exception that the quantity $r=1$.

C Device Processing Recipes

Table C-1: Etching alignment marks onto the sample.

Processing Step	Parameters
Clean sample	Rinse acetone (ACET), isopropyl (ISO), and methanol (METH) BHF, 5 s Rinse with DI H ₂ O
Deposit SiO ₂ etch mask	PECVD SiO ₂ deposition at 300°C, 2500Å Densify at 420°C for 1 min
Pattern alignment marks	Rinse ACET/ISO/METH Bake (hot plate) at 80°C for 10 min Spin HMDS, 5K rpm, 30 s Spin Shipley 1400-30 photoresist, 5K, 30 s Bake (hot plate) at 80°C for 25 min Expose for 8.5 s at power density 10mJ/cm ² Develop in AZ 351 (5:1 dilution) for 20 s Bake (oven) at 120°C for 25 min
Etch SiO ₂ layer	Reactive ion etch (RIE) in CF ₄ for 20 min (at ~125Å/min)
Remove photoresist	Rinse ACET/ISO
Etch alignment marks	Etch sample in H ₂ SO ₄ :H ₂ O ₂ :H ₂ O (1:8:40) at RT for 20-25 s (~1µm/min), 3000Å Rinse with DI H ₂ O
Remove SiO ₂ layer	BHF, 30 s Rinse with DI H ₂ O

Table C-2: Etching the MSM detector pads.

Processing Step	Parameters
Pattern detector pads	Rinse ACET/ISO/METH Bake (hot plate) at 80°C for 10 min Spin HMDS, 5K rpm, 30 s Spin Shipley 1400-30 photoresist, 5K, 30 s Bake (hot plate) at 80°C for 25 min Expose for 8.5 s at power density 10mJ/cm ² Develop in AZ 351 (5:1 dilution) for 20 s Bake (oven) at 120°C for 25 min
Pre-etch detector pads	Ion beam assisted Cl ₂ etch (IBAE-Cl ₂), 1.1μm
Selective etch to define the detector pads	Etch in PA11 for 20 s Selective etch, H ₂ O ₂ and NH ₄ OH to have a pH=7.5, etches GaAs, stops at Al _{0.60} Ga _{0.40} As Rinse with DI H ₂ O
Remove stop etch layer	HF for 5-10 s Rinse with DI H ₂ O
Remove photoresist	Rinse ACET/ISO

Table C-3: Be ion implantation.

Processing Step	Parameters
Pattern selective implant regions	Rinse ACET/ISO/METH Bake (hot plate) at 80°C for 10 min Spin HMDS, 5K rpm, 30 s Spin Shipley 1650 photoresist, 3K, 30 s Bake (hot plate) at 80°C for 20 min Expose for 0.6 min at power density 10mJ/cm ² Develop in AZ 606 (7:1 dilution) for 12 s Bake (oven) at 80°C for 45 min
Be ion implantation	Room temperature, no tilt ($N_T=3.9\times 10^{14}$ cm ⁻²) 400 keV, 5/13 N_T 220 keV, 5/13 N_T 100 keV, 5/13 N_T
Remove photoresist	Soak and spray clean with acetone RIE with O ₂ only as needed
Clean sample	Dip in H ₂ SO ₄ for 10 s Rinse with DI H ₂ O
Deposit anneal cap	Pyrolytic nitride at 700°C, 900Å PSG at 300°C, 2000Å
Anneal sample	Rapid thermal anneal at 900°C for 10 s
Remove anneal cap	Soak in HF:H ₂ O (50:50) for 2 min Rinse with DI H ₂ O Check with ellipsometer

Table C-4: Waveguide rib etching.

Processing Step	Parameters
Clean sample	Rinse ACET/ISO/METH
Deposit SiO ₂ etch mask	PECVD SiO ₂ deposition at 300°C, 1500Å Densify at 420°C for 1 min
Pattern waveguide ribs	Rinse ACET/ISO/METH Bake (hot plate) at 80°C for 10 min Spin HMDS, 5K rpm, 30 s Spin Shipley 1400-30 photoresist, 5K, 30 s Bake (hot plate) at 80°C for 25 min Expose for 8.5 s at power density 10mJ/cm ² Develop in AZ 351 (5:1 dilution) for 20 s Bake (oven) at 120°C for 25 min
Etch SiO ₂ layer	Reactive ion etch (RIE) in CF ₄ for 18 min (at ~125Å/min)
Etch waveguide rib	Ion beam assisted Cl ₂ etch (IBAE-Cl ₂)
Remove photoresist	Rinse ACET/ISO
Remove SiO ₂ layer	BHF, 30 s Rinse with DI H ₂ O

Table C-5: TIR mirror and groove etching.

Processing Step	Parameters
Clean sample	Rinse ACET/ISO/METH
Deposit SiO ₂ etch mask	PECVD SiO ₂ deposition at 300°C, 3000Å Densify at 420°C for 1 min
Pattern TIR mirrors and etch grooves	Rinse ACET/ISO/METH Bake (hot plate) at 80°C for 10 min Spin HMDS, 5K rpm, 30 s Spin Shipley 1650 photoresist, 3K, 30 s Bake (hot plate) at 80°C for 25 min Expose for 8.5 s at power density 10mJ/cm ² Develop in AZ 606 (7:1 dilution) for 10 s Bake (oven) at 120°C for 25 min
Etch SiO ₂ layer	Reactive ion etch (RIE) in CF ₄ for 35 min (at ~125Å/min)
Etch waveguide rib	Ion beam assisted Cl ₂ etch (IBAE-Cl ₂), at an angle of 30°, depth greater than 7.5µm
Remove photoresist	Rinse ACET/ISO
Remove SiO ₂ layer	BHF, 40 s Rinse with DI H ₂ O
Clean sample	Rinse ACET/ISO/METH
Deposit SiO ₂ to protect the TIR mirrors	PECVD SiO ₂ deposition at 300°C, 1500Å Densify at 420°C for 1 min

Table C-6: Deposit detector pattern, contacts and contact pads.

Processing Step	Parameters
Pattern detector regions and modulator contacts	Rinse ACET/ISO/METH Bake (hot plate) at 80°C for 10 min Spin HMDS, 3K rpm, 30 s Spin Shipley 1400-30 photoresist, 3K, 30 s Bake (hot plate) at 80°C for 25 min Expose for 5.0 s at power density 10mJ/cm ² Develop in AZ 351 (5:1 dilution) for 23 s Bake (oven) at 80°C for 30 min
Etch SiO ₂ layer	Dip in mild soapy water for 5 s BHF, 30 s (~90Å/s) Rinse with DI H ₂ O
Evaporate contacts	300Å Ti : 1000Å Au
Lift-off metal	Soak in acetone, lightly spray with bottle
Pattern contacts and contact pads	Rinse ACET/ISO/METH Bake (hot plate) at 80°C for 10 min Spin HMDS, 5K rpm, 30 s Spin Shipley 1650 photoresist, 3K, 30 s Bake (hot plate) at 80°C for 25 min Expose for 0.6 min at power density 10mJ/cm ² Develop in AZ 606 (7:1 dilution) for 12 s
Sputter metal	300Å Ti : 3500Å Au
Lift-off metal	Soak and spray with acetone

Table C-7: Backside sample processing.

Processing Step	Parameters
Protect top surface of device with polyimid	Measure device thickness Spin-coat the sample with PI 2555 polyimid 5K rpm, 30 s Measure device thickness
Thin sample	Mount sample topside-down on polishing jig with wax Lap the substrate to a thickness of $\approx 120\mu\text{m}$ Polish substrate with Clorox™ to a thickness $\approx 110\mu\text{m}$ Soak in hot trichloroethylene to remove from jig
Remove polyimid	Remove polyimid by soaking in AZ 606 (7:1 dilution) developer for 2.5 min Rinse with DI H ₂ O
Mount onto glass slide	Mount sample topside-down on glass slide with μ -stop
Clean back side	Rinse ACET/ISO Etch in PA11 for 20 s (removes $\sim 50\text{\AA}$) Rinse with DI H ₂ O
Evaporate back contact	300 \AA Ge : 600 \AA Au : 300 \AA Ni : 2000 \AA Au
Microalloy contact	400°C for 30 s
Cleave and mount	Mount sample with conducting silver paint

References

- [1] Lincoln Laboratory Journal, "Special Issue on Adaptive Optics," vol. 5, no. 1, Spring 1992.
- [2] Cheng, Y-Y., and Wyant, J.C., "Phase shifter calibration in phase-shifting interferometry," *Appl. Opt.*, vol. 24, no. 18, 3049-3052, 1985.
- [3] Bareket, N., "Three-channel phase detector for pulsed wavefront sensing," *Proc. SPIE*, vol. 551, 12.35, 1985.
- [4] Wyant, J.C., and Pettyjohns, K.N., "Three-dimensional surface metrology using a computer controlled non-contact instrument," *Proc. SPIE*, vol. 661, 292-295, 1986.
- [5] Kinnstaetter, K., Lohman, A.W., Schwider, J., and Streibl, N., "Accuracy of phase shifting interferometry," *Appl. Opt.*, vol. 27, no. 24, 5082-5089, 1989.
- [6] Hayes, J., and Lange, S., "A heterodyne interferometer for testing laser diodes," *Proc. SPIE*, vol. 429, 22-26, 1983.
- [7] Tarabocchia, M., and Holly, S., "Dynamic Hartman wavefront sensor in applications," *Proc. SPIE*, vol. 343, 93-100, 1982.
- [8] Rousset, G., Primot, J., and Fontanella, J.C., "Turbulent wavefront sensing and image processing," *Proc. SPIE*, vol. 936, 311-318, 1988.
- [9] Fried, D.L., "Post-detection wavefront distortion compensation," *Proc. SPIE*, vol. 828, 127-133, 1987.
- [10] Allen, J.G., Jankevics, A., Wormell, D., and Schmutz, L., "Digital wavefront sensor for astronomical image compensation," *Proc. SPIE*, vol. 739, 124-128, 1987.
- [11] Hardy, J.W., Lefebvre, J.E., and Koilopoulos, C.L., "Real-time atmospheric compensation," *J. Opt. Soc. Am.*, vol. 67, no. 6, 360-369, 1977.
- [12] Rediker, R.H., Lind, T.A., and Burke, B.E., "Optical wavefront measurement and/or modification using integrated optics," *J. Lightwave Technol.*, vol. 6, no. 6, 916-932, 1988.
- [13] Rediker, R.H., Zollars, B.G., Lind, T.A., Hatch, R.E., and Burke, B.E., "Measurement of the wavefront of a pulsed dye laser using an integrated optics wavefront sensor with 200-nsec temporal resolution," *Optics Lett.*, vol. 14, no. 8, 381-383, 1989.
- [14] Bossi, D.E., Goodhue, W.D., Finn, M.C., Rauschenbach, K., Bales, J.W., and Rediker, R.H., "Reduced-confinement antennas for GaAlAs integrated optical waveguides," *Appl. Phys. Lett.*, vol. 56, no. 5, 420-422, 1990.

- [15] Bossi, D.E., Goodhue, W.D., Goodhue, L.M., and Rediker, R.H., "Reduced-confinement GaAlAs tapered waveguide antennas for enhanced far-field beam directionality," *IEEE J. Quantum Electron.*, vol QE-27, no. 3, 687-695, 1991.
- [16] Lau, S., Donnely, J.P., Wang, C.A., Goodman, R.B., and Rediker, R.H., "Optical Phase Difference Measurement and Correction Using AlGaAs Integrated Guided-Wave Components," *IEEE Photon. Technol. Lett.*, vol. 3, no. 10, 902-904, 1991.
- [17] Lau, S., "Optical phase difference measurement and correction using AlGaAs guided-wave components," MIT Ph.D. Thesis, 1992.
- [18] Giallorenzi, T.G., Bucaro, J.A., Dandridge, A., Sigel, G.H. Jr., Cole, J.H., Rashleigh, S.C., and Priest, R.G., "Optical fiber sensor technology," *IEEE J. Quantum Electron.*, vol QE-18, no. 4, 626-665, 1982.
- [19] Sasaki, O., and Takahashi, K., "Sinusoidal phase modulating interferometer using optical fibers for displacement measurement," *Appl. Opt.*, vol. 27, no. 19, 4139-4142, 1988.
- [20] Moore, D.T., Murray, R., Neves, F.B., "Large aperture ac interferometer for optical testing," *Appl. Opt.*, vol. 17, no. 24, 3959-3963, 1978.
- [21] Johnson, G.W., Leiner, D.C., and Moore, D.T., "Phase-locked interferometry," *Optical Eng.*, vol. 18, no. 1, 46-96, 1979.
- [22] Kim, Y.S., Ramaswamy, R.V., and Sakai, S., "GaAs/AlGaAs optical waveguides on silicon substrates grown by molecular beam epitaxy," *Appl. Phys. Lett.*, vol. 53, no. 17, 1586-1587, 1988.
- [23] Tamir, T., *Guided-Wave Optics*, Springer-Verlag, Berlin, 1988.
- [24] Adachi, S., "GaAs, AlAs and $\text{Al}_x\text{Ga}_{1-x}\text{As}$: Material parameters for use in research and device applications," *J. Appl. Phys.*, vol. 58, no. 3, R1-R29, 1985.
- [25] Deri, R.J., Kapon, E., and Schiavone, L.M., "Bend losses in GaAs/AlGaAs optical waveguides," *Electron. Lett.*, vol.23, no. 16, 845-847, 1987.
- [26] Kapon, E., and Bhat, R., "Low-loss single-mode GaAs/AlGaAs optical waveguides grown by organometallic vapor phase epitaxy," *Appl. Phys. Lett.*, vol. 50, no. 23, 1628-1630, 1987.
- [27] Hunsperger, R.G., *Integrated Optics: Theory and Technology*, Springer-Verlag, Berlin, 1991.
- [28] Casey, H.C., Jr., Sell, D.D., and Panish, M.B., "Refractive index of $\text{Al}_x\text{Ga}_{1-x}\text{As}$ between 1.2 and 1.8 eV," *Appl. Phys. Lett.*, vol. 24, no. 2, 63-65, 1974.
- [29] Marcuse, D., *Theory of Dielectric Optical Waveguides*, Academic Press, Boston, 1991.

- [30] Haus, H., *Waves and Fields in Optoelectronics*, Prentice-Hall, Englewood Cliffs, 1984.
- [31] Damask, J.N., "A New Photonic Device: The Integrated Resonant Channel-Dropping Filter," MIT S.M. Thesis, 1993.
- [32] Casey, C., Jr., Sell, D.D., and Wecht, K.W., "Concentration dependence of the absorption coefficient for n- and p-type GaAs between 1.3 and 1.6 eV," *J. Appl. Phys.*, vol. 46, no. 1, 250-257, 1975.
- [33] Kingston, R.H., "Electroabsorption in GaIn AsP," *Appl. Phys. Lett.*, vol. 34, no. 11, 744-746, 1979.
- [34] Yariv, A., *Optical Electronics*, Saunders College Publications, Philadelphia, 1991.
- [35] Kato, K., Hata, S., Kozen, A., Oku, S., Matsumoto, S., and Yoshida, Y., "22 GHz photodiode monolithically integrated with optical waveguide on semi-insulating InP using novel butt-joint structure," *Electron. Lett.*, vol. 28, 1140-1142, 1992.
- [36] Doldissen, W., Fiedler, F., Kaiser, R., and Morl, L., "Butt coupled photodiodes integrated with Y-branched optical waveguides on InP," *Electron. Lett.*, vol. 25, 35-37, 1989.
- [37] Chandrasekhar, S., Campbell, J.C., Dentai, A.G., and Qua, G.J., "Monolithic integrated waveguide photodetector," *Electron. Lett.*, vol. 23, 501-502, 1987.
- [38] Bornholdt, C., Doldissen, W., Fiedler, F., Kaiser, R., and Kowalsky, W., "Waveguide-integrated PIN photodiode on InP," *Electron. Lett.*, vol. 23, 2-4, 1987.
- [39] Erman, M., Jarry, P., Gamonal, R., Gentner, J., Stephan, P., and Guedon, C., "Monolithic integration of a GaIn As p-i-n photodiode and an optical waveguide: modeling and realization using chloride vapor phase epitaxy," *J. Lightwave Technol.*, vol. 6, 399-411, 1988.
- [40] Deri, R.J., Doldissen, W., Hawkins, R.J., Bhat, R., Soole, B.D., Schiavone, L.M., Seto, M., Andreadakis, N., Silberberg, Y., and Koza, M.A., "Efficient vertical coupling of photodiodes to InGaAsP rib waveguides," *Appl. Phys. Lett.*, vol. 58, 2749-2751, 1991.
- [41] Bossi, D.E., Ade, R.W., Basilica, R.P., and Berak, J.M., "Regrowth-Free Waveguide-Integrated Photodetector with Efficient Total-Internal-Reflection Coupling," *IEEE Photon. Technol. Lett.*, vol. 5, no. 2, 166-169, 1991.
- [42] Streetman, B.G., *Solid State Electronic Devices*, Prentice-Hall, Englewood Cliffs, 1980.
- [43] Milnes, A.G., and Feucht, D.L., *Heterojunction and Metal-Semiconductor Junctions*, Academic Press, New York, 1972.

- [44] Wang, C.A., Paitnaik, S., Caunt, J.W., and Brown, R.A., "Growth characteristics of a vertical rotating-disk OMVPE reactor," *J. Cryst. Growth*, vol. 93, 228-234, 1988.
- [45] Donnelly, J.P., "Ion implantation in III-V semiconductors," in *III-V Semiconductor Materials and Devices*, (R.J. Malik ed.), Elsevier Science Publishers B.V., Amsterdam, 1989.
- [46] Donnelly, J.P., "The electrical characteristics of ion implanted compound semiconductors," in *Nuclear Instruments and Methods*, 553-571, 1981.
- [47] Donnelly, J.P., Leonberger, F.J., and Bozler, C.O., "Uniform-carrier-concentration p-type layers in GaAs produced by beryllium ion implantation," *Appl. Phys. Lett.*, vol. 28, no. 12, 706-708, 1976.
- [48] Pauw van der, L.J., "A method of measuring specific resistivity and Hall effect of discs of arbitrary shape," *Philips Research Reports*, vol. 13, 1-9, 1958.
- [49] Petritz, R.L., "Theory of an experiment for measuring the mobility and density of carriers in the space-charge region of a semiconductor surface," *Phys. Rev.*, vol. 110, no.6, 1254-1262, 1958.

